CRANFIELD UNIVERSITY

ARISTEIDIS ANTONAKIS

MULTI-DISCIPLINARY PERFORMANCE STUDIES ON PROPULSION SYSTEM INTEGRATION FOR MILITARY AIRCRAFT

SCHOOL OF AEROSPACE, TRANSPORT AND MANUFACTURING

PhD Thesis
Academic Year: 2018 - 2019

Supervisor: Dr Theoklis Nikolaidis
January 2019

CRANFIELD UNIVERSITY

SCHOOL OF AEROSPACE, TRANSPORT AND MANUFACTURING

PhD Thesis

Academic Year 2018 - 2019

ARISTEIDIS ANTONAKIS

MULTI-DISCIPLINARY PERFORMANCE STUDIES ON PROPULSION SYSTEM INTEGRATION FOR MILITARY AIRCRAFT

Supervisor: Dr Theoklis Nikolaidis
January 2019

ABSTRACT

Military aircraft propulsion systems represent one of the most challenging sectors of jet engine design: Operating at an extremely variable environment strongly influenced by aircraft aerodynamics, these engines should pack high thrust output at the minimum possible size without compromising reliability and operating cost. In addition, the multidisciplinary nature of military aircraft operations frequently introduces contradicting performance objectives which are hard to incorporate to engine design. All the above are combined with the very high cost of engine development, necessitating proper selections early in the design phase to ensure the success of the development process and the viability of new engine concepts.

Despite the significant volume of research in the field and perhaps due to the sensitivity of the data involved, studies published to date are focused on rather specific topics without addressing the full multidisciplinary aircraft-propulsion system integration problem. In order to achieve this, a new synthesis of methods needs to be established combining aspects and contributions from different areas of research.

This project investigates the development of a new methodology for interconnecting engine preliminary design to aircraft operational requirements. Under this scope, a representation of a generic military airframe is constructed and combined with engine performance models and simulation tools to investigate propulsion system effects on aircraft mission performance and survivability. More specifically, the project's contributions in the field of military aircraft propulsion system integration are focused on three domains:

- A new military aircraft representation modelling critical aspects of the interaction between the aircraft and the propulsion system: Aircraft aerodynamics, airframe/propulsion system aerodynamic interference, IR and noise signature. The model has low computational requirements and is suitable for use in the context of large-scale parametric studies and trajectory optimization cases.

- New simulation-based techniques for estimating climb performance and assessing the mission capabilities of aircraft/engine configurations in realistic mission scenarios. Points of novelty within the developed methods include a multi-objective formulation to the climb trajectory problem, a technique for Altitude-Mach tracking, an expansion of the Energy-Manoeuvrability (E-M) technique allowing for the concurrent optimization of the aircraft trajectory and engine schedule and the introduction of minimum noise and IR trajectories for military aircraft.
- The quantification of propulsion system effects on aircraft survivability, taking into account both the aircraft's IR signature and aircraft/missile kinematic performance. This is achieved through a combination of an aircraft IR model with kinematic simulations of missile-vs-aircraft and aircraft-vs-aircraft which are used to measure an aircraft's susceptibility to attacks, along with its own ability to attack manoeuvring targets.

The above methods are developed and validated using published data and applied to investigate aircraft performance trends in a series of test cases where the effectiveness of different propulsion system designs is evaluated in a variety of simulated mission tasks. The results successfully demonstrate the developed methods' ability to quantify the relation between aircraft performance and engine design, providing a basis for understanding the performance trade-offs that result from the adoption of different propulsion system configurations, to maximize the efficiency of the powerplant design process.

Keywords:

Survivability; Trajectory Optimization; IR signature; Climb Performance

ACKNOWLEDGEMENTS

It’s been a long time I had been waiting for this moment and I never imagined that I would have so little time left to write these words. Nevertheless, I will try to make good use of this small space here and pick the opportunity to thank those whose help and support made this project possible:

Professor Pericles Pilidis, for offering me the opportunity to work on this project and for his continuous support throughout the duration of my studies at Cranfield.

My supervisor, Dr Theoklis Nikolaidis for his guidance and constructive feedback that were vital for the quality and timely delivery of this work.

Dr Ioannis Kitsios, Aggelos Fekas for their expert reviews on my research results. Also, my friend, Giorgos Lazarou, for providing me with a helping hand at difficult times.

But most of all, I want to dedicate this work to my wife, Roula, and children, Maya and Aliki. Thank you for your patience, thank you for supporting my efforts and for being my motivation to continue. This must be the end of a long academic journey that we’ve made together, but I cannot promise. One thing is sure: I love you and will always do.

TABLE OF CONTENTS

LIST OF FIGURES

LIST OF TABLES

LIST OF EQUATIONS

LIST OF ABBREVIATIONS

A	Surface Area
A/B	Afterburner
AGARD	Advisory Group for Aerospace Research and Development
ALZ	Aircraft Lethal Zone
ANOPP	Aircraft Noise Prediction Program
AOB	Angle Off Boresight
AUM	All Up Mass
BFM	Basic Fight Manoeuvre
C_D	Drag Coefficient
C_L	Lift Coefficient
C_n	Nozzle Coefficient
C_p	Specific Heat
D	Drag
c_1	PSO Social Factor, Coefficient
c_2	PSO Cognitive Factor, Coefficient
$C_{1,2}$	Radiation Constants
CAD	Computer-Aided Design
CFD	Computational Fluid Dynamics
D	Drag
D_e	Nozzle Diameter
DI	Drag Index
DOF	Degrees Of Freedom
DP	Design Point
E-M	Energy Manoeuvrability
E_s	Specific Energy
ESDU	Engineering Standard Data Unit
FLOPS	Flight Optimization System
FTC	Fuel To Climb
G	Gravitational Acceleration
H	Convection Heat Transfer Coefficient, Altitude
H	Irradiance
H_p	Pressure Altitude

HP	High-Pressure
HPC	High Pressure Compressor
ICR	Inlet Capture Ratio
IMS	Integral Mean Slope
IMST	Integral Mean Slope Truncated
IPAS	Integrated Propulsion/Airframe Analysis System
IR	Infra-Red
IRSL	Infra-Red Signature Level
ISA	International Standard Atmosphere
K	Conduction Heat Transfer Coefficient, Induced Drag Factor
KLZ	Kinematic Lethal Zone
L	Lift, Length
LES	Large Eddy Simulation
LZ	Lethal Zone
LOS	Line Of Sight
LP	Low-Pressure
M	Mass
M	Mach number
MOPSO	Multi-Objective Particle Swarm Optimization
n_z	Aircraft Vertical Load Factor
N	Radiance, Navigation Constant
NEI	Noise Equivalent Irradiance
NGV	Nozzle Guide Vane
NNEP	Navy/NASA Engine Program
NPR	Nozzle Pressure Ratio
NPSS	Numerical Propulsion System Simulation
OASPL	Overall Aircraft Sound Pressure Level
OD	Off-Design
ODP	Off-Design Point
P, p	Pressure, Roll Rate
P_s	Specific Excess Power
PSO	Particle Swarm Optimization
Q, q	Heat, Fuel Consumption

R	Distance
R	Gas Constant, Distance; Radius
RANS	Reynolds-Averaged Navier-Stokes
S	Aircraft Reference Area
SAE	Society of Automotive Engineers
SAM	Surface to Air Missile
SFC	Specific Fuel Consumption
St	Stanton Number
T	Time
T	Temperature, Thrust
TDD	Throttle Dependent Drag
TERA	Techno-economic Environmental Risk Assessment
TET	Turbine Entry Temperature
TR	Temperature Ratio
TTC	Time To Climb
U	Velocity
U	Control Input
UCAV	Unmanned Combat Air Vehicle
USAF	United States Air Force
VR	Velocity Ratio
VSV	Variable Stator Vane
W	PSO Inertial Weight
W	Radiant Emittance
V	Velocity
A	Speed of Sound, Angle of Attack, Acceleration
B	Jet Expansion Angle
Γ	Flight Path Angle
E	Emittance
Θ	Polar Angle
Λ	Wavelength
Ξ	Constant, Aileron Deflection
P	Density
Σ	Stephan-Boltzmann Constant

T	Transmittance, Time Constant
Φ	Polar Angle, Aircraft Bank Angle
Ψ	Aircraft Heading Angle
Ω	Angular Velocity

Subscripts

A	Afterbody
Amb	Ambient
B	Boattail
C	Contrast, Commanded
CL	Climb
CR	Cruise
H	Highlight (Inlet)
J	Jet
LO	Lock On
M	Max, Missile
P	Pressure, Pitch
Ref	Reference
W	Wall
Y	Yaw
∞	Infinity, Ambient

1 INTRODUCTION

The need to improve the performance of military aircraft was the driving force behind the birth of the jet engine. Nowadays, more than eight decades after Sir Frank Whittle's reaction engine prototype and despite the vastly expanded field of gas turbine applications, military aircraft still represent one of the most challenging sectors for jet engine design and operation. Key requirements include high thrust at the minimum possible size combined with the ability to operate at extremely variable environmental conditions; the above should come at a reasonable operating cost and without compromising engine reliability. The contradicting nature of the aforementioned objectives is rather obvious: High performance dictates using state-of-the-art technology, which unavoidably increases development cost and system complexity, the latter leading to increased operating costs and reduced reliability. Careful design is therefore required to produce a competitive powerplant- a successful one should have an operating lifecycle of more than 30 years.

An additional difficulty faced when designing propulsion systems for military aircraft lies in the highly integrated nature of the engine installations. Apart from very few exceptions, engines are installed within the aircraft fuselage which signifies that interference effects between aircraft and engine aerodynamics become pronounced. Because of this and in contrast with civil aircraft applications, engine and aircraft design cannot be handled separately. Proper design selections, synchronization between the airframe and engine design teams and, finally, intense testing is essential if performance deterioration due to interference is to be avoided.

Engine design does also follow the evolution of aircraft designs: Modern air forces require aircraft with multi-role capabilities, in other words, aircraft that are able to fulfil various mission roles and conduct missions in the past requiring different types of aircraft to be accomplished. As a result, a whole military fleet can nowadays consist of a single aircraft type while maintaining the same operational capabilities as before. This helps keep maintenance costs low, reduces crew training requirements and simplifies maintenance and logistics.

With respect to engine design, however, multi-role capabilities are translated as a series of contradicting requirements which need to be satisfied simultaneously. Design optimality consequently becomes a matter of selecting the best compromises between the latter and strongly depends on the 'mix' of mission roles that are to be fulfilled. These may have significant variations among different operators, even for the same aircraft type. To add more, the nature of military operations makes it hard to translate operational requirements into specific engine performance metrics. Contrary to civil transport aircraft, fuel economy is not a primary design driver and it is mostly regarded as a means of increasing payload, range and endurance. In the same context, to fulfil its mission a military aircraft needs to be able to survive in a constantly evolving aerial battlefield environment as, over the years, continuous advances in weapon technology have significantly modified the rules of aerial engagement, prioritizing stealth over pure performance and manoeuvrability.

Given the extremely high development cost of a new engine, all the above issues should be addressed during its preliminary design phase; high cost penalties are to be paid if configuration changes are decided beyond that point. This necessitates the adoption of a new philosophy that will allow for the modelling and management of multiple factors associated with the engine's operational life, incorporating, apart from more traditional performance metrics, concerns about the actual operational performance of airframe/propulsion system configurations in modern battlefields.

Contributions from major research organizations, academic institutions and their industrial partners have paved the way in this wide field of research. Nevertheless, perhaps due to sensitivity of the national-security-critical data involved, not a lot of these research activities find their way to the open literature, in most of the cases comprising only occasional applications or case studies. As a result, the process has still many open items, which should be resolved to provide a basis for understanding the performance trade-offs resulting from the adoption of different propulsion system configurations and maximize the efficiency of the powerplant design process. This would prove

particularly beneficial in terms of development cost, minimizing the need for configuration changes at late design stages.

In this context, the present project focuses on the introduction of a unified multi-disciplinary approach to the modelling and simulation of the integrated performance of military aircraft/engine configurations. Its aim is to form the basis of a new module of Cranfield University's Techno-economic Environmental Risk Assessment (TERA) framework, which will allow for applying its principles to the study of military aircraft powerplants and evaluate the effect of new technologies on the engines' operational lifetime, including, but not limited to, operational performance, operating and maintenance cost, pollutant emissions and component lifing.

The above task was split into three main objectives, as per following:

1. *To quantify the effects of military aircraft propulsion system integration on engine and aircraft performance.* This objective is associated with the modelling of the multiple layers of interaction between the engine and the airframe, so as provide a means of studying their impact on the aircraft's ability to fulfil its mission objectives. As the starting point for the development of an associated TERA module, this study will be focused on the development of models accounting for throttle-dependent aerodynamic forces, Infra-Red (IR) emissions and noise signature of integrated aircraft/engine configurations. An initial investigation of modelling techniques should be conducted under the scope of developing parametrizable models that can be used to identify trends in aircraft performance associated with propulsion system design.
2. *To develop a realistic representation of a military aircraft airframe to be used for performance studies of propulsion system configurations*. This objective is complementary to objective 1 and refers to the development of an aircraft aerodynamic representation that will be combined with the aircraft 'interference' models of the previous objective to form a platform for studies on the integrated performance of aircraft/engine configurations. In principle, this should be equivalent to similar models

currently used for studies on different applications (e.g. civil aircraft) within the TERA framework. As for the model of objective 1, modelling accuracy should be sufficient for identifying trends in aircraft performance associated with propulsion system design.

3. *To complete a methodology for the assessment of aircraft and propulsion system performance with respect to mission-specific criteria*. As previously stated, the nature of military aircraft operations is multi-disciplinary and the definition of performance metrics is not as straightforward as in other applications, as traditional methodologies often fail to keep up with the evolution of aerial warfare. Therefore, as part of this objective, new approaches for assessing aircraft performance with respect to operational objectives should be evaluated to provide a more concise interconnection to the engine design process and complete the design loop. In particular, the developed utilities should be able to quantify the influence of the propulsion system on aircraft mission performance and survivability, to set the basis for the optimization of the propulsion system configuration with respect to these objectives.

The thesis consists of 6 Chapters, each divided into multiple sections and subsections. The present Chapter serves as the introduction to the project, presenting the context of this research work, along with its aims, objectives and overall contribution to knowledge.

The literature review performed in the context of this work is included in Chapter 2. This covers a wide range of topics in the field of aircraft/engine integration. Section 2.1 discusses the general principles of aircraft aerodynamics and methods for aircraft aerodynamic modelling. Section 2.2 describes the physical mechanisms around throttle-dependent afterbody forces and presents a historical analysis of research in the field. Following that, in Section 2.3, methods for aircraft performance assessment are discussed, covering topics on mission performance and survivability; as part of this discussion, aircraft IR signature, combat simulation and trajectory optimization are also analysed.

In Chapter 3, the methodology adopted for fulfilling this project's objectives is presented. Section 3.1 is dedicated to the presentation of the aircraft model. Sections 3.1.1-3.1.3 describe the methods used for the development of its individual components accounting for airframe drag, throttle-dependent forces and engine performance. In a similar manner, in Sections 3.2-3.3, details on the development of the aircraft IR and noise signature models are given. Sections 3.4-3.5 present the structure of the simulation-based climb, mission and combat performance modules and provide details on the methods employed.

Chapter 4 contains example applications of the developed modules, using each method to perform comparisons between different aircraft/engine configurations. A discussion of results is performed, highlighting key findings from the numerical experiments that were conducted.

Chapter 5 summarizes the conclusions that were reached as part of the research in the context of this project. Observations that were made are discussed, along with the applicability and limitations of the methods developed.

Based on the above, in Chapter 6, a number of recommendations for future work on the project are made, aiming towards overall capability improvement and pointing out further contributions that are required to complete a TERA module dedicated to the study of military aircraft propulsion systems.

2 LITERATURE SURVEY

This project aims to investigate the combined performance of airframe/propulsion system configurations with respect to mission-specific criteria. In this context, a literature survey focused on fundamental aspects of military aircraft aerodynamics and propulsion system integration effects on aircraft and engine performance was conducted. A review of the research on aircraft mission performance and survivability was also performed with a view to producing guidelines for the intended performance assessment methodology. A general discussion on the findings of this literature survey is presented this Chapter.

2.1 Military Aircraft Aerodynamics

The achievement of heavier-than-air flight at the beginning of the previous century was a milestone that changed the route of human history. Air transport reduced journey times to an extent that gradually led to the globalization of the human civilization. A safe and efficient means of transport, the aircraft was also found to be particularly effective as a weapon too. Controlling the skies proved to have a dramatic effect on the advent of any military operation and consequently, less than a decade after the first manned powered flight, the aerial warfare was introduced [1].

A century of continuous research on the physics of flight has led to a marked evolution in aircraft designs. Among these, in their struggle for air superiority, combat aircraft have always benefited from state-of the-art technology to gain a performance advantage over their opponents. Their own evolution has been at least impressive: The first fighters were made of wood and fabric, reached maximum altitudes of 10,000 feet and had a top speed of merely 80 miles per hour. These have nowadays evolved to highly sophisticated machines, able to carry and deliver tons of weaponry, reach altitudes of several kilometers and top speeds twice the speed of sound. Despite this, modern fighters still obey to the

same simple aerodynamic principles as their predecessors, the fundamental theory behind which had been already established by 1918 [2].

Aerodynamic theory suggests that any aircraft travelling through air experiences a force exerted by the fluid on its surface. It is standard practice to resolve this force into two components, named Lift and Drag. Lift is defined as the component of force acting in the aircraft's plane of symmetry in a direction perpendicular to the line of flight. Lift supports the aircraft in flight by acting against its weight. Drag is the component of force acting along the line of flight which directly opposes motion. The magnitudes of the two forces depend upon the velocity and shape of the aircraft, along with local air properties. In contrast with Lift, Drag is always present and, as a result, a propulsion system is required to counteract its effects by producing Thrust.

The ratio of Lift to Drag is a fundamental measure of an aircraft's aerodynamic efficiency and since the very beginning of aviation research has focused on defining methods for its prediction. Under this scope, various approaches have been tested over the years, including analytical methods, wind tunnel tests, flight tests and, in the most recent years, Computational Fluid Dynamics (CFD).

Though no universal theory for the estimation of Lift and Drag does exist until today, several related methods have been developed most of which rely on the summation of contributions from different aircraft components or flow mechanisms [3, 4, 5]. An example, reproduced from reference [6], is given in Figure 2.1. Such an approach appears to be particularly effective in preliminary design applications where the aircraft's exact geometry is not known or needs to be determined: semi-empirical formulas, as the ones found in references [2] and [7] may be used to produce off-the-self estimates for Lift, Drag and Pitching Moment of wing-fuselage combinations based on simple geometric parameters.

Nowadays, CFD methods offer an alternative means of predicting a vehicle's aerodynamic performance. In a recent example, Ghoreyshi et al. [8] used CFD to construct a simulation model for the Ranger 2000 fighter trainer aircraft. Although results showed good agreement with flight test data, from a practical scope, the procedure to model a complete aircraft in various flight conditions

using CFD appears to be rather complex and computationally expensive for many applications.

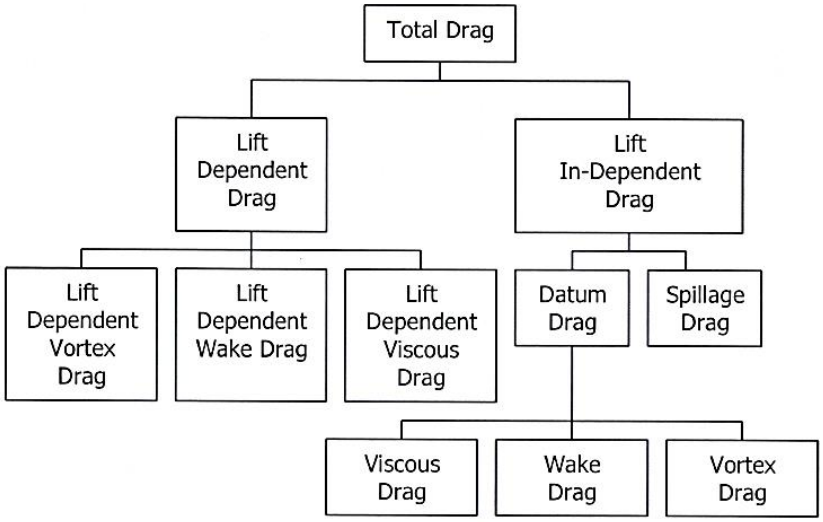

Figure 2.1:[6] An example of a component-based drag prediction strategy.

The most notable effort towards a unified methodology for the component-based prediction of aircraft aerodynamic parameters is perhaps USAF's Stability and Control DATCOM [9], which comprises a collection of methods for estimating aerodynamic stability and control characteristics in preliminary design applications. In a similar direction, in Europe, the ESDU database was formed to provide validated methods for engineering design, including aerospace applications. Cooke [10] demonstrates a methodology of how to produce a detailed aircraft simulation model of the NFLC Jetstream 31 based on ESDU items. In his PhD thesis [6], Laskaridis also relies on ESDU data to create HERMES, a civil transport aircraft model now a part of the TERA framework used for engine performance studies on civil airliners. A preliminary effort to introduce a similar model for a military aircraft was made by Tsentseris [11] who also employed a component-based strategy for aerodynamic force predictions. His study was based upon published data for the F-16 aircraft, considered to represent a typical combat aircraft.

Interestingly, component-based aerodynamic prediction methods are well-suited to military aircraft, as they represent a means to tackle the problem of modelling

the effects of external store installations on the aircraft's aerodynamic performance: The latter became a lot more pronounced after the introduction of the first truly multi-mission jets (such as the F-4 aircraft), which were required to carry payloads that would greatly vary between different missions causing equivalent alterations in aircraft performance due to the combined effects of added mass and drag. In practical terms, this significantly complicated mission planning procedures, as these effects needed to be somehow accounted for, a fact that led to the introduction of the now commonly-used drag index system [12]. The latter assigns a value (the drag index - DI) to each external store which is proportional to the drag increment caused by its installation for some specified flight condition, not including the added mass effects. In its original form, the drag index was specified as the incremental drag area caused by the store at Mach 0.5 multiplied by a factor of ten, as per Equation (5-1).

$$DI = 10\Delta C_{D_{M=0.5}} S \tag{2-1}$$

where $\Delta C_{D_{M=0.5}}$ is the incremental aircraft drag coefficient at M=0.5 and S the aircraft reference area, usually expressed in ft^2. Under the assumption that the drag increments caused by the same store at different flight conditions are correlated to its drag index, generalized drag curves can be constructed and used to predict the aircraft performance at any flight condition. As with every component-based aerodynamic prediction method, the effects of individual store installations are added to create predictions for full mission configurations.

A general limitation of component-based aerodynamic modelling methods [6, 10, 11] is that aerodynamic predictions can be considered valid only for subsonic Mach numbers. The problem that arises from the fact that transonic and supersonic flight is associated with the formation of shock waves that significantly alter the fluid properties of the air surrounding the aircraft [3]. This leads to large variations in the aerodynamic forces exerted to the airframe, their magnitudes becoming strongly affected by the exact shape and relative position of the various aircraft geometric components. In terms of military aircraft

modelling, this imposes a rather restrictive limitation, since their speed envelopes typically extend well into the supersonic regime.

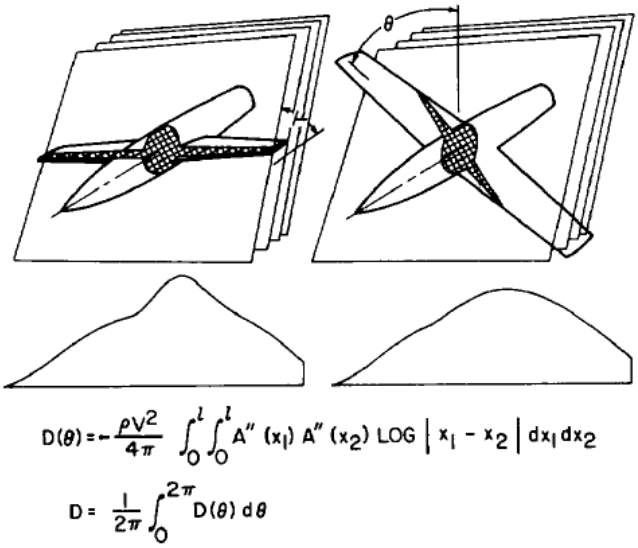

Figure 2.2: [13] Graphical illustration of the Supersonic Area Rule procedure to estimate aircraft wave drag

To tackle this problem CFD modelling can be employed, resolving all the complicated features of the supersonic flowfield around the aircraft [14]. In cases when the use of CFD is not possible, simpler approaches are also available: Perhaps the simplest methodology for the prediction of drag at transonic Mach numbers is Whitcombs' Area Rule [15], first introduced in 1956 and later expanded to the supersonic region by Jones [16]. This approximates the aircraft's three-dimensional geometry with an equivalent body of revolution sharing the same area distribution along planes tangential to the Mach cone. Assuming that the drag of the two bodies is equal, slender body theory is applied to the simplified geometry to obtain an estimate of total drag (Figure 2.2). Experiments proved the validity of the method along with its ability to produce reasonably accurate estimates of drag with minimum computational requirements. In the same context and among other similar efforts, Boeing developed a computer program [13], known as the Harris Wave Drag program, which applies the Area Rule method to aircraft configurations parametrized in a preliminary-design-like manner (Figure 2.3). Though in some occasions the produced geometry approximations may become crude [17], the software

predicts drag accurately enough to support preliminary performance calculations and has been used extensively in aircraft design.

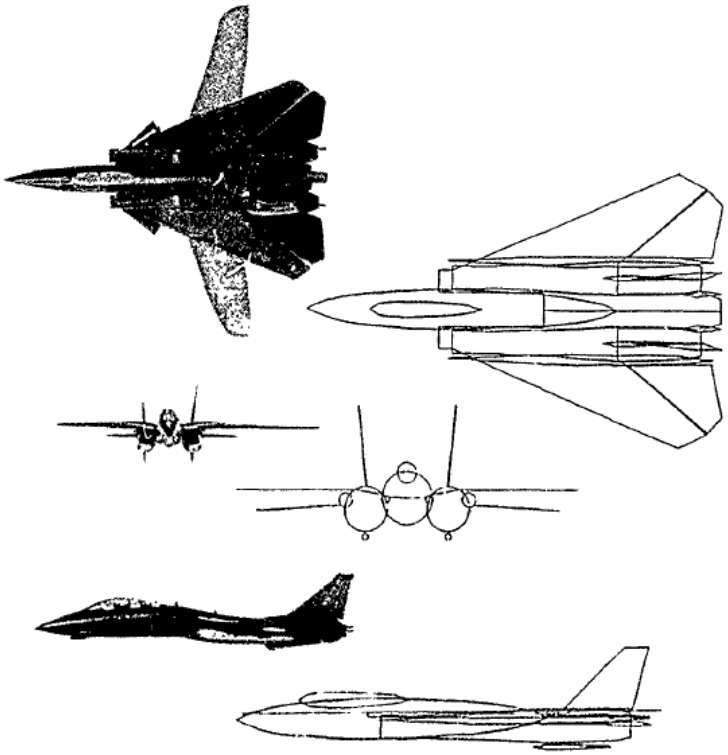

Figure 2.3: [3] F-14 Harris Wave Drag Program model

If a specific aircraft geometry is not required, generic aerodynamic models can be constructed by summing up contributions from various sources that have been published during the last four decades of research in the field. In many cases the aerodynamic data that are available allow for complete representations of different aircraft types to be established: In the context of an extended study on aircraft afterbody aerodynamic design, Glasgow et al. [18] present diagrams showcasing the variation of the zero-lift drag coefficient with Mach number for a variety of aircraft configurations. Heffley and Wayne [19] and Teper [20] provide full aerodynamic representations of the F-4 and F-5 aircraft; an equivalent model for the F-15 aircraft is given in reference [21], also including details on throttle-dependent drag and inlet pressure recovery. Nguyen et al. [22] present data on the subsonic aerodynamics and flight control

system design of the F-16 aircraft, whereas data on the supersonic performance of the same aircraft are included in reference [23].

2.2 Throttle-Dependent Forces

Throttle dependent forces account for all internal and external forces acting on the aircraft as a result of variations in engine power setting. These not only include the forces on the engine stream tube, but also the external forces on the airframe related to the inlet and nozzle flow fields [24]. To achieve maximum performance for a given aircraft/engine combination, the magnitudes of these forces need to be determined at an early design stage so that any undesired installation-related interference phenomena are identified and designed-out. This has been the subject of thorough experimental testing over the previous decades, especially for military aircraft applications where the engine/airframe interactions are stronger as a result of the highly-integrated engine installations and the extended flight envelopes. To provide some standardization for tests it has become common to discretize throttle-dependent forces into inlet and afterbody forces depending on the airframe area these are exerted at.

In the context of his PhD project [25], fellow researcher T. Triantafyllou has conducted research on military aircraft inlet characteristics combining CFD and engine simulations to measure the effect of inlet conditions on the engine's installed thrust and to quantify airflow distortion as a function of flight conditions. Benefiting from his contribution and with a view to producing a model that will include all throttle-dependent aircraft/engine interactions, in this project, research was focused on the quantification of afterbody forces and their effects on engine performance. Under this scope, a literature survey on the aerodynamics of military aircraft afterbodies and their interactions with propulsive jets was made. Its results are presented in the following paragraph.

2.2.1 Afterbody drag

The introduction of the afterbody drag concept arises from the need to book-keep engine and aircraft performance and, in particular, to obtain a full appreciation of what constitutes thrust and drag for a large variety of aircraft/engine configurations. Such knowledge is crucial in order to identify the contribution of each individual component on the whole-aircraft's performance; the causes of performance shortcomings may then be identified and component modifications be carried out to resolve the problem. However, for this approach to be effective and, given that the distinction between thrust and component drag is non-physical (in practice, an aircraft in flight only experiences one force), exact definitions are required for all the associated quantities and their interfaces. This ensures that all contributions are included and not double-accounted [26], allowing for the separate study of engine and airframe performance by the respective manufacturers.

An airframe's afterbody is defined as the rear part of its structure, characterized by a consistent decrease in cross-sectional area when progressing backwards along the aircraft's longitudinal axis. Based on this definition, the afterbody is neither a closed nor an infinite body, consequently, according to potential flow theory [27] there will be a buoyant force exerted on it along the flow direction even under the assumption of ideal, frictionless flow. This force should not be confused with Afterbody Drag.

Afterbody Drag is a force acting along the line of flight and directly opposing the motion of the vehicle which results from the failure of the afterbody force to match the potential buoyancy force. This is defined as the surface integral of the difference between real and potential flow pressure distributions over the afterbody's surface plus a term accounting for the afterbody's skin friction drag:

$$D_a = \oint_a (P_s - P_s^{pot}) dA + f_a \qquad (2\text{-}2)$$

In a typical military aircraft/engine configuration, the jet exhaust is placed at the rear end of the airframe's afterbody, leading to considerable interference

between the jet stream and the local external airflow. As a result of this interaction, afterbody Drag is significantly affected by the properties of the jet flow, becoming essentially a throttle-dependent force. This effect was noted almost as soon as jet engines were applied to aircraft propulsion [28], however, extended research was required before a fair understanding of the underlying flow phenomena was achieved.

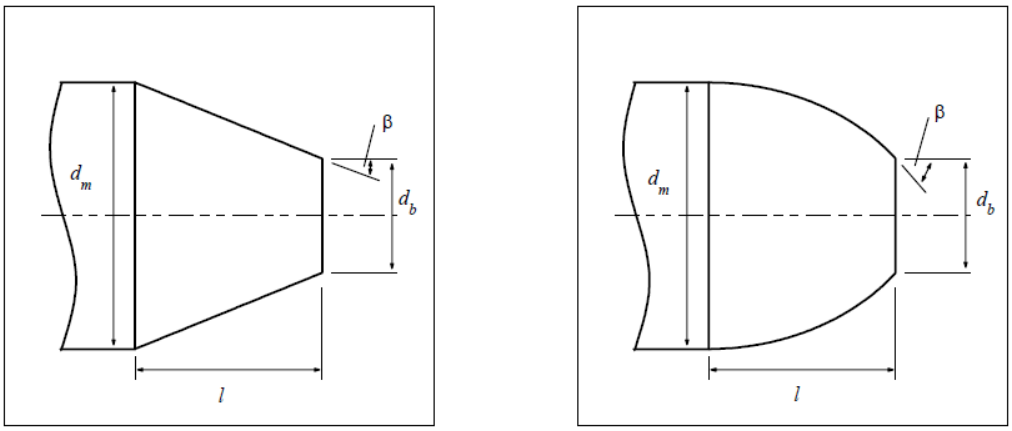

Figure 2.4: Typical afterbody geometries. Reproduced from [29]

Figure 2.5, obtained from reference [28], depicts a typical variation of the afterbody drag coefficient of a conical or circular-arc afterbody (Figure 2.4) with the jet-to-freestream velocity ratio. Three main regions of interference may be identified:

1. The “base bleed” region, spanning from jet-off condition to a velocity ratio of 1. In the absence of a propulsive jet, the rear surface of the afterbody acts as a base area. As a result, jet-off drag is typically high. Its value, however, appears to fall rapidly if quite small quantities of fluid are allowed to flow through the nozzle. Being associated with very low values of jet velocity, this region lies well outside the operating range of propulsion systems.

2. The “entrainment-dominated” region, starting at $\frac{u_j}{u_\infty} = 1$ and ending at the point where Nozzle Pressure Ratio (NPR) reaches a value of 1.89 (jet reaches sonic speed). As the jet velocity increases, freestream air is

entrained into the jet, leading to local flow acceleration. This results in a pressure drop over the afterbody which generates drag.

3. The “plume-dominated” region, for NPR>1.89. As soon as the jet flow reaches sonic conditions, the under-expanded jet forms a plume which displaces the freestream flow and causes pressures on the afterbody to rise. Acting against the entrainment effect, exhaust pluming begins to dominate as NPR increases. For high NPRs, the plume may become large enough for the afterbody drag to become negative.

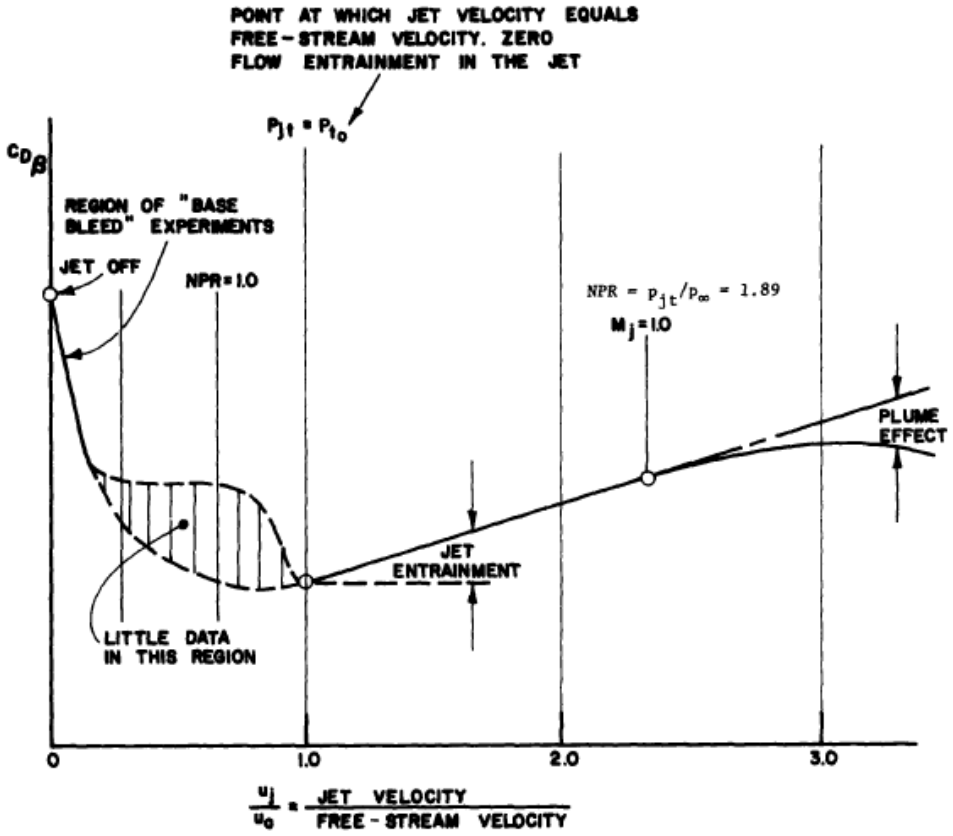

Figure 2.5: [28] Typical variation of the afterbody drag coefficient C_{D_b} of a conical or circular-arc afterbody with the jet-to-freestream velocity ratio

A change towards multi-mission military aircraft designs during the 1970s dictated the need for methods that could predict nozzle/afterbody performance over a wide range of flight conditions and operating NPRs. This was reflected in a significant increase in the number of experiments associated with ducted afterbody designs [18, 30-36].

Studying the relation between exhaust gas physical properties and afterbody drag, Compton [32] identified a connection between plume blockage effects and the plume's initial expansion angle δj, the latter being equal to the Prandtl-Meyer expansion angle of the jet flow when expanded to the external boattail static pressure. Attempting to establish a similar relation for entrainment effects, Compton evaluated various parameters and concluded that these varied in an almost linear fashion with the ratio $\frac{R_j T_j}{R_\infty T_\infty}$, R and T corresponding to the gas constant and static temperature respectively. In most of these experiments, afterbody drag was dominated by plume blockage, whereas entrainment effects became significant in cases where large regions of separated flow were present.

During the same era, Swavely and Soileau [30] collected data from parametric wind tunnel tests and proposed a factor relating afterbody pressure drag to the body's cross-sectional area distribution. Obviously inspired by Whitcomb's Area Rule [15], this shape factor was named the Integral Mean Slope (IMS). IMS drag predictions showed good agreement with experimental data over a variety of afterbody configurations, later further improved by Brazier and Ball [31] with the introduction of the Integral Mean Slope Truncated (IMST) concept which incorporated the effects of flow separation to the basic IMS formula.

Based around the same principles and in the absence of sophisticated CFD tools, a series of methods for the prediction of nozzle/afterbody performance were developed during the early 1970s [18] and were applied to preliminary design and mission analysis studies of multi-role combat jets. Though particularly suited to these applications, these methods provided no insight to the actual shape of the flowfield around the afterbody and were consequently unable to address problems emerging from geometry-dependent local flow distortion. In fact, such issues were commonplace during the development of most combat aircraft of that era: notable examples include the Tornado [37, 38, 39], the FIAT G.91Y [37, 40] and the Douglas A-4 aircraft [39]. In all these cases, flow instability over the afterbody was the cause for increased drag combined with severe buffet and loss of directional control. Structural failures of

nozzle flaps have also been observed in the B-1 and F-15 aircraft as a result of the strong coupling between twin-jet plumes [41]. Prediction of these undesired phenomena at the earliest possible design stage became thus a requirement in order to reduce development costs.

Advances in computer technology allowed for effective CFD tools to be gradually introduced to afterbody design applications to serve this scope. Probably some of the best indicators of this progress are AGARD's AR-226 [37] and AR-318 [42] reports, published June 1986 and September 1995 respectively, in which state-of-the-art CFD methods of each era are assessed against wind tunnel data over a variety of test conditions and afterbody configurations. A comparison of the two reports clearly pinpoints the evolution in both CFD methodology and its applications. The growth in computational power allowed for complex three-dimensional geometries to be examined in the most recent report, as compared to the axisymmetric two-dimensional cases of its predecessor. One may also observe that between 1986 and 1995 the use of Reynolds-Averaged Navier-Stokes (RANS) solvers became far more extended, gradually leading to the abandonment of older methods such as the Viscous-Inviscid Interaction schemes. A rather unexpected finding, however, is that according to the results published in AR-318 [42], as of 1995, CFD predictions of afterbody drag still failed to match the accuracy of well-tuned semi-empirical methods based on principles derived during the 1970s.

Nevertheless, over the years, the evolution in CFD has been continuous and it is now an established design tool, with a field of applications that includes a lot more than simple drag predictions. Recently, requirements for noise suppression and infra-red signature reduction have established a whole new research field for CFD. In 2006, Georgiadis and DeBonis [43], reviewing state-of-the-art Navier-Stokes analysis methods for turbulent jets stated that, in terms of these applications, the limits of RANS solvers had been reached; Large Eddy Simulations (LES) were suggested as the next major step towards more accurate predictions. Research on LES methods constitutes a primary topic of research in the CFD field during the current decade [44].

Despite these significant advances in CFD, it appears that there is still a need for semi-empirical methods in preliminary design, since they provide a fast and accurate means for the conceptual evaluation of possible configurations [42]. According to the same reference, because of the complexity associated with grid generation and case setup, CFD analysis and design methods are best suited to the final stage design phase during which they can be used to pre-evaluate the performance of a design and visualize complex flow phenomena so as to reduce the need for wind-tunnel tests [14, 45].

2.3 Aircraft Performance Assessment

The history of aerial warfare has shown that the performance specifications under which a combat aircraft is developed are equally as important for its operational success as the quality of the design itself. The dynamic nature of military operations, however, driven by a constant evolution in armory, makes it difficult to quantify the factors that define air superiority and translate them into measurable design requirements. Failure to formulate design specifications that are representative of real-world combat scenarios has in many occasions ruined the performance potential of otherwise excellent aircraft designs.

Probably the most famous related example is the P-51 Mustang aircraft, which, based on a specification for a low-to-medium altitude interceptor, was initially fitted with a non-supercharged engine that limited its performance at high altitude. Some years later, the growing needs for high-altitude fighters for bomber escort missions led to the replacement of the original powerplant with one suitable for this type of operations (the Rolls-Royce Merlin). This modification completely transformed the aircraft's performance and established it as one of the most successful designs of its era [1].

During the 1950's, military planners predicted that aerial combat would gradually move towards supersonic speeds, using missiles as their prime armament. Under this scope, the F-4 fighter was designed for maximum speed and without provision for an internal gun. During the Vietnam conflict that

followed, the latter proved to be a serious drawback that limited the fighter's combat performance, leading to a cannon being retrofitted to the airframe [46]. Apart from that, air combat never became truly supersonic: even by today's standards, most combat action occurs in the high-subsonic region of the flight envelope where the fighters' turn performance is maximized [39].

Ever since then, performance specifications have evolved considerably based on the feedback gathered from over a century of aerial warfare. Constituting the link between aircraft constructors and military operators, these specifications should guarantee that an aircraft will be effective in the mission it was designed for. Under this scope, a large number of performance measures, including mission types, have been standardized to provide some systemization for aircraft development [47, 48] A fundamental contribution towards this direction was made by USAF pilot J. R. Boyd with the introduction of the Energy-Manoeuvrability (E-M) Theory [49] in the mid-1960s. Boyd and his collaborators suggested that requirements expressed in terms of up-to-then 'traditional' variables such as altitude, airspeed, acceleration and range provided no indication of an aircraft's integrated performance and design efficiency throughout its flight envelope. Instead, based on some earlier work by Rutowski [50], they introduced a theory relating an aircraft's manoeuvrability to its energy state and energy rate capabilities and applied it to conduct performance comparisons between dissimilar aircraft designs. This methodology has been successfully applied to the design of the F-15 [51] and subsequent fighter jets and now represents the most established approach for assessing the performance of military aircraft. In a recent paper, Takahashi [52] illustrates the effectiveness and simplicity of the method, using E-M 'sky maps' to conduct trade studies of notional aerodynamic performance by changing fundamental configuration design variables.

Although the E-M analysis has contributed significantly in quantifying fundamental parameters of an aircraft's performance, deciding on which of the latter are important for a given combat mission remains a matter of qualitative assumptions. For example, instantaneous turn capability is considered vital to

evade from a threatening situation, but of trivial importance for long-range high-speed interception where longitudinal acceleration and speed appear to be the prime requirements. As it has been historically proven, however, such simplifications do not always correspond to the actual requirements of real-world combat scenarios which are variable, complicated and environmentally-affected. Furthermore, in the absence of a means to weigh the contribution of each parameter, deciding over particular design features can be hard if these act in a contradicting manner: e.g. high-speed performance needs to be sacrificed to achieve better turn capability [53].

To make matters worse, following the recent improvements in weapon technology, skepticism has been raised about whether E-M is still suitable for describing combat performance in a modern warfare environment: During the last decades, military aircraft design has demonstrated a consistent departure from this philosophy, prioritizing stealth and sophisticated weaponry instead. This trend has become more obvious than ever after the introduction of the F-35 fighter aircraft, whose design, for the first time, trades manoeuvrability for radar invisibility and has consequently become the subject of much controversy [54].

A recent study [55], emphasizes on the gradual departure from traditional ‘tail-chasing’ fight that has begun after the introduction of effective, long-range, all-aspect IR weapons in the 1980’s: Future combat is expected to involve very little or no manoeuvring at all and will mostly rely on sensor networks, data fusion and smart, long-range weapons. In this context, it is reasonable to question the relation between aircraft manoeuvrability and combat effectiveness: if this connection no longer exists, it would be reasonable to dispense with fuel-thirsty power plants and switch to more efficient solutions that will boost mission range and reduce detectability. On the other hand, one must be cautious not to repeat mistakes of the past: as previously stated, back in the 1950’s, tacticians anticipated that future combat would solely rely on missiles and take place at supersonic speeds, a change that has yet to occur more than half a century later [46]. However, in any case it is well understood that, with the advent of new weapon technologies, new methods are also

required to gain an insight on the requirements of the evolving aerial battlefield. Such predictions will be necessary to ensure the viability of future aircraft and engine projects given the constantly rising investments in both money and time that are required to complete their development [56].

2.3.1 Mission Performance and Simulation

In an effort to provide a solution to the multi-objective problem of aircraft and propulsion system design, manned and unmanned simulation tools have been developed as early as the 1970s and gradually inserted to the design procedure of aircraft and weapon systems [53, 57]. Simulations are particularly suited to modelling the complicated events that occur on the course of an aircraft mission: modelling can include accurate representations of aircraft dynamics, variable environments [53] and/or the pilot himself [58], depending on the type of simulation used. By executing multiple simulation runs of a combat scenario under variable initial conditions, aircraft performance can be statistically isolated and quantitative conclusions may be reached upon the effect of various design parameters on an airframe's combat effectiveness [59]. Of course, these benefits come at a cost since they require considerable computational resources and, in the case of manned simulations, expensive facilities in order to produce a realistic environment for the human pilot. In most cases, however, this is outweighed by the resulting savings in development cost, particularly during the last decades when computational power has become significantly cheaper than it has ever been in the past.

Engine-airframe integration requires careful evaluation of an aircraft's performance in executing the mission it has been design for. Research in this domain must overcome two fundamental difficulties: (a) a suitable means for accurately representing the integrated aircraft/engine performance is required and (b) the nature of the missions flown is such that it becomes hard to discretize them into a finite set of mission profiles. The challenges of aircraft-engine integration are widely reflected into the great volume of related research work, spanning along more than six decades [60, 61].

To provide a common reference for aircraft developers, the US department of Defence issued specifications [48] introducing standardized mission profiles to be used for assessing the performance of military aircraft. These were accompanied by a wide range of performance metrics, intended to unify the entire aircraft performance assessment procedure, to the maximum possible extent. A large number of studies have made use of the data in these specifications; some indicative examples may be found in references [18, 64].

In the field of aircraft and propulsion system modelling and design optimization, NASA has made very significant contributions with the introduction of the Flight Optimization System (FLOPS) [65], the Navy/NASA Engine Program (NNEP) [66], later evolving into the Integrated Propulsion/Airframe Analysis System (IPAS) [67] and, more recently, the Numerical Propulsion System Simulation (NPSS) [68] framework. Large aircraft and engine manufacturers have also demonstrated equivalent capabilities in the same context [64, 69].

In Europe, research institutions and aircraft companies have joined forces to develop aircraft/engine simulation platforms to aid at preliminary design studies [70, 71]. Among the most important efforts in this domain is Cranfield University's Techno-economic and Environmental Risk Assessment (TERA) tool [72], developed to provide an insight on the expected environmental impact and operating cost of conceptual gas turbines. TERA's HERMES [6] module is used as an aircraft performance platform simulating the engine's installed performance on generic airliner airframes and is combined with the University's in-house engine performance code, TURBOMATCH [73] which performs the engine modelling.

2.3.2 Aircraft Trajectory Optimization

Aircraft flight path optimization belongs to a family of trajectory optimization problems that were born out of the need to maximize the performance of air vehicles and/or reduce their operating cost and environmental impact. The pioneering work of Rutowski [50], may be considered as the starting point for

work in this domain, later evolving to the Energy–Manoeuvrability Theory [49] which has contributed significantly to the quantification of aircraft performance. Though computationally inexpensive and relatively accurate, some of the limitations of this methodology were already evident by the late 1960s: The flyability of the optimal paths generated was not guaranteed, while simplifications associated with the method's fundamental assumptions led, in many cases, to unavoidable deviations between actual and estimated results [74, 75]. The gradual increase in the available computational resources and improvement of numerical algorithms led to the introduction of more sophisticated methods for aircraft trajectory optimization: optimal control theory and nonlinear programming techniques have been used extensively under this scope [76-80]. Optimal control theory, when applied to a trajectory optimization problem, seeks an optimal control law; in other words, a sequence of control inputs that drives a given vehicle into a trajectory that minimizes a pre-defined cost function. Methods for solving optimal control problems include Dynamic Programming [79], which is restricted to small state dimensions; Indirect Methods, which use the necessary conditions of optimality to derive and numerically solve a boundary value problem; and Direct Methods, which discretize the original infinite-dimensional control problem to a finite-dimensional one and solve it using nonlinear programming techniques [80].

Genetic algorithms and, in general, population-based optimization schemes represent a more recent addition to the collection of methods for trajectory optimization [81-88]. Although the latter may not be considered computationally competitive with "traditional" optimal control methodology, they incorporate some fundamental advantages that have attracted scientific interest: The convergence of population-based methods is not affected by the smoothness or continuity of the functions being minimized; this feature is particularly suited to aerospace applications where, traditionally, tabular data are used for model construction. This allows for a direct interface between the optimization code and the engine performance software to obtain estimates for thrust and fuel consumption, instead of resorting to simplified, smoothened functional representations for the latter; in fact, when considering the detailed modelling of

an aircraft powerplant, small discontinuities in these quantities and/or their derivatives are typical as a result of bleed valve, NGV, nozzle, bleed and power extraction schedules. Furthermore, because of their very good global search capabilities and contrary to gradient-based optimization methods, population-based schemes do not require an initial guess by the user and can thus been applied to problems with solutions that are hard to estimate [83]. Combining the above with a simple and straightforward implementation leads to a significant reduction in the effort required for case setup and makes trajectory optimization accessible to users without the otherwise-necessary mathematical background or system knowledge. As a result, given the ever-increasing computational power that is available, the use of such schemes has become widespread over the last decades, replacing, in many cases, methods that are more traditional.

Yokoyama and Suzuki [83] developed a modified real-coded genetic algorithm for constrained trajectory optimization to be used for providing appropriate initial solutions to gradient-based direct trajectory optimization methods. The proposed algorithm was applied to a space vehicle's re-entry trajectory problem and produced solutions that were close to the actual optimal solution. Pontani and Conway [84] applied the Particle Swarm Optimization (PSO) technique (an optimization method inspired by the social behaviour of animals) to a series of space trajectory optimization cases and showed that the method is efficient, reliable and accurate in determining optimal trajectories for problems with a limited number of unknown parameters. Rahimi, Kumar and Alighanbari [85] reached the same conclusions while examining the application of PSO to spacecraft re-entry trajectory optimization. Pontani, Ghosh and Conway [86] employed PSO to generate optimal multiple-burn rendezvous trajectories and used the solutions to initialize a gradient-based optimization process; good agreement between the results of the two methods was observed, demonstrating the effectiveness of the PSO scheme. Common features of all the approaches presented above are the use of a direct-shooting-equivalent problem formulation, employing parameterized curves to produce control time histories with a finite number of input variables and the implementation of

constraints by means of penalty functions, selections that are dictated by the characteristics of the selected optimization schemes.

A rather interesting feature of population-based optimization algorithms that has recently been exploited in the field of trajectory optimization is their ability to handle multiple objectives in a single optimization run [62, 87, 88]; in a so-called multi-objective optimization case, instead of a single solution, the optimizer seeks for a set of solutions that correspond to the optimal compromises between contradicting targets; the latter form a front in the objective space, named the Pareto front. This capability partly compensates for the higher computational cost of population-based methods, since multiple runs of a comparable gradient-based optimization method are required to produce the same amount of solutions.

2.3.3 Survivability

A military aircraft's ability to complete its mission is synonymous to its ability to survive the challenges of the modern aerial battlefield. In the past, aerial superiority was purely a matter of flight performance, however, over the last 30 years advances in weapon technology have significantly altered the rules of aerial engagement. Today, highly sensitive sensors can be used to locate aircraft targets from large distances and direct long-range, highly manoeuvrable weapons against them. Consequently, aerial engagements take place at increasing distances and more emphasis is being put on the capabilities of an aircraft's onboard sensors and weapons than on the manoeuvrability of the aircraft itself. In this new environment, it has also become apparent that the careful management of aircraft sensor footprint is a necessity in order to improve the survivability and combat effectiveness of military aircraft [89].

Aircraft detection is achieved by exploiting electromagnetic radiation that is either generated by a transmitter and reflected by the target (active mode) or directly emitted by it (passive mode) [90]. Passive detection is directly related to the aircraft propulsion system's operation: The aerodynamic interference

between an aircraft's external surface and the atmosphere, combined with the massive heat output of the engine, generate high-temperature regions over and around the airframe, which act as sources of radiation in the infrared (IR) spectrum. Ever since the early 1950's, dedicated devices, called IR seekers, have been developed to exploit this property for locating and destroying aircraft targets by directing missiles against them. IR seekers allow for passive detection and tracking of aircraft, which, contrary to active detection methods such as radar, gives no warning to the target [89]. The improvements in seeker technology that have been introduced during the last three decades have dramatically increased the effectiveness of IR-guided weapons and have modified air-to-air combat rules and tactics [55].

The extensive use of IR weapons against aircraft targets has been the motivation for the development of models to estimate aircraft IR signature such as SPIRITS, SIRUS and NATO's NIRATAM codes. Several studies have also been published in the field, attempting to quantify the effect of IR signature on aircraft survivability: Mahulikar et al. [91] proposed a component-based method for IR signature prediction of complete airframes and used it to impose constraints on the aircrafts' flight envelope to avoid exposure to ground-to-air IR threats. Jianwei and Qiang [92] used a coupling between a CFD solver estimating aircraft skin temperature and a reverse Monte-Carlo model for radiation transfer to produce a detailed representation of the IR Signature Level (IRSL) of a fighter jet and assess the individual contribution of various aircraft components to it. Kim et al. [93] employed a similar approach for IRSL estimation and combined it with a simple missile kinematic model to assess aircraft susceptibility to IR-guided air-to-air missiles. Apart from high-fidelity solutions, simplified representations of aircraft IRSL are of some practical value and have also been used in several studies related to aircraft survivability: The work of Rao and Mahulikar [94], expanded in [95, 96], is based upon an isotropic aircraft IR radiation model, which, similarly to reference [93], is combined with a simple missile model to estimate missile lethal range as a function of aircraft and missile flight parameters. In the same context, Andersson [97] studies the effect of skin emissivity on the effectiveness of

attack aircraft against IR-guided SAM sites by means of a very simplified representation of aircraft geometry.

2.3.4 IR Radiation principles

According to Planck's law of radiation, a body's radiant emittance W is given by the formula:

$$W(\lambda) = \frac{\varepsilon(\lambda)C_1}{\lambda^5(\exp(\frac{C_2}{\lambda T})-1)} \quad (2\text{-}3)$$

where C_1, C_2 are the first and second radiation constants, ε is the body's emittance, T is the body temperature and λ is the radiation's wavelength.

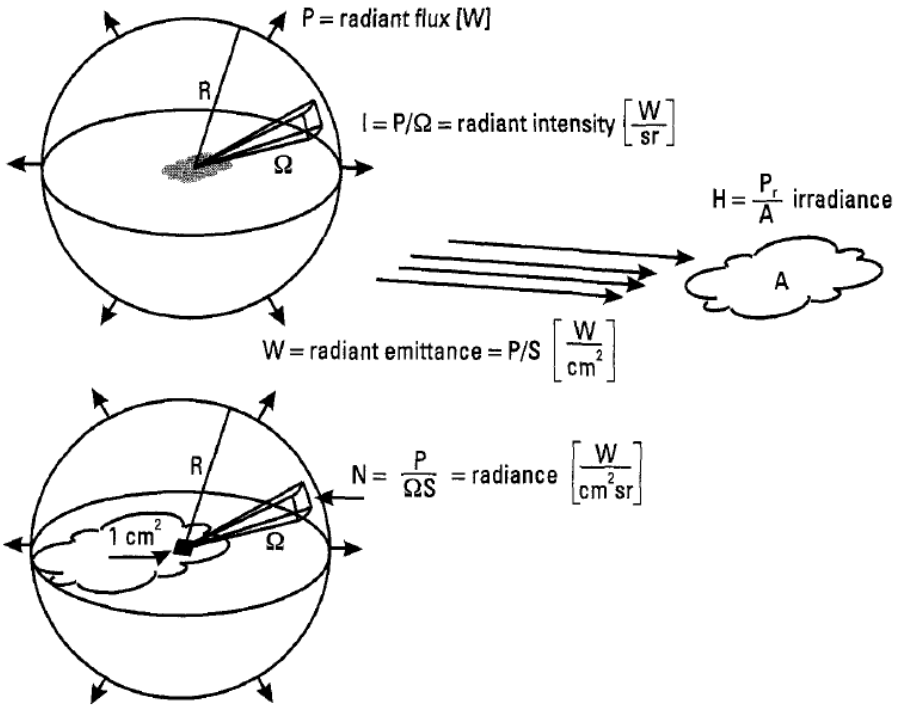

Figure 2.6: Definitions of radiation metrics [90]

Using Eq. (2-3), the body's radiance N in the band (λ_1, λ_2) can be calculated by means of the following integral:

$$N = \frac{1}{\pi}\int_{\lambda_1}^{\lambda_2} W(\lambda)d\lambda \quad (2\text{-}4)$$

The irradiance H at some arbitrary point x_0 located at distance R from the body equals:

$$H = \frac{A}{\pi R^2}\int_{\lambda_1}^{\lambda_2} W(\lambda)\tau(\lambda)d\lambda \quad (2\text{-}5)$$

where A is the body's projected area when viewed from x_0 and τ accounts for atmospheric transmittance, which is the ratio of the radiation flux at distance R to the radiation flux at the source.

The value of transmittance τ is a function of the atmospheric composition along the path between the source and the observation point, and accounts for the strong influence of the atmosphere on the transmission of IR signals. Figure 2.7 presents a typical variation of the atmospheric transmittance with wavelength indicating that only radiation corresponding to special bands, called 'atmospheric windows' can effectively pass through the atmosphere: these bands are exploited by IR sensors for target identification and tracking.

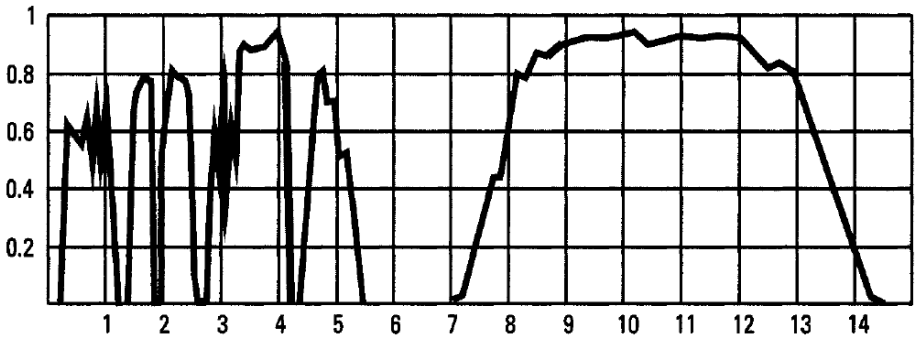

Figure 2.7: Atmospheric transmittance VS wavelength for horizontal path of 1 km length at an altitude of 1 km [90].

A source of IR radiation may be distinguished from its background by means of the difference in irradiance it generates with respect to radiation originating from the background. This property is called contrast irradiance H_c and is defined as follows:

$$H_c = \left(N - N_{bgd}\right)\tau \frac{A}{R^2} \quad (2\text{-}6)$$

where N_{bgd} is the background radiance.

An IR detector is able to locate a radiator if the contrast irradiance at the sensor is larger than a threshold that depends upon a sensor characteristic called Noise Equivalent Irradiance (NEI) which is a measure of the internal noise generated by the sensor, excluding external sources. Assuming that the emitted radiation has wavelengths that lie within the sensor's wavelength band, then detection is possible if:

$$H_c > \xi_{min} NEI \quad (2\text{-}7)$$

Where ξ_{min} is a constant, $\xi_{min} > 1$

The maximum lock-on range (R_{LO}) may be calculated by combining Eqs (2-5) and (2-7):

$$R_{LO} = \sqrt{\left(N - N_{bgd}\right)\tau \frac{A}{\xi_{min} NEI}} \quad (2\text{-}8)$$

Generalizing, for a radiator consisting of a surface with arbitrary temperature distribution:

$$R_{LO} = \sqrt{\frac{\tau}{\xi_{min} NEI} \iint_S \left(N - N_{bgd}\right)(\bar{x} \cdot \bar{n}) dS} \quad (2\text{-}9)$$

$\bar{x}$ and $\bar{n}$ represent the Line-Of-Sight (LOS) and surface normal vectors respectively. This equation needs to be solved iteratively, since the atmospheric transmittance τ is itself a function of the distance R_{LO}.

2.3.5 Air Combat Simulation

Predicting aircraft IRSL is only part of the process for assessing aircraft survivability against IR threats as it only considers the ability of the weapons'

sensors to lock-on to the target and track its movement; in practice, to destroy a manoeuvring target, the weapons must also have the kinematic ability to reach at a sufficient distance close to it so that the detonation of the warhead becomes effective. In addition to this, in an air-to-air combat scenario, the attacker needs to have sufficient manoeuvrability to place himself in a position that his weapons have a high probability of hitting the target [98, 99]. As a result, a complete simulation of such a scenario is a highly complicated task and a lot of research has been conducted on the development of tools to be used for the evaluation of suitable aerial tactics: this is signified by a plethora of proposed methodologies that attempt to provide solutions to aircraft-vs-aircraft and aircraft-vs-missile combat manoeuvring problems. Generally, these are classified into those which formulate an optimization problem and use a suitable solver to solve it [100-105] and rule-based methods [106-109], the former emphasizing on the optimality of the generated solutions and the latter targeting towards reduced computational complexity and real-time applications.

In the US, a variety of platforms that employ artificial Intelligence to generate realistic air combat representations have been developed, finding application in pilot training and in the evaluation of new tactics. These include, among others, the AML [109], TAC Brawler, AASPEM and TDG programs. Using the AML framework, Kosciusko [59] studied the correlation between a fighter aircraft's performance and its combat effectiveness by measuring the outcome of one-vs-one air combat scenarios while varying the aircraft's maximum G capability and thrust-to-weight ratio. His study was limited by the AML program's inability to accommodate the significant variations in the aircraft performance parameters that were introduced. Working on the development of a realistic pursuit-evasion game between a missile and an aircraft, Imado [108], introduced a simplified approach to the problem using proportional and augmented proportional navigation guidance for both vehicles. Despite the method's simplicity, the presented results were in wide agreement with standard pilot techniques for missile evasion [110]. In the same field, You and Shim [106] developed an aerial combat guidance law based on the generation of a virtual pursuit point, used to alter between lag, pure and lead pursuit guidance depending on the

flight condition and the opponent's relative position. The method was validated using simulated air combat scenarios against man-controlled opponents and was shown to be able to reproduce some textbook Basic Fight Manoeuvres (BFMs).

In the field of optimal control theory, air combat is defined as a differential game, usually simplified into a zero-sum pursuit-evasion game [111]. Although the nature of the air combat game makes it a hard-to-solve problem, several studies have proposed methodologies for finding the optimal solutions [102-103, 112-114]. Among the most notable efforts in this domain is the work of Sprinkle et al [105] and Eklund et al [104], who encoded air-combat logic into a non-linear model predictive tracking controller and used it for the real-time control of an autonomous aerial platform which flew successfully against an F-15 flown by a human pilot. In the same context, McGrew et al. [114] employed approximate dynamic programming to develop an air combat guidance law for UCAVs and validated it in sub-scale flight tests. However, due to restrictions of the used vehicles' dynamics, only manoeuvring in the horizontal plane was demonstrated. Despite the sophisticated nature and complexity of these methods, however, most of them have not yet reproduced standardized air-combat tactics [98, 99].

2.4 Research Gap

The previous Sections of this Chapter summarized the findings of the literature survey that was conducted, which investigated past and present research on the broad area of aircraft/propulsion system integration and its effects on the mission performance of military aircraft. Comparing the latter to this project's objectives, specified in Chapter 1, results in the identification of the associated research gap that needs to be filled by this project,

As a general conclusion, it may be stated that despite the significant volume of research in the field, existing studies are focused on rather specific topics instead of addressing the full multi-disciplinary aircraft-propulsion system

integration problem. In order to achieve this, a new synthesis of methods needs to be established combining aspects and contributions from different fields of research.

As far as the aircraft's aerodynamic modelling is concerned, a plethora of research data and/or modelling techniques are readily available for the development of a generic representation of military aircraft aerodynamics. Existing aircraft aero models, however, either do not take into account the aerodynamic interference resulting from the interaction of the airframe with the propulsion system or are limited to a small number of configurations and operating conditions. On the other hand, the data from studies on throttle-dependent forces rarely extend to demonstrate the effects on full aircraft configurations and translate the calculated drag increments to changes in aircraft mission performance. In this context, a more complex model is required, that will allow for modelling of both effects in a parametric manner, so that the aerodynamic influence of the propulsion system is fully accounted for.

As denoted by the large number of performance metrics that have been developed over the years, military aircraft performance is complicated to measure and specify during the design phase. The industrial standard practice is the use of variable fidelity tools to simulate aircraft mission scenarios, however, most of these utilities remain proprietary and are not accessible to the public. In the open literature, there exists instead a wide variety of well-documented trajectory optimization techniques that have not been expanded to full mission applications. It would therefore be a logical step to introduce a new module covering full mission scenarios by further developing or combining these methods.

In air combat scenarios, IR signature and manoeuvrability were identified as the principal domains in which the propulsion system influences aircraft survivability. To date, no studies are available in the open literature that address both effects to measure the exact effect of propulsion system performance on aircraft survivability, with research work being exclusively focused on either the one domain or the other. In the same context, aircraft IR signature

representations available in the literature are not well-suited to the intended parametric studies because either they are not accurate enough to capture the trends associated with variations in engine performance or they are based on methods that require excessive computational cost to make predictions.

Having identified the research gap around this project's research topic, Chapter 3 describes the methodological approach used to fulfil the objectives that were set.

3 PROJECT METHODOLOGY

This Chapter describes the methodology used in the context of this project. The result is a computational framework allowing for the multidisciplinary performance analysis of military aircraft/engine configurations, in accordance with the objectives set in Chapter 1; the outline of the project structure is shown in Figure 3.1.

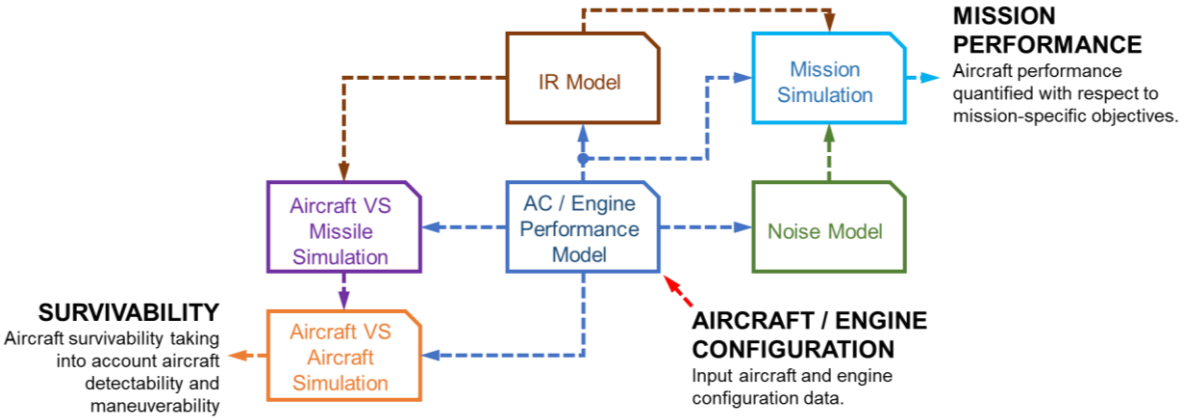

Figure 3.1: Project modular structure

The project comprises six separate modules which are interconnected to produce estimates of the expected mission performance and combat survivability for candidate configurations. These calculations use the outputs of aircraft and engine performance, IR and noise signature models, fed to simulation-based processes which translate them into mission-based quantitative objectives as shown in Figure 3.1.

The aircraft and engine performance models are parametrizable in order to adapt the corresponding models to the requirements the intended case study. The same also applies to all the simulation-based performance assessment modules in which it is possible to adjust the conditions of the scenarios being simulated; in the case of the mission simulation module, full mission profiles can be specified, meaning that it is possible to model multiple mission types and apply performance criteria adapted to the requirements of each particular case.

3.1 Aircraft Model

Figure 3.2 shows the block diagram and associated data flow of the aircraft performance model that was set-up for the scopes of this project. This comprises three separate blocks accounting for aircraft aerodynamics, engine performance and throttle-dependent aerodynamic interference effects respectively. The aerodynamic and interference blocks generate drag estimates which are combined with the thrust output from an engine performance model to predict aircraft longitudinal acceleration as a function of flight conditions, aircraft configuration and the engine's control input. The engine model estimates engine performance at the specified flight conditions; the calculated engine off-design operating point is also exported and used as input to the aircraft noise and IRSL prediction models. A more detailed description of these models' structure is given in the subsequent paragraphs.

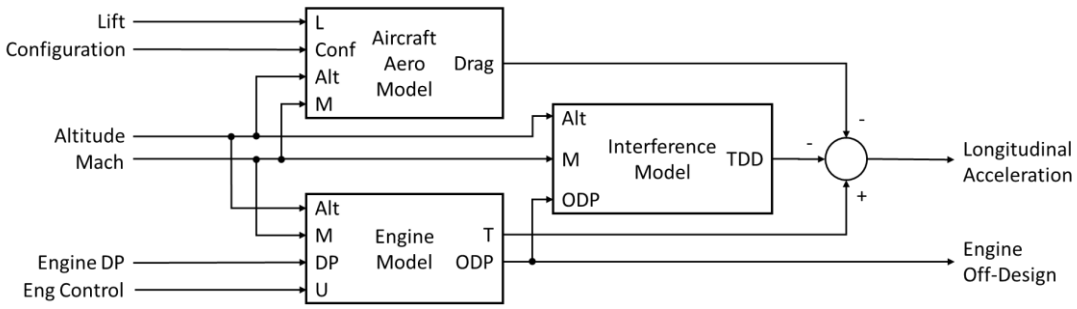

Figure 3.2: Block diagram of the aircraft performance model showing the data flow between the aircraft, engine and interference modules

3.1.1 Aircraft Aerodynamic Model

An aircraft aerodynamic representation was constructed by exploiting the data available in references [19, 21]. The latter were used to model the relation between the aircraft's lift and drag coefficients, in a lookup-table format. The effect of external store installations was modelled using the drag index system [12], combined with the data of reference [117], to produce realistic representations of actual store configurations. The use of this approach allows

for configurations including several external stores to be modelled by simply adding up the drag index values of individual stores; some indicative drag indices of widely-used aircraft stores are included in Table 3.1.

Based on its original formulation, the drag index system is limited to subsonic Mach numbers. However, in the present study, the concept's use was also expanded to the supersonic regime, under the following assumptions:

- Individual store drag coefficient follows the same distribution with altitude and flight Mach number as the aircraft's zero-lift drag coefficient (geometric similarity).
- Flow interference effects between the store and the airframe are neglected. (linear superposition)

Careful use of the above assumptions is required in order to ensure model validity. In the general case, however, due to the significant drag penalties imposed along with structural considerations, aircraft flying supersonic missions are restricted to minimal store carriage comprising mostly missiles for which the above assumptions can be considered as valid. Figures 3.3 and 3.4 present the resulting variation of aircraft aerodynamic performance as a function of flight conditions and the configuration's drag index value. The low lift-to-drag ratio, typical of military airframes, can be observed along with the drop in aerodynamic performance in the transonic region. External store installations are also shown to have a significant effect on aircraft performance: the installation of two 370-gallon external tanks (DI=9.8) imposes an 11% penalty to the aircraft's maximum lift-to-drag ratio.

Table 3.1. Store drag indices [117].

Store	Drag Index
$Mk\ 81\ LDGP\ bomb$	0.8
$Mk\ 82\ LDGP\ bomb$	1.6
$Mk\ 83\ LDGP\ bomb$	2.6
$370\ gallon\ external\ tank$	4.8
$AIM-9\ missile$	2.2
$AIM-7\ missile$	2.6

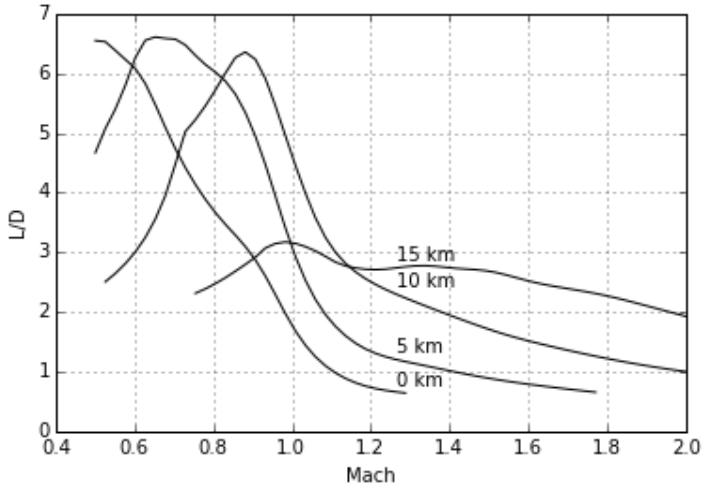

Figure 3.3: Variation of aircraft lift to drag (L/D) ratio as a function of flight Mach number and Altitude

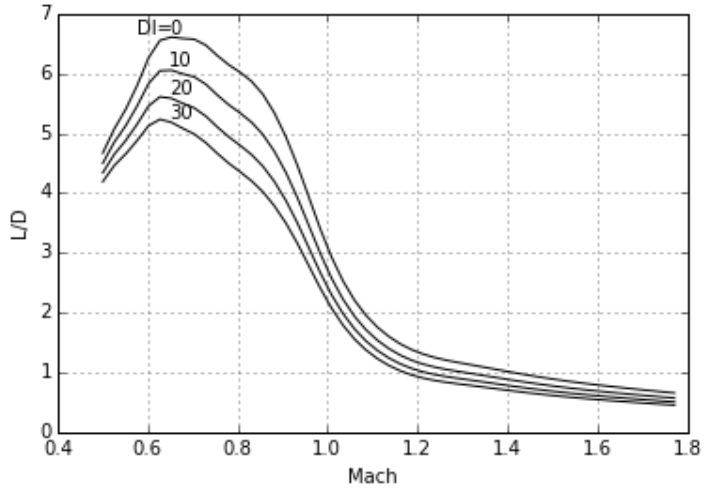

Figure 3.4: Variation of aircraft lift to drag ration with configuration drag index (DI) at an altitude of 5,000 m

3.1.2 Engine Model

A twin-spool low-bypass ratio afterburning turbofan engine configuration was used for the engine models in the context of this project, using a 0-D approach for performance simulation. Engine modelling was performed with Cranfield University's in-house engine performance code, TURBOMATCH, which is a

software-based Gas Turbine performance simulation tool developed by the Propulsion Engineering Centre at Cranfield University [73, 115].

Each model was specified as a combination of thermodynamic models of components, as per Figure 3.5 and Figure 3.6, which also show the numbering convention that was employed in this report.

- Low (LPC) and High-Pressure Compressor (HPC) were modelled using high-pressure axial-flow compressor maps available in Turbomatch. Design-point pressure ratio and isentropic efficiency were used as input variables to the engine model, to account for simulating different engine configurations. Variable stator geometry was implemented to the HPC model to provide an additional means for scheduling engine operating points for different flight conditions. An 1% bleed was assumed at the compressor outlet, to account for the turbine cooling flow requirement. As a first approach, to retain simplicity, bleed air flow for supporting the operation of airframe systems (fuel tank pressurization and air-conditioning) was not taken into account considering that it can be easily added to the model during further work on the project.
- Combustion (CC) and Afterburner (ABC) Chambers were parameterized using combustion efficiency and pressure loss. Total pressure loss was specified as a percentage of the total pressure at the inlet of the combustor. The corresponding combustion outlet temperatures were selected to reflect the modelled engines' material technology.
- Low (LPT) and High-Pressure (HPT) Turbines were modelled using fixed-geometry, low-enthalpy-drop turbine maps available in Turbomatch, and varying design-point isentropic efficiency to account for different engine configurations.
- A fully-variable convergent-divergent nozzle (N) was used, to allow for optimizing the engine off-design performance for different operational objectives under various operational conditions.
- The twin spool configuration was retained for all engine models used in this study, with the sole exception of the J79 turbojet engine model for

which a single spool was specified. Models inspired from the EJ200 and J79 engines were used as the basis for the engine configurations in this study; their design point (DP) specifications are presented in Table 3.2.

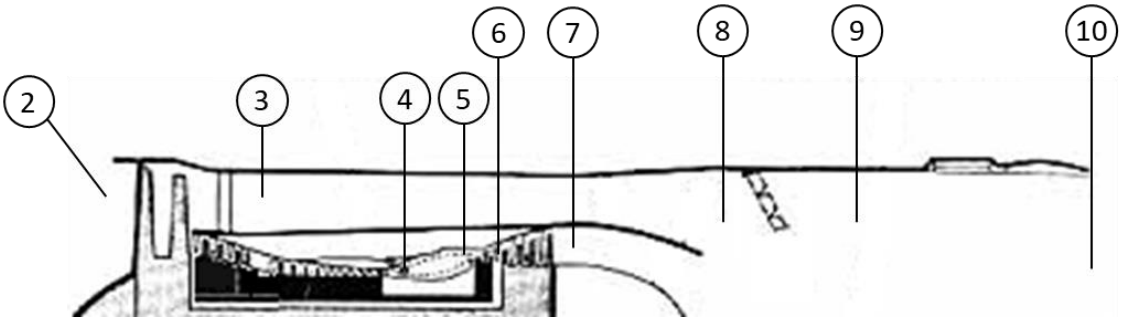

2. LP Compressor Inlet
3. LP Compressor Outlet
4. HP Compressor Outlet
5. Combustor Outlet
6. HP Turbine Outlet
7. LP Turbine Outlet
8. Mixer Outlet
9. Afterburner Outlet
10. Nozzle Outlet

Figure 3.5. Engine station numbering

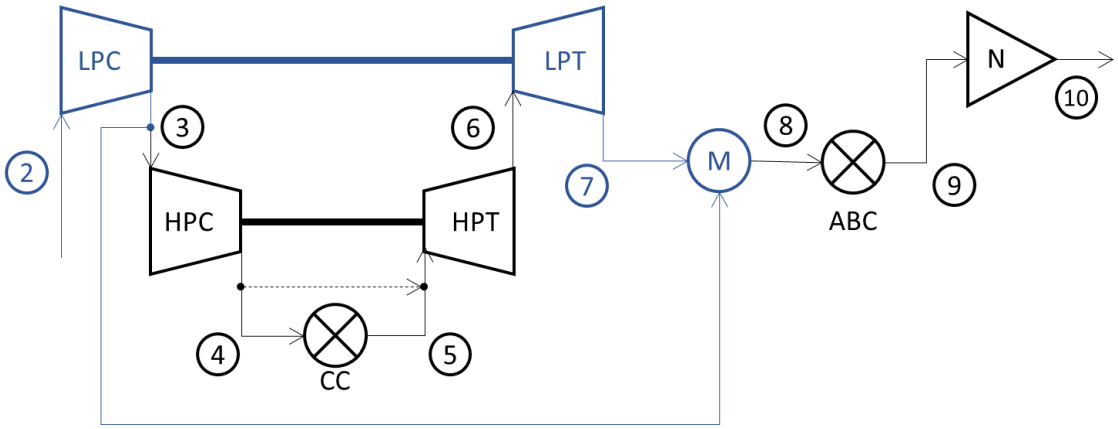

Figure 3.6. Block diagram of the engine model. The parts in blue correspond to items specific to the twin-spool turbofan configuration, whereas the black blocks are shared between the twin-spool turbofan and the single-spool turbojet models

Table 3.2. Design Point Parameters of reference engine models

Component	Parameter	EJ200	J79
LPC	Pressure Ratio	4.2	-
	Isentropic Efficiency	0.88	-
HPC	Pressure Ratio	5.9	13.5
	Isentropic Efficiency	0.87	0.84
	Bleed Extraction	1%	1%
	VSV angle	0-20 deg	0-20 deg
Combustion Chamber	Combustion Efficiency	0.99	0.98
	Pressure Loss	5%	5%
	Max Combustion Temperature	1750 K	1400 K
HPT	Isentropic Efficiency	0.89	0.85
LPT	Isentropic Efficiency	0.9	-
Mixer	Pressure Loss	1%	-
A/B Chamber	Combustion Efficiency	0.9	0.88
	Pressure Loss	5%	5%
	Max Combustion Temperature	2000 K	1800 K
Engine DP (SL Static Conditions)	Air Mass Flow	76 kg/s	76 kg/s
	Bypass Ratio	0.4	0
	Thrust	90.2 KN	75.7 KN
	SFC	43.6 mg/N.sec	47.1 mg/N.sec

3.1.3 Interference Model

The aerodynamic interaction between the engine and the airframe was modelled using an interference model outputting estimates for inlet and afterbody force as function of the flight conditions and engine operating point.

A simple model for inlet drag was adopted, assuming a dual-shock fixed-geometry inlet configuration, which is typical of modern multi-mission fighter jets. Data from Reference [118] were used to construct a model for the spillage drag coefficient as a function of flight Mach number and Inlet Capture Ratio (ICR), as per Figure 3.7. ICR is defined as the ratio between the cross-sectional area of the stream tube corresponding to the air mass flow captured (A_0) by the intake and the geometrical intake area A_H.

$$ICR = \frac{A_0}{A_H} \tag{3-1}$$

Inlet pressure distortion was not modelled through the developed interference model but was instead implemented directly to the engine model by altering the inlet pressure recovery with flight Mach number, in accordance with specification MIL-E-5007 [119].

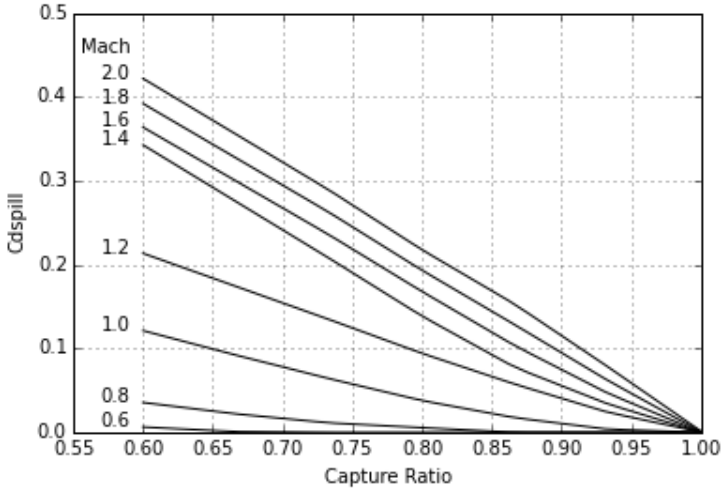

Figure 3.7: Variation of spillage drag coefficient with flight Mach number and inlet capture ratio

Since most military aircraft engines employ variable-geometry nozzles, a more detailed methodology was selected for modelling throttle-dependent forces on the aircraft afterbody, which was assumed to be of conical shape, neglecting the interference caused by neighbouring aerodynamic surfaces and flow control devices.

Aerodynamic modelling was based upon computer routines developed to illustrate the methods of ESDU items 01012 [120], 00017 [121] and 99010 [122] for any afterbody configuration within their range of applicability. ESDU item 99010 was used for the subsonic and low-transonic region and items 00017, 99010 for supersonic calculations above Mach 1.3. A fairing between the two methods was employed for calculations in the region between Mach 0.95-1.3, based on the typical variation of aircraft drag coefficient for the same Mach number interval.

The resulting model was cross-validated against the worked examples of the same references and its output was qualitatively assessed based on the findings from the literature survey (Section 2.2.1).

Calculated values of the afterbody drag coefficient as a function of Mach number, Nozzle Pressure Ratio and Afterbody boattail angle are presented in Figures 3.8 and 3.9 respectively. In both Figures, the boattail drag coefficient displays a similar relation to flight Mach number as the aircraft drag coefficient: An approximately constant value of the coefficient in the subsonic region is followed by a steep increase in the transonic Mach number range, reaching a maximum at approximately Mach = 1 and with the drag coefficient's value slowly dropping as the Mach number is further increased.

Higher boattail angles result in higher values of the boattail drag coefficient, as expected, due to the separation induced by the adverse pressure gradient caused by the steep reduction in cross-sectional area of the axisymmetric afterbody geometry (Figure 3.8). This effect has a very strong influence on boattail drag which experiences a 62% increase at low Mach numbers for a change in boattail from 6 to 20 degrees. At transonic Mach numbers this

increment is significantly magnified with afterbody drag reaching 688% of its original value for the same variation in afterbody angle.

In the same context, the effect of pluming is clearly observable in Figure 3.9, resulting in a consistent reduction in afterbody drag with increasing nozzle exit pressure ratio. At high enough values of the latter it is possible for afterbody drag to become negative i.e. to be converted to an additional pressure thrust component exerted over the afterbody's convergent section; this phenomenon was observed to be stronger at high subsonic Mach numbers and low values of boattail angle, in which cases afterbody drag became negative for nozzle exit pressure ratios higher than 1.8. The combined effect of the throttle dependent forces was calculated at approximately 5% of the total aircraft drag for both subsonic and supersonic cruise conditions.

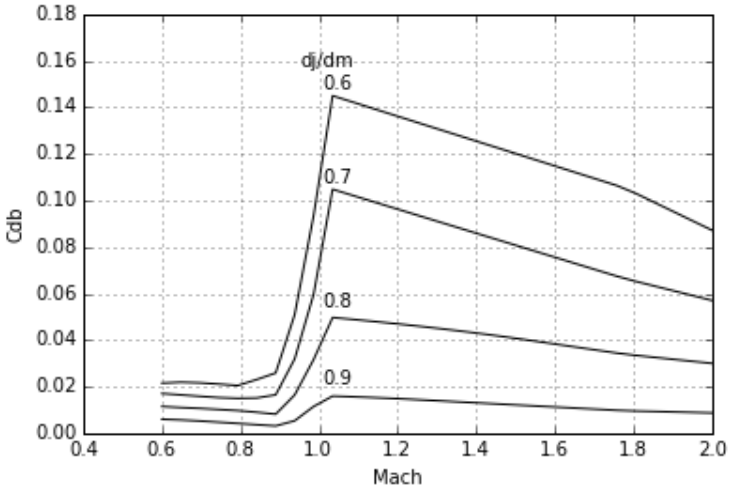

Figure 3.8: Variation of afterbody drag coefficient with nozzle exit-to-inlet diameter ratio; Pj=Pamb=1 bar, Tj=600 K, Tamb=288 K, Mj=1. Afterbody length is 1 m.

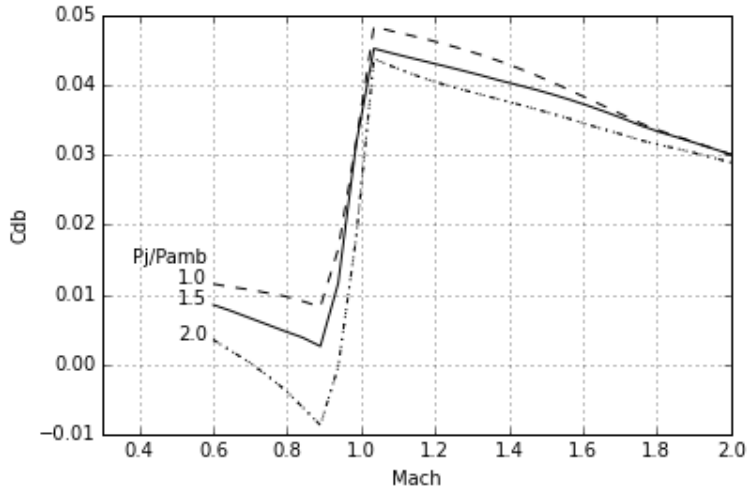

Figure 3.9: Variation of afterbody drag coefficient with nozzle exit pressure ratio; dj/dm=0.8, Tj=600K, Tamb=288 K, Mj=1.5. Afterbody length is 1 m.

3.2 IR Signature Model

The aircraft IR signature model that was developed as part of this project is used to generate estimates of the distribution of aircraft IR emissions in the space surrounding the airframe as a function of the flight condition and engine operating point, to quantify the influence of the latter on aircraft detectability in the IR spectrum, a wavelength commonly used by weapon sensors in aerial warfare. Aircraft IR emissions are a function of multiple factors, which need to be accounted for in order to produce a realistic aircraft representation. To explain the methodology used for the development of the aircraft IR model, some of the equations originally presented in Chapter 2 will be used and, for convenience of the reader, are repeated in Table 3.3.

Table 3.3: Recapitulation of IR radiation equations from Chapter 2.

$N = \frac{1}{\pi}\int_{\lambda_1}^{\lambda_2} W(\lambda)d\lambda$	(2-4)
$H = \frac{A}{\pi R^2}\int_{\lambda_1}^{\lambda_2} W(\lambda)\tau(\lambda)d\lambda$	(2-5)
$H_c = \left(N - N_{bgd}\right)\tau\frac{A}{R^2}$	(2-6)
$R_{LO} = \sqrt{\frac{\tau}{\xi_{min} NEI}\iint_S \left(N - N_{bgd}\right)(\bar{x}\cdot\bar{n})dS}$	(2-9)

Equation (2-9) suggests that an IR model of a generic radiation source needs to provide estimates for the following quantities:

1. Surface temperature distribution
2. Material emittance properties
3. Projected areas for different fields of view
4. Background radiance
5. Atmospheric transmittance
6. Sensor performance

Adapting the above to an aircraft application led to the model structure of Figure 3.10. An aero-propulsive model is used to calculate the engine's operating point and the respective thermodynamic properties of the exhaust gases for the specified flight conditions and aircraft configuration. These are fed as inputs to aircraft and plume thermal models which estimate spatial temperature distributions for these components. Using Eqs. (2-4)-(2-6) in conjunction with an atmospheric model which outputs background radiance (assuming sky background) and atmospheric transmittance along the specified path, contrast

irradiance at the sensor is estimated. Finally, Eq. (2-9) can be used to obtain the aircraft's lock-on range for a given sensor.

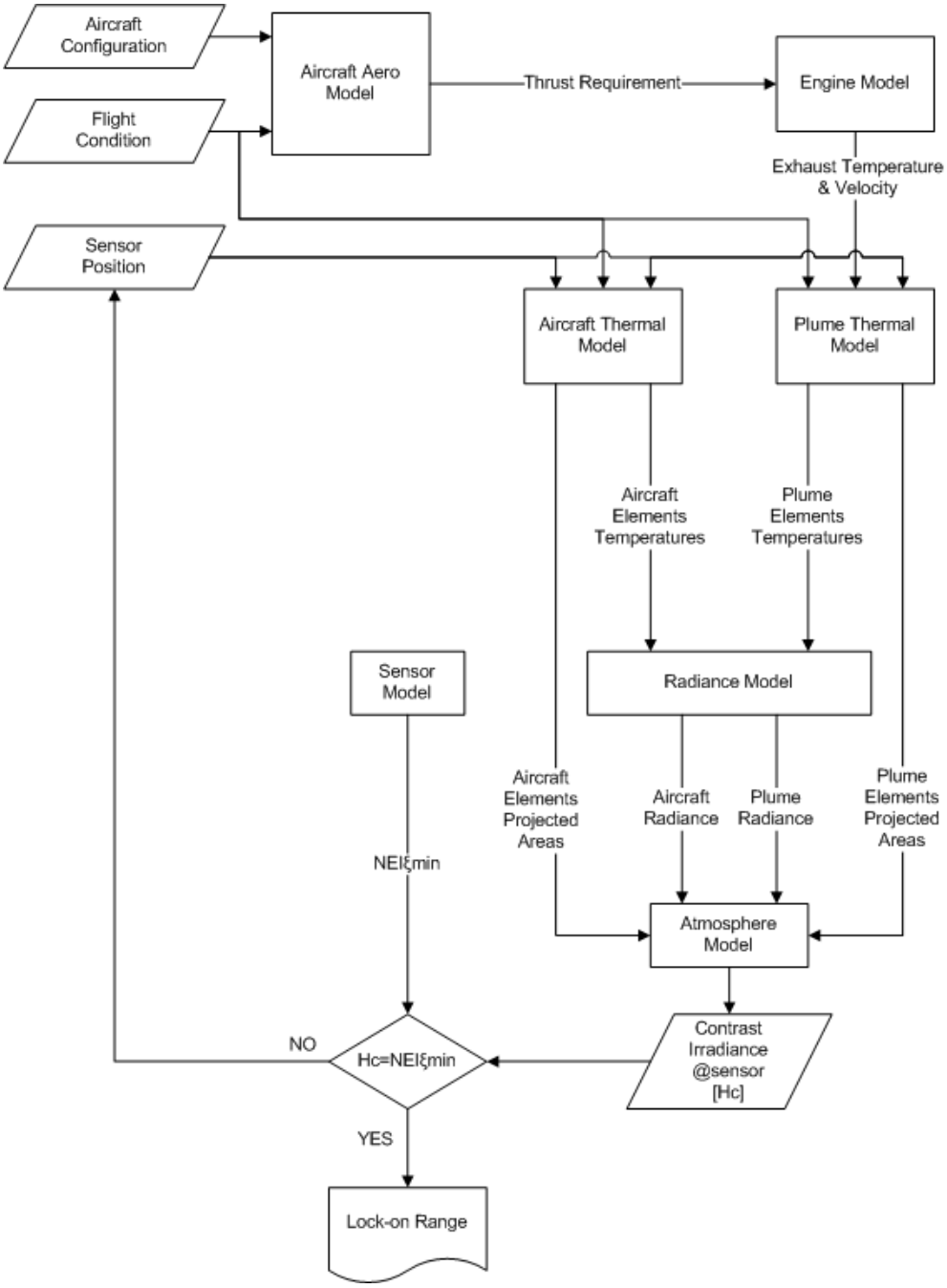

Figure 3.10: Flowchart of the procedure for estimating aircraft lock-on range

3.2.1 Aircraft and Plume Thermal Models

Estimating surface temperature distribution for an aircraft in flight requires solving heat-balance equations for the entire airframe which is a complicated task because of the complex flowfield around the aircraft, particularly at transonic and supersonic flight speeds. Researchers have frequently resorted to CFD [92-93, 123-124] to generate solutions for the aircraft heat balance problem, however, as a result of the computational intensity of the calculations involved, the data presented correspond to a limited number of operating conditions and/or do not cover the entire airframe.

With the intention to create an aircraft IR model that will generate predictions for the entire flight envelope with minimum computational requirements, a semi-empirical formulation for temperature estimation was selected. References [90, 97] suggest that the temperature of the aircraft skin can be roughly approximated as:

$$T = T_{\infty}(1 + 0.164M^2) \tag{3-2}$$

which is essentially a fraction of the flow total temperature at the specified flight condition (T_{∞}accounts for ambient temperature and M for Mach number). This value, however, can only be considered as representative of airframe areas not affected by the heat generated by the propulsion system. The latter is known to generate hot regions around the rear fuselage and the exhaust tailpipe [89]. An alternative formulation is thus required for these regions that will take into account the powerplant's heat output.

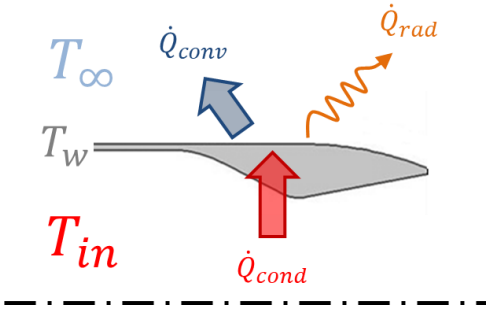

Figure 3.11: Heat Flow on the exhaust pipe

The heat balance equation for the rear fuselage section of Figure 3.11 can be written as:

$$\dot{Q}_{cond} = \dot{Q}_{conv} + \dot{Q}_{rad} \tag{3-3}$$

where $\dot{Q}_{cond}$ is the heat flux per unit area transmitted by conduction through the tailpipe's casing, $\dot{Q}_{conv}$ is the convection heat flux between the tailpipe wall and the airstream and $\dot{Q}_{rad}$ is the radiation flux. Eq. (3-3) can be written, in a more analytical form as:

$$k(T_{in} - T_w) = h(T_w - T_\infty) + \varepsilon\sigma(T_w^4 - T_\infty^4) \tag{3-4}$$

where k, h are the conduction and convection heat transfer coefficients, σ is the Stephan-Boltzmann constant and T_w is the wall temperature. The conduction heat transfer coefficient is a property of the material of the tailpipe's casing and was estimated using data for wall temperature distribution and heat flux found in references [123, 124]. The convection heat transfer coefficient h is a function of the flow conditions over the tailpipe's external surface; a script illustrating the procedure of ESDU item no 69011 [125] was developed and used to provide estimates for h in various flight conditions. The method is based upon the flow Stanton number (St):

$$St = \frac{h}{\rho V C_p} \tag{3-5}$$

where ρ is the fluid's density, C_p is the fluid's specific heat and V the flow velocity. Stanton number is a function of the wall temperature, therefore, an iterative procedure was set up to solve of Eq. (3-4) and obtain the temperature of the external tailpipe wall T_w for each operating condition. The convergence of the developed method is demonstrated in Figure 3.12. In the same Figure, the model's temperature estimate is compared with CFD data from reference [124] under identical flight conditions. External wall temperature can be observed to converge at the same values for the same boundary conditions, which can be considered as proof of the validity of the adopted method.

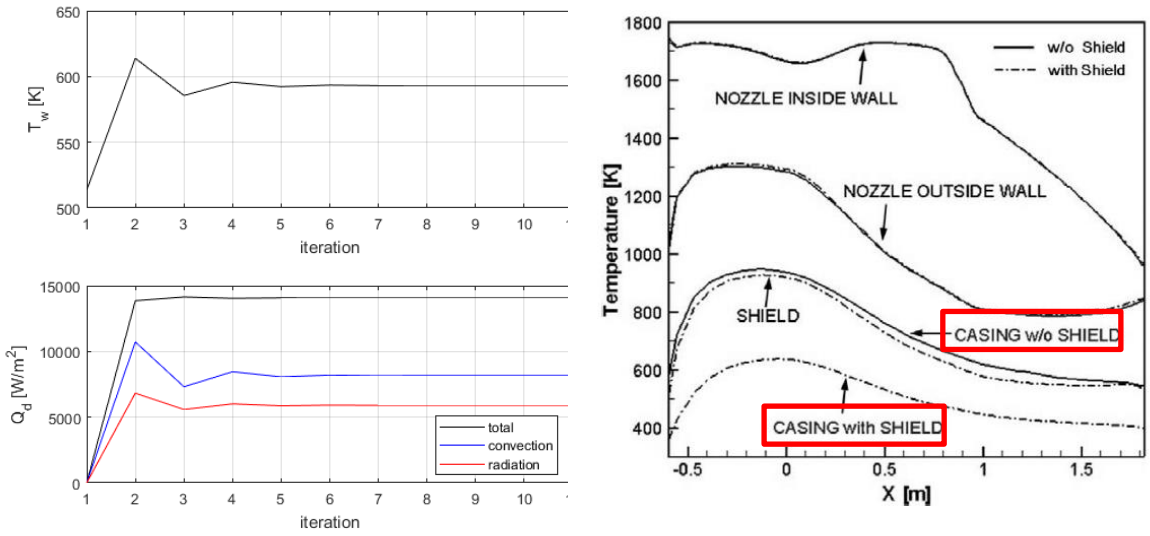

Figure 3.12: Convergence of the iterative method for tailpipe temperature estimation (left) VS temperature distributions from [124] (right).

Apart from the airframe itself, studies on the IR signature of air vehicles [126] have shown that a major contributor to a military aircraft's IR footprint is the exhaust plume formed by the exhaust gases exiting the engine's nozzle. The shape of the exhaust plume and the temperature distribution within it is a function of the internal (engine) and external (atmosphere) flow conditions in the region surrounding the exhaust nozzle. As for the case of aircraft skin temperature estimation, accurate solutions may only be generated by means of CFD, however, the computational cost of this approach makes it, by today's standards, unsuitable for parametric performance studies. Alternative approaches that are commonly used include empirical methods and the method of characteristics [127].

In the context of the present study the author resorted to a computationally inexpensive, lower-fidelity method, to allow for its implementation to air combat scenario simulations without this resulting in unacceptable simulation time. The methodology employed combines a velocity distribution model from reference [128] with turbulent jet theory [129] and engine operation data from an aircraft manual [117]. It may be summarized as follows: Reference [128] suggests that

the non-dimensional velocity ratio (VR) along the plume centerline can be expressed as a function of the corrected distance x* from the nozzle exit plane:

$$VR = \frac{V - V_\infty}{V_j - V_\infty} \sim x^* = \left[x \left(C_n D_e \sqrt{1 + M_j} \right)^{-1} \right]^b$$

$$b = 1 + \frac{1}{3} \left[\left(\frac{V_j}{V_0} \right)^2 - 1 \right]^{-1} \quad (3\text{-}6)$$

Where D_e accounts for the nozzle diameter whereas C_n is a non-dimensional coefficient whose value depends on the nozzle configuration. The use of VR to describe the exhaust flowfield is advantageous in that it can be applied to various combinations of flight velocity V_∞, exhaust velocity $V_j$and Mach number M_j at the nozzle.

Using Eq. (3-6) as a baseline, a function describing the variation of jet velocity along the plume centerline was constructed by curve-fitting on exhaust flow fields sourced from reference [117] (Figure 3.14). Following that, axisymmetric shape functions were used to form three-dimensional velocity contours based on the estimated velocities on the jet centerline, as per Figure 3.13. To account for the effects of forward velocity on the shape of the exhaust jet, as suggested by jet theory [129], the jet expansion angle β was modified according to the formula:

$$\beta = \beta_{[V_\infty = 0]} \frac{V_j - V_\infty}{V_j + V_\infty} \quad (3\text{-}7)$$

The transformation described in Eq. (3-7) introduces a ‘compression’ to the original plume shape with increasing freestream flow velocity (Figure 3.13). Abramovich [129] also suggests that local values of VR are interconnected to the respective values of the non-dimensional temperature ratio (TR).

$$TR = \frac{T - T_\infty}{T_j - T_\infty} \quad (3\text{-}8)$$

Therefore, having established the velocity distribution within the plume, an equivalent temperature distribution may be constructed in a similar manner, by curve-fitting velocity and temperature data from reference [117] (Figure 3.15).

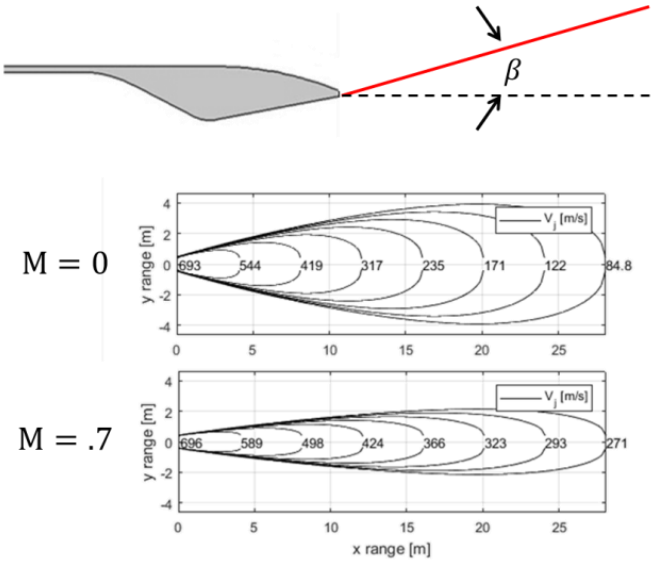

Figure 3.13: Definition of jet expansion angle (β) [top] showing the effect of forward velocity on plume shape [bottom].

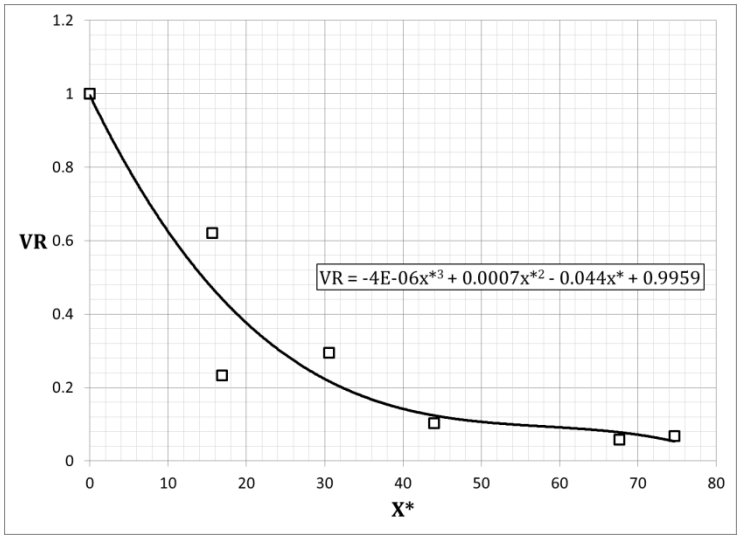

Figure 3.14: Velocity Ratio (VR) VS x^*, Max-Power data [117].

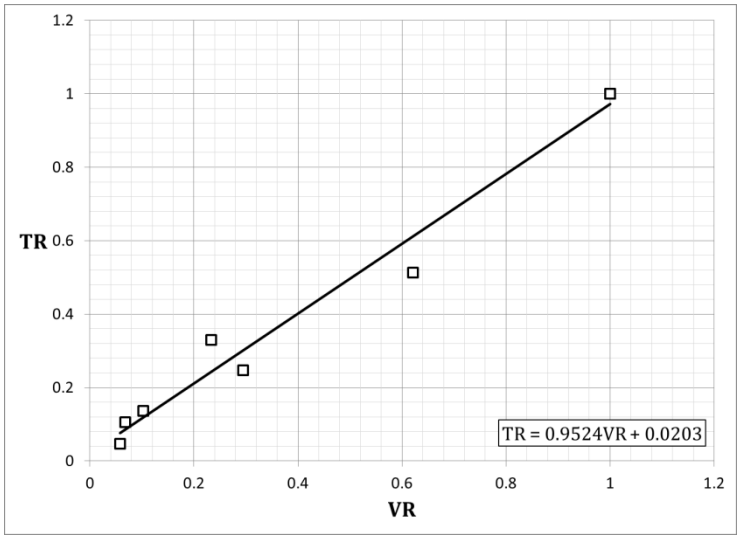

Figure 3.15: Temperature Ratio (TR) VS Velocity Ratio (VR), Max Power data [117]

For validation purposes, the predictions generated by the proposed plume model were compared against CFD solutions for fully expanded and under-expanded nozzle exit conditions [130]. The predicted temperature variation along the plume centerline was found to closely match CFD results for the fully-expanded flowfield, resulting in good accuracy in the corresponding temperature-area distribution for the same test case (Figure 3.16). As expected, the model was unable to capture the temperature oscillations present in the under-expanded nozzle solution (Figure 3.17). These are a result of complex interactions between shock waves and expansion fans occurring within the exhaust jet's inviscid core the effects of which cannot be modelled by the simplified plume representation that was selected. Despite this, temperature predictions were found to be adequately close to the actual results, showcasing a similar reduction trend to the CFD solution results with increasing distance from the nozzle exit.

The validity of the assumption for angle β was assessed by comparing the CFD plume boundary with the corresponding boundary generated by the model: Good match between the two results was observed, only limited by the proposed model's inability to capture the initial plume deflection due to the expansion taking place at the nozzle exit. Subject to the above limitations, the

proposed method's performance was deemed sufficient for the intended preliminary-level performance studies.

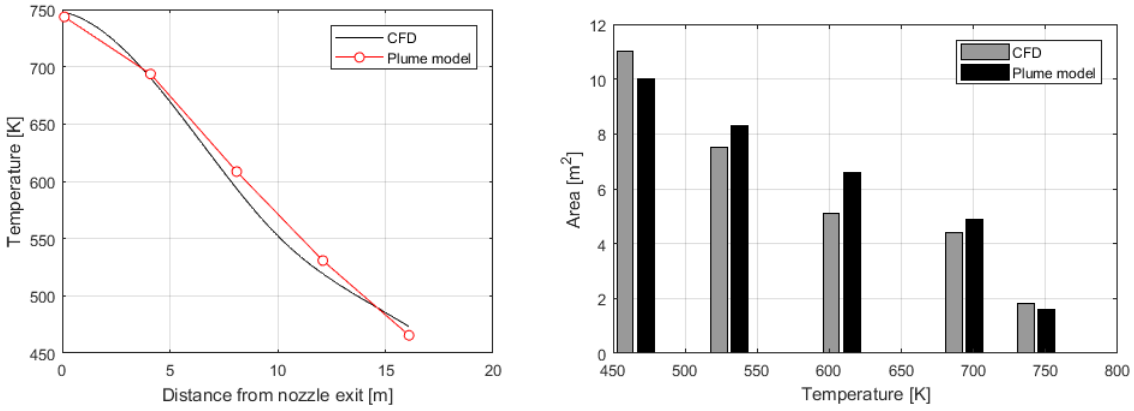

(a) (b)

Figure 3.16: Comparison of plume model predictions with CFD data for a fully expanded nozzle: (a) Jet temperature along centerline vs distance from nozzle (b) Temperature vs element area. Jet exhaust velocity is 550m/s, exhaust temperature is 750 K, ambient temperature 288 K and flight Mach number 0.9.

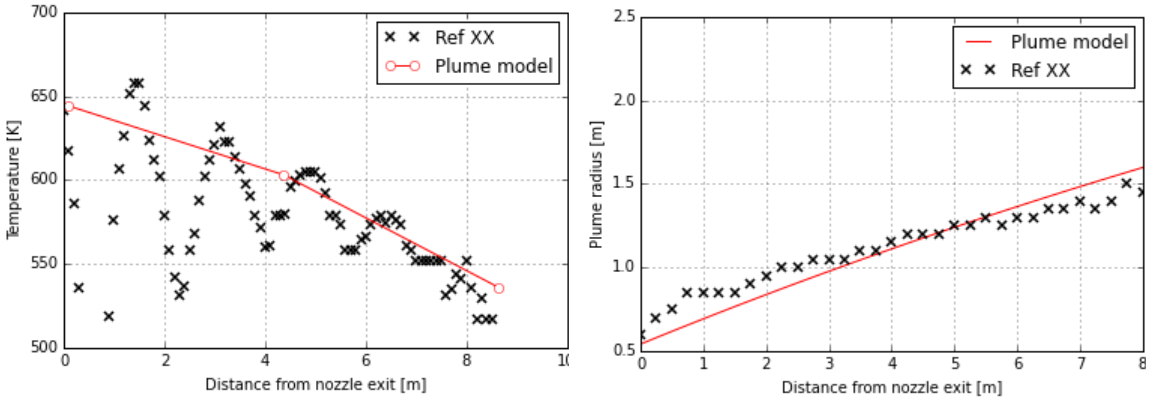

(a) (b)

Figure 3.17: Comparison of plume model predictions with CFD data for an under-expanded nozzle from reference [130]: (a) Jet temperature along centerline vs distance from nozzle (b) Plume width vs distance from nozzle. Jet exhaust velocity is 605m/s, exhaust temperature is 645 K, ambient temperature 212 K and flight Mach number 0.6.

3.2.2 Estimation of component projected areas

According to Eq. (2-5), the total irradiance generated at the sensor is proportional to the projected area of each radiating component. Therefore, aside temperature estimates, component area estimates should also be as realistic as possible in order to obtain physically correct results in terms of the distribution of IR radiation levels around the aircraft. Whereas aircraft and plume geometries can be reduced to very simple shapes (for example, reference [97] uses a 'shoebox' aircraft model and reference [131] models the exhaust plume as two concentric cylinders) while retaining some accuracy on the projected area estimates from different fields of view, such an approach fails to capture the exact effects of overlaps between them which are fundamental for aircraft IR: When viewed from the front, it is known that the aircraft body hides most of the engine's exhaust plume from an IR sensor, however, depending on the engine operating condition, some lower-temperature regions may still be visible to the sensor and affect the detection range. The same also applies to aircraft side views in which the visibility of high-temperature components is subject to features of the aircraft geometry such as wing span and the location of the empennage with respect to the engine tailpipe.

Based on the above, it was decided to develop a realistic aircraft representation using an open-source 3D CAD design of a generic airframe and use it to obtain accurate area estimates. In this context, a surface grid was generated in CATIA V5 and was used in conjunction with the plume model of the previous paragraph to calculate projected areas for the airframe components and the exhaust plume. The general layout of the airframe grid is shown in Figure 3.18.

The calculation process aims to identify visible airframe-plume elements and sum-up their projected areas for a given sensor position. To do so, for each element of the aircraft and plume surface grid, a Line-Of-Sight (LOS) vector L needs to be constructed, interconnecting the element's centroid with the sensor location; the element's visibility to the sensor may then be evaluated by

checking if the LOS line intersects the aircraft wireframe, not including the element itself, as shown in Figure 3.19.

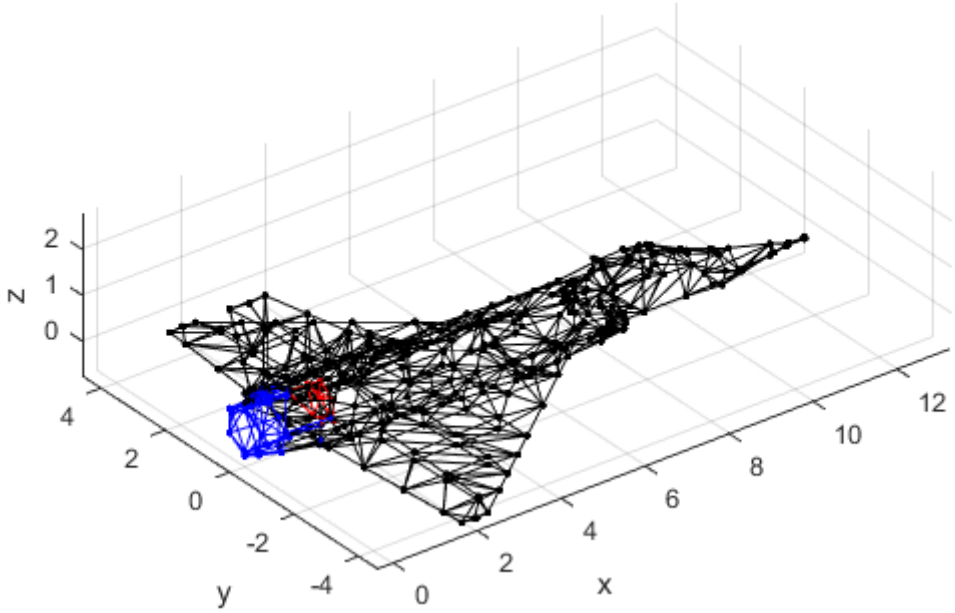

Figure 3.18: Overview of the aircraft surface grid used for calculating airframe projected areas for IR signature estimation. The blue, red and black-colored regions correspond to aircraft tailpipe, turbine face and skin respectively.

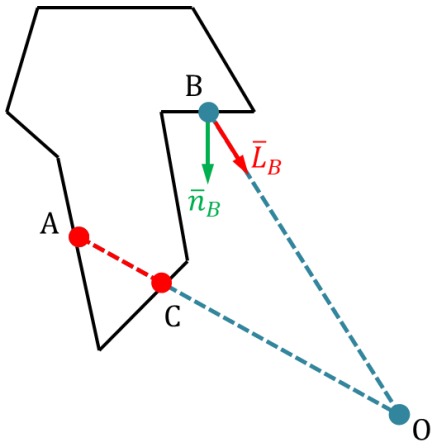

Figure 3.19: Procedure to assess the visibility of surface elements (shown as edges in this 2D example) to a sensor located at point O. Line segment AO intersects the body's surface at point C, therefore point A is not visible from point O.

In case that no intersections occur, the projected area of the element equals:

$$A_{p_i} = A_i(\bar{n}_i^T \bar{L}_i) \tag{3-9}$$

where A_i, n_i and L_i are the element's total area, normal vector and normalized LOS vector respectively. For a sensor located at point $\bar{x}_s$, the following procedure is used to check whether the LOS line of element i intersects element j:

1. Calculate the intersection between the plane defined by the surface element j and the LOS line. If $\bar{n}_j$ is the normal vector of element j and $\bar{x}_{0j}$ the position vector of its centroid, then the equation of the plane containing element j is:

$$\bar{n}_j^T \bar{x} = \bar{n}_j^T \bar{x}_{0j} \tag{3-10}$$

In a similar manner, if $\bar{x}_1$, $\bar{x}_2$ are two random vectors normal to the LOS vector $\bar{L}_i$, the LOS line of element i can be defined as the intersection of two planes:

$$\begin{bmatrix} \bar{x}_1^T \\ \bar{x}_2^T \end{bmatrix} \bar{x} = \begin{bmatrix} \bar{x}_1^T \\ \bar{x}_2^T \end{bmatrix} \bar{x}_{0i} \tag{3-11}$$

Combining Eqs. (3-10) and (3-11) the intersection point $\bar{x}_C$ can be calculated:

$$\bar{x}_C = \begin{bmatrix} \bar{n}_j^T \\ \bar{x}_1^T \\ \bar{x}_2^T \end{bmatrix}^{-1} \begin{bmatrix} \bar{n}_j^T \bar{x}_{0j} \\ \bar{x}_1^T \bar{x}_{0i} \\ \bar{x}_2^T \bar{x}_{0i} \end{bmatrix} \tag{3-12}$$

2. Check if intersection $\bar{x}_C$ lies between $\bar{x}_{0i}$ and $\bar{x}_s$. This statement holds if:

$$(\bar{x}_C - \bar{x}_S)^T \bar{L}_i < 0 \cap (\bar{x}_C - \bar{x}_{0i})^T \bar{L}_i > 0 \tag{3-13}$$

If the condition of Eq. (3-13) is not true, the LOS line of element i does not intersect element j. Otherwise, proceed to next step.

3. Check if intersection $\bar{x}_C$ is an internal point of element j. Let $\bar{n}_k$ be the normal vector of an edge of element j and $\bar{M}_k$its midpoint, as shown in Figure 3.20. Under the assumption that element j is convex, point $\bar{x}_C$ is internal to element j if:

$$(\bar{x}_C - \bar{M}_k)^T \bar{n}_k < 0 \quad \forall\, k \in [1, N] \tag{3-14}$$

where N accounts for the number of edges of element j. If $\bar{x}_C$ is internal to element j, then the LOS line of element i intersects element j.

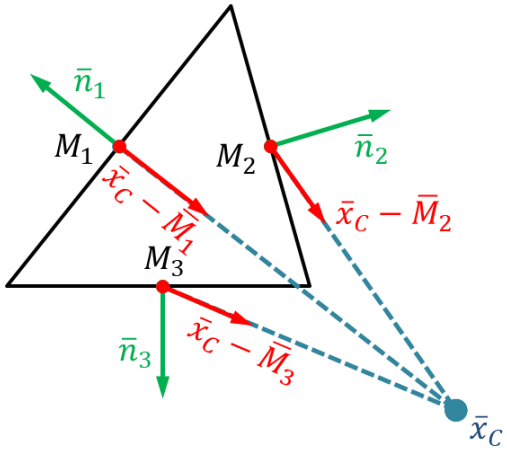

Figure 3.20: Geometry for checking if point $\bar{x}_C$ is internal to a triangular surface element.

Repeating the above procedure for all surface elements' combinations allows for the calculation of the projected areas of the airframe and plume; some example results are shown in Figure 3.21.

To reduce the computational intensity of future IR signature calculations, the spatial domain around the aircraft and plume was parametrized using spherical coordinates and multiple runs were conducted to calculate and store the projected area values of the three specified airframe regions. Conversion from the Cartesian axis system of Figure 3.21 to a spherical system was made by introducing angles θ and φ, defined as follows:

$$r = \sqrt{x^2 + y^2 + z^2}$$

$$\theta = arccos\left(\frac{z}{r}\right)$$

$$\varphi = arctan\left(\frac{y}{x}\right) \quad (3\text{-}15)$$

Stored values were organized in a look-up table format which can be used to generate the area values required for IR calculations with minimum computational cost. This assumes that the projected area values are not a function of the distance between the sensor and the airframe, which can be considered as valid for distances in the order of typical aircraft lock-on ranges. The same approach was not applied to plume projected areas, because plume geometry is a function of the flight conditions and engine setting and, therefore, results are harder to generalize.

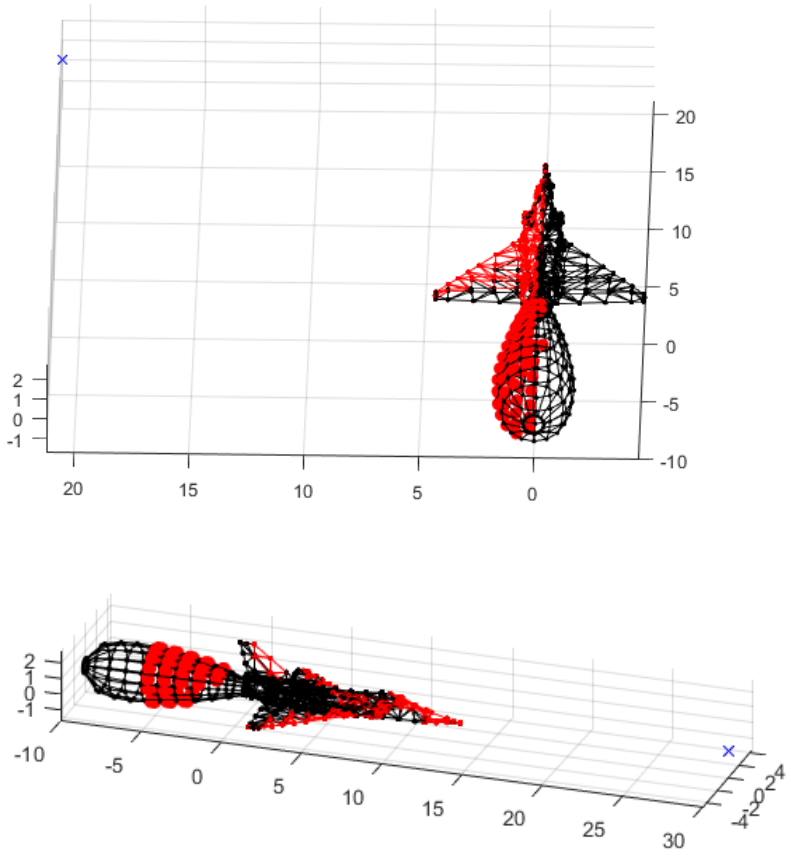

Figure 3.21: Calculated airframe and plume visible areas (marked in red) with respect to a sensor (blue cross) located at aspect angles of 45º (top) and 0º (bottom).

A test run of the developed IR model was conducted with the objective of finding the bounds of the lock-on envelope for an aircraft cruising at 1000 m altitude, Mach 0.6. Sensor sensitivity was set to $10^{-6}\,W/m^2$, roughly averaging the respective values from references [91, 97] and the plume emittance model from Baqar [131] was employed. Results are presented in Figures 3.22 and 3.23. The distribution of the IR signals from all sources comprising the IR model were compared to data from reference [132] and were found to follow a similar distribution (Figure 3.22). Qualitatively, in common with the results of Kim et al [93] and Mahulikar et al. [91], the calculated envelope is apple-shaped, with the lowest value of the lock-on range occurring at the aircraft front, as expected due to the combined effects of reduced projected area and plume masking. In terms of magnitude, the lock-on range is close to a value of 3-5 km for cruise and 15-25 km for Max A/B operation (Figure 3.23), which, based on the author's own experience as a military aircraft engineer and pilots' feedback can be considered as typical for the specified flight conditions and a 'standard' IR sensor.

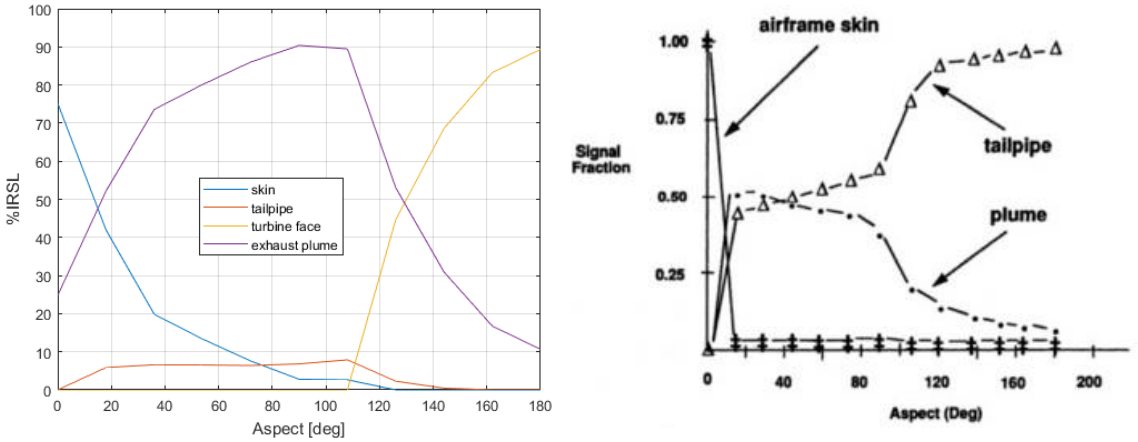

Figure 3.22: Calculated distribution of IRSL with aspect angle for various aircraft components for an aircraft cruising at Mach 0.6 and Altitude 1000m (Left) VS data from reference [132] (Right).

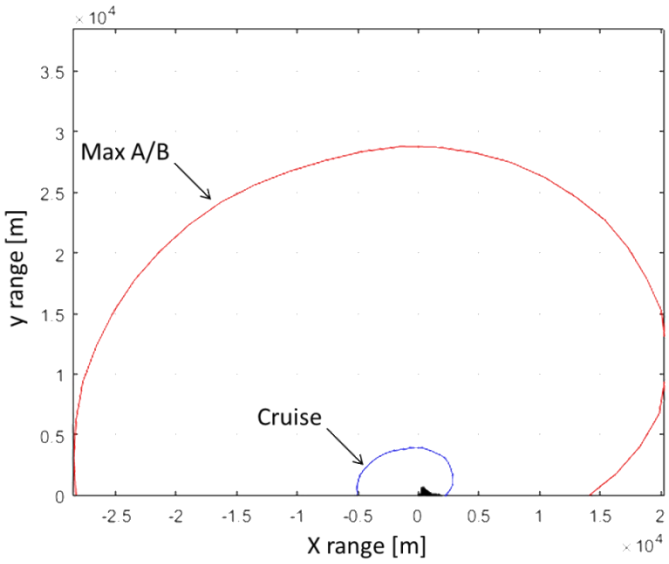

Figure 3.23: Estimated cruise and Max A/B lock-on envelopes at Mach=0.6, Alt=1,000m

3.3 Noise Model

Fighter aircraft are designed for high speed and combat performance and are as a result very noisy on operation. According to the findings of AGARD-CP-512 [133], the high levels of noise generated by fighter aircraft are increasingly perceived as a nuisance by populations in the proximity of military airbases and training areas. However, despite the changes that have been introduced to commercial aircraft to reduce the impact to local societies during the last decades, the evolution of military aircraft is towards a rather different direction: as far as engines are concerned, a constant demand for increased thrust and reduced size has led to a rise in exhaust velocity which is a major contributor to the engines' sound footprint (according to Lighthill's theoretical study [134-135], the acoustic power of jet noise is proportional to V_j^8).

Although it appears that noise reduction does not currently represent a design trend for military engines, effort has been placed towards gaining understanding of the physical mechanisms associated with noise generation [133]. In this context, various methods for the prediction of aircraft noise have been

developed, applicable to both civil and military aircraft; these among others include NASA's ANOPP [136] and the Swiss FLULA [137] noise prediction programs while the same topic is also covered by a number of SAE standards and ESDU items [138-141]. As far as the aims and scope of the present project are concerned, the implementation of a noise prediction model was selected in order to obtain an estimate of the public annoyance levels associated with conceptual aircraft/engine configurations

To retain simplicity, the developed aircraft noise model considers only the effects of the two main sources of acoustic signals associated with military aircraft, namely the jet noise generated by the turbulent mixing of the engine exhaust gases with the atmosphere and the sonic boom, which originates from shock waves formed around aircraft traveling at supersonic speed. The model's general structure is shown in Figure 3.24. Given the small fan diameter and the acoustic shielding provided by the typically long intake system of military aircraft, fan noise was not considered in the calculations performed. A brief description of the methods used is given in the following paragraphs.

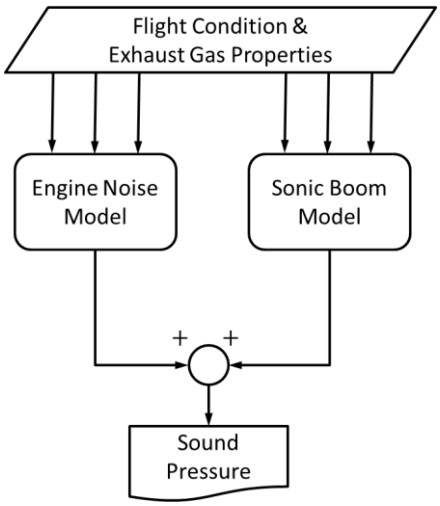

Figure 3.24: Block diagram of the aircraft noise prediction model

3.3.1 Jet Noise Prediction

The prediction method developed by Stone [142-144] for NASA's widely-used ANOPP program was selected for modelling jet noise. According to the latter,

the Overall Aircraft Sound Pressure Level that is generated by an exhaust jet, uncorrected for refraction ($OASPL'$) is given in dB by:

$$OASPL' = 141 + 10log\left[\left(\frac{\rho_a}{\rho_{ISA}}\right)^2\left(\frac{c_a}{c_{ISA}}\right)^4\right] + 10\log\left(\frac{A_j}{R^2}\right) + 10\omega\log\left(\frac{\rho_j}{\rho_a}\right) +$$

$$75\log\left(\frac{V_j}{c_a}\right) - 15log[(1 + M_0 cos\theta)^2 + a^2 M_0^2]$$

$$\omega = \frac{3\left(\frac{V_j}{c_a}\right)^{3.5}}{0.6+\left(\frac{V_j}{c_a}\right)^{3.5}} - 1 \qquad (3\text{-}16)$$

Where:

ρ_α	=	local atmospheric density
ρ_{ISA}	=	ISA density
c_a	=	local speed of sound
c_{ISA}	=	ISA speed of sound
A_j	=	jet area
R	=	distance from nozzle
ρ_j	=	jet density
M_0	=	flight Mach number
M_j	=	jet Mach number
V_0	=	flight velocity
θ	=	angle from inlet axis
β	=	secondary angle from inlet axis
a, k	=	constants

The OASPL of an aircraft in flight can be obtained by inserting a series of correction factors accounting for different phenomena:

$$OASPL_F = OASPL' + \Delta_R + \Delta_K + \Delta_D + \Delta_{So} \qquad (3\text{-}17)$$

Definitions and formulas for the correction terms of Eq. (3-17) are given in Table 3.4. For under-expanded exhaust nozzles, the presence of shocks acts as

additional source of noise. The equivalent OASPL accounting for shock-generated noise can be calculated as follows:

$$OASPL_S = 162 + 10log\left[\left(\frac{\rho_a}{\rho_{ISA}}\right)^2\left(\frac{c_a}{c_{ISA}}\right)^4\right] + 10\log\left(\frac{A_j}{R^2}\right) + 10log\left[\frac{\left(M_j^2-1\right)^2}{1+\left(M_j^2-1\right)^2}\right]$$

$$- 10log\left[1 - M_o\cos(\theta+\beta) + F(\theta-\theta_M\right]$$

$$\theta_M = 180^o - arcsin\frac{1}{M_j}$$

$$F = \begin{cases} 0 & \theta \le \theta_M \\ 0.75 & \theta > \theta_M \end{cases} \qquad (3\text{-}1)$$

Table 3.4. Definition of OASPL correction factors.

Symbol	Definition	Value
Δ_R	Refraction Correction	$in\ tabular\ form$
Δ_D	Kinematic Effect	$\Delta_K = -10\log[1 - M_o\cos(\theta+\beta)]$
Δ_D	Dynamic Effect	$\Delta_D = -15log\left\{\frac{\left[1+k\left(\frac{V_j-V_o}{c_a}\right)cos\theta\right]^2 + a^2k^2\left(\frac{V_j-V_o}{c_a}\right)^2}{\left[1+k\left(\frac{V_j}{c_a}\right)cos\theta\right]^2 + a^2k^2\left(\frac{V_j}{c_a}\right)^2}\right\}$
Δ_{So}	Source Strength Alteration	$\Delta_{So} = 50log\left(1-\frac{V_o}{V_j}\right) + 10\left\{\frac{3\left[\left(\frac{V_j}{c_a}\right)\left(1-\frac{V_o}{V_j}\right)^{\frac{2}{3}}\right]^{3.5}}{0.6+\left[\left(\frac{V_j}{c_a}\right)\left(1-\frac{V_o}{V_j}\right)^{\frac{2}{3}}\right]^{3.5}} - \frac{3\left(\frac{V_j}{c_a}\right)^{3.5}}{0.6+\left(\frac{V_j}{c_a}\right)^{3.5}}\right\}\log\left(\frac{\rho_j}{\rho_a}\right)$

The total OASPL generated by the exhaust jet can be calculated by means of antilogarithmic addition of basic OASPL with $OASPL_S$:

$$OASPL_T = 20\log\left(\frac{P_{OASPL}+P_{OASPL_S}}{P_{ref}}\right) \qquad (3\text{-}2)$$

where $P_{OASPL}$and P_{OASPL_S} are the RMS sound pressure values corresponding to OASPL and OASPLs respectively, while P_{ref} is the reference sound pressure. Figure 3.25 shows an example calculation of the OASPL contours around an aircraft in sea-level static and cruise conditions.

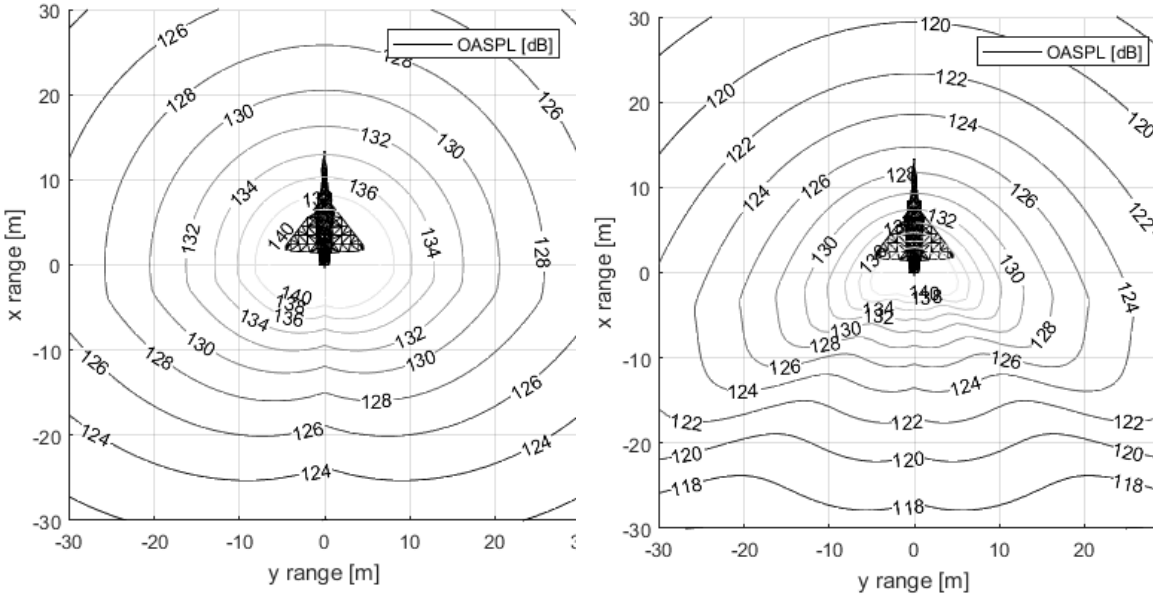

Figure 3.25: Maximum-power OASPL contours around an aircraft at static (left) and cruise (right) conditions.

3.3.2 Sonic Boom

The method of reference [145] was selected for sonic boom prediction. This is essentially a graph-based procedure that reduces the problem to the following equation:

$$\Delta P_{max} = 2K_P K_s \sqrt{p_v p_g}(M^2 - 1)^{1/8} h^{-3/4} L^{3/4} \qquad (3\text{-}18)$$

Where p_v, p_g account for atmospheric pressure at flight altitude h and at ground level respectively, M is the cruise Mach number and L is the aircraft's length. Parameters K_s (aircraft shape factor) and K_p (pressure amplification factor) are derived from Figures 3.26 and 3.27.

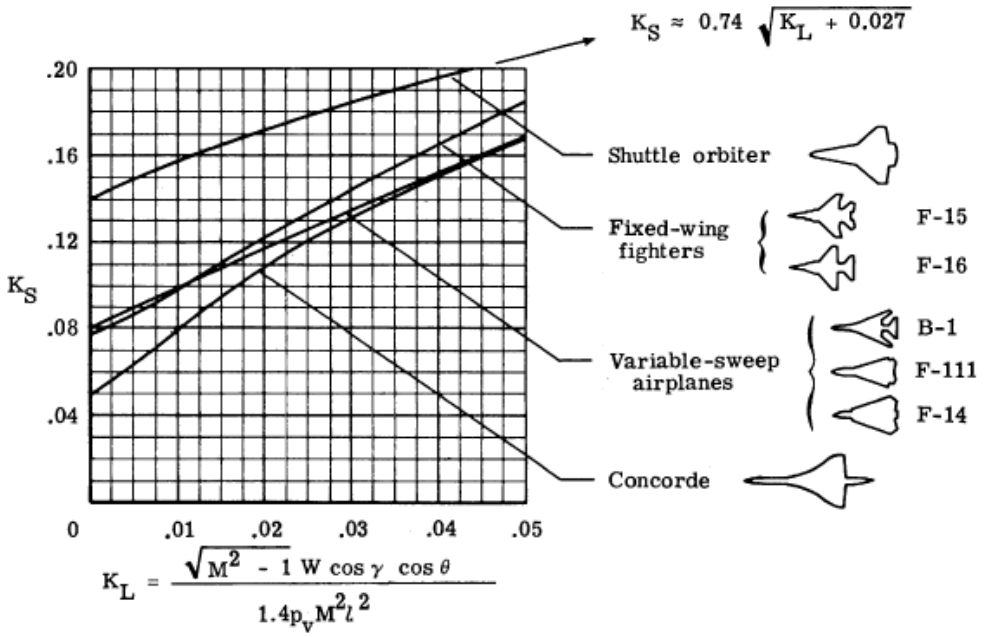

Figure 3.26: Graph for estimating shape factor K_s [145].

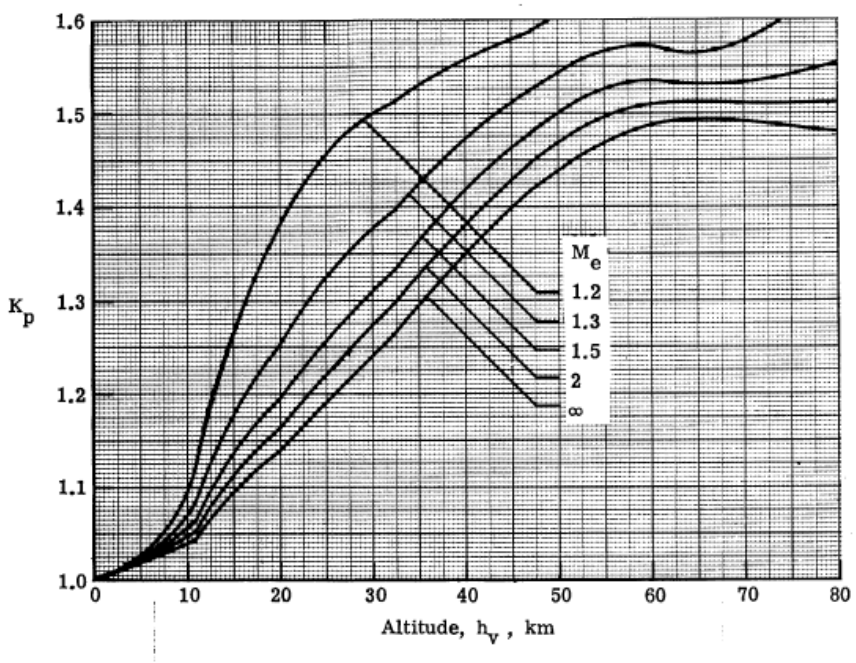

Figure 3.27: Pressure amplification factor K_p as a function of cruise altitude and Mach number [145].

The sum of the calculated sonic boom and jet noise sound pressure levels with respect to an observer on ground located directly underneath the aircraft is

used as a representation of the aircraft noise signature. Figure 3.28 shows a calculated distribution of aircraft sound pressure levels within the flight envelope of a typical fighter aircraft at cruise. The sonic boom effect can be observed as a sudden increase in noise sound pressure at Mach 1, leading to pressure values that are approximately two orders of magnitude higher than those generated by jet noise. In the same Figure, a second effect is also visible, which is the reduction of jet noise at high-subsonic cruise due to the faster mixing of the exhaust jet with the freestream flow, creating a downward 'droop' of the sound pressure contours in the speed region between Mach 0.7-1. In Figure 3.25, the same phenomenon is shown to affect the directionality of jet noise emissions and reduce noise intensity with increasing aircraft velocity.

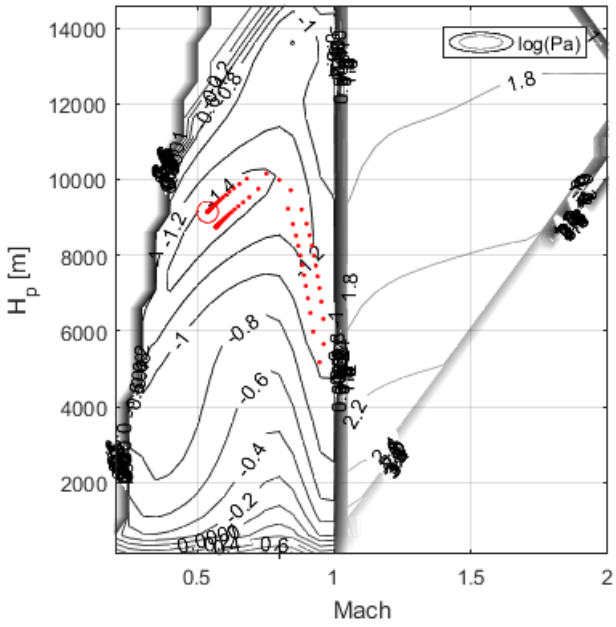

Figure 3.28: Estimated logarithmic aircraft sound pressure contours in an Altitude-Mach number chart for cruise condition. Red circle represents the minimum noise solution, whereas red dots show the corresponding search conducted by an optimization solver.

3.4 Mission Simulation

The estimation of military aircraft climb/descent performance requires the generation of optimal trajectories; contrary to civil aircraft, mission climb profiles

are not subject to strict air traffic regulations and are typically optimized to maximize aircraft mission performance. Because of its simplicity, Rutowski's [50] energy-based climb path optimization procedure is a tool that is commonly used to make this type of calculations. Although quite effective, the method has well-known limitations that limit its accuracy and applicability. An often cause of discrepancies is the method's assumption that the transition between aircraft states with the same Specific Energy (E_s) can be realized instantaneously, which is clearly not the case in real-world scenarios. To add more, aircraft dynamics are not taken into account meaning that the flyability of the calculated trajectories is not guaranteed. Finally, the method is only restricted to the calculation of fixed-throttle climb profiles which limits its applicability to the simulation of full aircraft mission scenarios.

In this project, two separate approaches where adopted with a view to tackle the limitations of the Energy-Manoeuvrability technique. The first one is a simulation-based optimization methodology that focuses on the analysis of mission climb segments. The second focuses on full-mission scenarios and is based on an augmented version of the Energy-Manoeuvrability method that allows for the concurrent optimization of aircraft mission profiles and engine control schedules. A description of both approaches is given in the following paragraphs.

3.4.1 Climb Performance Simulation

Climb performance is usually one of the most crucial factors for an aircraft's ability to fulfil its mission. A military aircraft climb profile is characterized by fast acceleration segments, steep gradient climbs and quick manoeuvres involving exchanges between kinetic and potential energy. In this context, a simulation-based optimization scheme was deemed more suitable than an energy-based approach because the former allows capturing the effects of aircraft dynamics which are prominent in this type of trajectory. This was based upon a population-based optimization scheme which permitted the use of a direct interface with the engine modelling software. A novel multi-objective formulation

to the classical aircraft climb path optimization problem is also proposed as a better means for describing the climb potential of candidate aircraft/engine configurations. The methodology is described in detail in the following paragraphs.

3.4.1.1 Aircraft Model

A 5-DOF longitudinal point-mass aircraft state-space model was created for this application (Equations 1-7), excluding lateral-directional dynamics which are irrelevant to the intended climb performance studies.

For the simulation runs, a constant throttle setting was assumed, which can be considered as standard practice in aircraft climb sequences [48]. Flight path angle control was used to control the aircraft's climb rate, and airspeed so as to fly commanded paths in the Pressure Altitude (h) - Mach Number (M) plane; the exact guidance logic employed is addressed in paragraph 3.4.1.3. Flight path angle rate saturation was implemented to the model to represent the aircraft's maximum lift capability and structural strength (Eqs. 3-22, 3-24)

$$\dot{x} = V cos\gamma \tag{3-19}$$

$$\dot{h} = V sin\gamma \tag{3-20}$$

$$\dot{V} = \frac{T-D}{m} - g sin\gamma \tag{3-21}$$

$$\dot{\gamma} = \begin{cases} \min\left\{\frac{\gamma_c-\gamma}{\tau}\ ,\ \frac{L_{max}}{mV} - \frac{gcos\gamma}{V}\right\} & \gamma_c > \gamma \\ \max\left\{\frac{\gamma_c-\gamma}{\tau}\ ,\ \frac{-L_{max}}{mV} - \frac{gcos\gamma}{V}\right\} & \gamma_c < \gamma \end{cases} \tag{3-22}$$

$$\dot{m} = -SFC \times T \tag{3-23}$$

$$L_{max} = \min\left\{\frac{1}{2}\rho S C_{L_{max}} V^2\ \ ,\ \ n_{z_{max}} mg\right\} \tag{3-24}$$

$$D = \frac{1}{2}\rho S V^2 \mathrm{C_D} \tag{3-25}$$

3.4.1.2 Generation of Climb paths

Under the assumption of a constant throttle setting, climb paths can be considered as two-dimensional curves in the H-M plane interconnecting specified start and end conditions. In the present study, the latter where represented by Bezier splines [146] which are parametric curves built around polynomial expressions, known as the Bernstein polynomials. A Bezier curve of order n is defined by a set of control points, P_0 through P_n, under the formula:

$$B(t) = \sum_{i=0}^{n} \binom{n}{i} (1-t)^{n-i} t^i P_i \qquad 0 \leq t \leq 1 \tag{3-26}$$

Where $\binom{n}{i} = \frac{n!}{i!(n-i)!}$ and P_i are the coordinates of control point i.

The selection of Bezier splines to construct flight paths is justified by a number of advantages over other curve-fitting approaches:

1. Complex curve geometries may be generated using a small number of control variables
2. Boundary conditions may be easily applied
3. Bezier splines allow for the representation of non-functional relations between Altitude and Mach number which may be generated by combinations of accelerated climbs/descents with zoom climb-type manoeuvres
4. The curves produced are directional, a feature that can be exploited by the aircraft's path-tracking guidance logic.

An example of a Bezier-spline-generated climb path is shown in Figure 3.29, plotted over contours of Specific Excess Power (P_s).

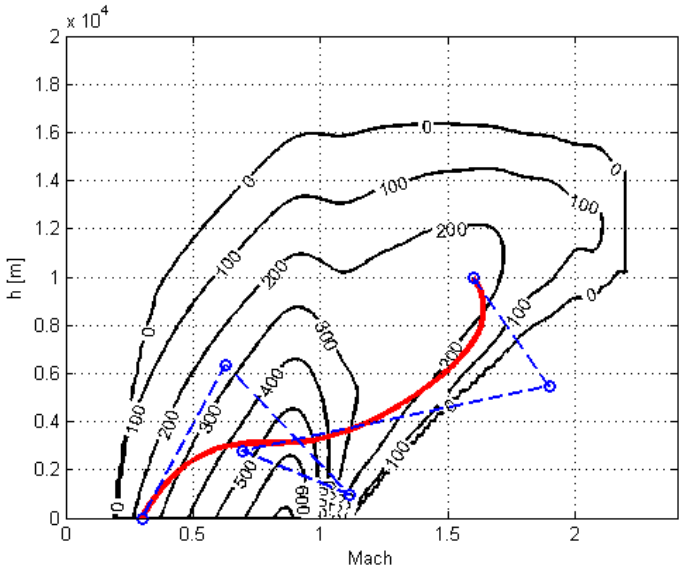

Figure 3.29: Climb path (red) generated using a Bezier spline, plotted over Specific Excess Power contours. The spline's control points are shown in blue.

Since for a climb path to be acceptable, values of altitude should be positive throughout is entire length, to reduce the amount of rejected solutions during the optimization run, the resulting negative altitude values were forced to zero.

3.4.1.3 Aircraft Guidance and Control

Assuming a constant throttle setting, the aircraft's rate of climb and airspeed may be simultaneously controlled by properly adjusting its flight path angle. From the definitions of Specific Energy (E_s) and Specific Excess Power (P_s) [49]:

$$E_s = h + \frac{V^2}{2g} \tag{3-27}$$

$$P_s = \frac{T-D}{mg}V \tag{3-28}$$

$$P_s = \frac{dE_s}{dt} = \dot{h} + \frac{V}{g}\dot{V} \tag{3-29}$$

Using the chain rule:

$$\frac{dh}{dM} = \frac{dh}{dV}\frac{dV}{dM} = \frac{dh}{dV}a = \frac{dh}{dt}\frac{dt}{dV}a = \frac{\dot{h}}{\dot{V}}a \Rightarrow \dot{V} = \frac{\dot{h}a}{\left[\frac{dh}{dM}\right]} \tag{3-30}$$

Combining Equations (3-29) and (3-30)

$$P_s = \dot{h} + \frac{V}{g}\frac{\dot{h}a}{\left[\frac{dh}{dM}\right]} \Rightarrow \dot{h} = \frac{P_s}{1+\frac{Va}{g\left[\frac{dh}{dM}\right]}} \tag{3-31}$$

Knowing that $\dot{h} = V sin\gamma$, Equation (3-31) becomes

$$\gamma = sin^{-1}\frac{P_s}{\left(1+\frac{Va}{g\left[\frac{dh}{dM}\right]}\right)V} \tag{3-32}$$

It is thus possible to fly in a desired direction in the H-M plane only by controlling the aircraft's flight path angle. Limitations, however, do exist:

For $\gamma > 0$

$$\frac{dh}{dM} < \frac{V^2 a}{g(P_s - V)} \tag{3-33}$$

The limiting value corresponds to the aircraft climbing vertically.

Equivalently, for $\gamma < 0$

$$\frac{dh}{dM} > \frac{-Va}{g(\frac{P_s}{V}+1)} \tag{3-34}$$

the limiting value corresponding to a vertical dive.

Both limitations are presented graphically in Figure 3.30, the shaded area denoting the range of physically possible transitions in the h-M plane.

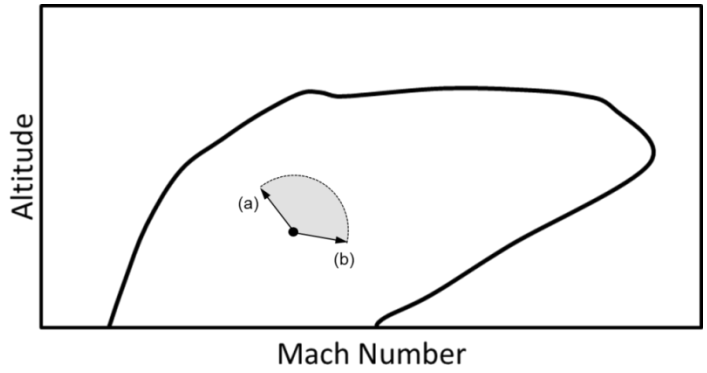

Figure 3.30: Schematic representation of feasible transitions in the h-M plane by means of flight path angle control (shaded area). Limits (a) and (b) correspond to a vertical climb and a vertical descent respectively

In order to evaluate the specified climb paths, a non-linear path-following guidance method was developed and used to guide the aircraft model in the h-M space. This was inspired by the Carrot Chasing algorithm [148], adapted to match the specific characteristics of the examined guidance problem.

From the derivation of the previous paragraph, it was shown that, subject to some limitations, it is possible to fly in a particular direction in the h-M plane by properly adjusting the aircraft's flight path angle: A transition from an initial state (0) to new state (1) can be realized by setting the flight path angle to a value such that $\frac{dh}{dM} = tan\theta$, θ being the angle formed between the states' relative position vector and the M axis (Figure 3.31). Consequently, instead of controlling the rate of rotation of the vehicle's velocity vector, as in typical guidance applications, direct control over the direction of displacement in the h-M plane is available. Based on this feature and the Carrot Chasing guidance scheme, a methodology for path-tracking in the h-M plane was developed. This is presented schematically in Figure 3.32.

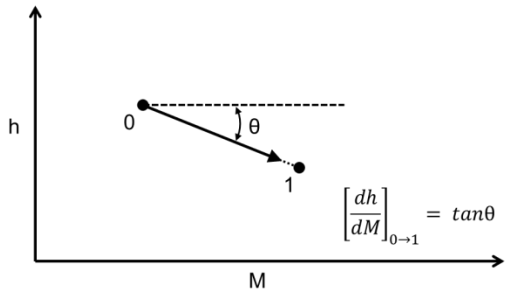

Figure 3.31: Condition to achieve a transition from state (0) to state (1) in the H-M plane

Let C represent an arbitrary curve in the h-M plane, $\overrightarrow{x_0}$ the vehicle's current position and $\overrightarrow{x_1}$ the projection of $\overrightarrow{x_0}$ on C. A reference point $\overrightarrow{x_{1'}}$ is generated on C, at a distance $d_{11'}$ downstream of $\overrightarrow{x_1}$. The direction of the vehicle's displacement vector $\overrightarrow{V'}$ is defined as:

$$\vec{V} \;//\; (\overrightarrow{x_{1'}} - \overrightarrow{x_0}) \tag{3-35}$$

Point $\overrightarrow{x_{1'}}$ is equivalent to the Virtual Target Point used in the Carrot Chasing path tracking algorithm and is generated by means of numerical integration over curve C to appear at a fixed curve length downstream of $\overrightarrow{x_0}$.

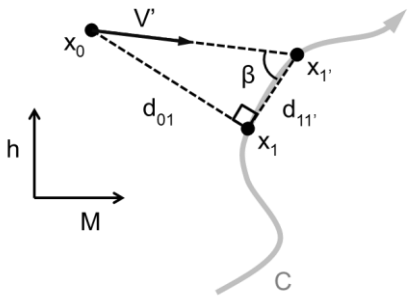

Figure 3.32: Schematic representation of the proposed path-tracking method

The path tracking methodology hereby presented was evaluated over a wide variety of flight paths, displaying very good overall performance (Figure 3.33).

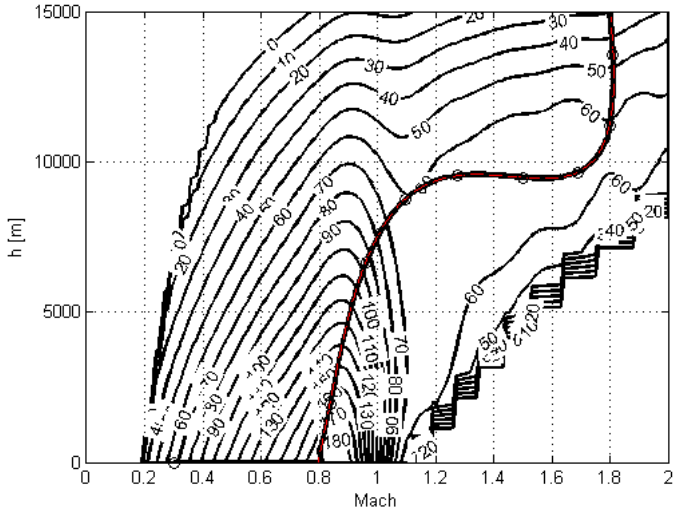

Figure 3.33: Path tracking in a supersonic climb test. The climb path is shown in red and the aircraft's trajectory in black, empty circles corresponding to aircraft position at equal time intervals. The climb path is plotted over calculated contours of Specific Excess Power, expressed in m/s.

3.4.1.4 Validation

In this Paragraph, a study of the stability characteristics of the proposed path-tracking method is conducted over a circular trajectory of radius R. Results may be generalized for any curve C by setting R equal to the local curvature of C. In order to focus on the performance of the path-tracking algorithm aircraft dynamics have been neglected; it is hereby assumed that the aircraft reproduces all commands instantaneously and without error. Figure 3.34 illustrates the system geometry for the examined case.

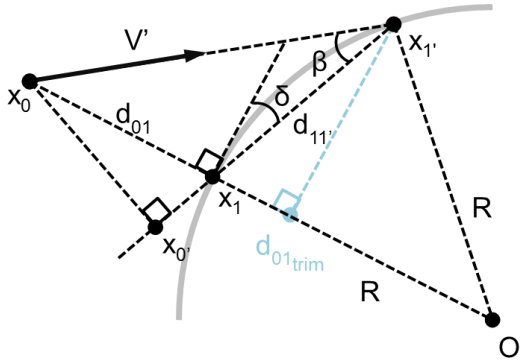

Figure 3.34: System geometry for a circular path

For a path with fixed curvature:

$$d_{11'} = const \tag{3-36}$$

Consequently,

$$\delta = const = \sin^{-1}\left(\frac{d_{11'}}{2R}\right) \tag{3-37}$$

The rate of change of the cross-track error d_{01} equals:

$$\dot{d_{01}} = -V'\sin(\beta + \delta) \tag{3-38}$$

From the triangle $(x_0 x_{0'} x_{1'})$:

$$\beta = \tan^{-1}\left(\frac{d_{01}\cos\delta}{d_{01}sin\delta + d_{11'}}\right) \tag{3-39}$$

From Equations (3-38), (3-39), knowing that $d_{11'}, \delta$ are constant:

$$\dot{d_{01}} = -V' \sin\left(\tan^{-1}\left(\frac{d_{01}\cos\delta}{d_{01}sin\delta + d_{11'}}\right) + \delta\right) = f(d_{01}) \tag{3-40}$$

which is the system's state-space model.

For equilibrium:

$$\dot{d_{01}} = 0 \overset{(19)}{\Longrightarrow} \beta = -\delta \Rightarrow tan\beta = -tan\delta \tag{3-41}$$

Combining Equations (3-37), (3-39) and (3-41) yields:

$$d_{01_{trim}} = -2Rsin^2\delta \tag{3-42}$$

which corresponds to a point inside the circle where $\overrightarrow{V'}$ becomes normal to $\overrightarrow{d_{01}}$, as shown in Figure 3.34.

Some steady-state cross-track error is thus unavoidable, given that a positive value of δ is required for path-tracking; this, however, may become negligible if angle δ is set at an adequately small value i.e. $d_{11'} \ll R$.

Angle β is bounded in the interval $\left(-\frac{\pi}{2}, +\frac{\pi}{2}\right)$, consequently, from Equations (3-37), (3-39), d_{01} is also bounded:

$$\beta \in \left(-\frac{\pi}{2}, +\frac{\pi}{2}\right) \Rightarrow \mathrm{d}_{01} \in (-2\mathrm{R}, +\infty) \tag{3-43}$$

From Equation (3-40), f is monotonous for $\mathrm{d}_{01} \in (-2\mathrm{R}, +\infty)$, as a synthesis of monotonous functions, consequently:

$$f(d_{01}) = \begin{cases} > 0 & d_{01} < d_{01_{trim}} \\ = 0 & d_{01} = d_{01_{trim}} \\ < 0 & d_{01} > d_{01_{trim}} \end{cases} \tag{3-44}$$

Let $= d_{01} - d_{01_{trim}}$, and a Lyapunov-candidate function $V(x) = |x|$. Then:

$$\dot{V}(x) = \frac{dV}{dx}\dot{f}(x) = sgn(x)\dot{d_{01}}(x) \tag{3-45}$$

Using Equation (3-44):

$$\dot{V}(x) < 0 \; \forall x \in \left(-2R - d_{01_{trim}}, +\infty\right) \setminus \{0\} \tag{3-46}$$

Therefore, $f(x)$ is *asymptotically stable* for all possible values of x.

3.4.1.5 Optimization Approach

3.4.1.5.1 Multi-Objective Particle Swarm Optimization (MOPSO)

Particle Swarm Optimization (PSO), first introduced in [152], accounts for a population-based optimization algorithm inspired by the social behaviour of animals. The baseline PSO algorithm combines simplicity with fine search capabilities: A population (swarm) of n particles is initialized at random positions

$\vec{x}$ within a search space of dimension D, assigned with random velocities $\vec{u} \in R^D$. At the end of each step of the PSO algorithm, positions of all n particles are updated, using the following set of equations:

For particle *i*, step *j* and search variable *k*:

$$v_{ijk} = a_k c_1 \left(x_{gbest_{jk}} - x_{ijk}\right) + b_k c_2 \left(x_{pbest_{ijk}} - x_{ijk}\right) + w v_{ij-1,k} \quad (3\text{-}47)$$

$$x_{ij+1k} = x_{ijk} + v_{ijk} \quad (3\text{-}48)$$

where $\vec{x}_{gbest}$ stands for the position of the global best, namely, the best-so-far solution discovered by the swarm; $\vec{x}_{pbest}$ stands for the position of the particle's personal best which represents the best-so-far solution discovered by the particle itself; c_1, c_2, w are constants (named social factor, cognitive factor and inertial weight respectively); a_k, b_k are random numbers uniformly distributed in [0, 1]; *k* = 1,…, D where D is the number of search variables.

As with most similar algorithms, a variety of multi-objective variants of PSO have been proposed expanding the method's capabilities to handle multiple objectives in a single optimization run [147]. Among these, the Multi-Objective Particle Swarm Optimization (MOPSO) introduced in [116] represents one of the most popular approaches and has been adopted for this study. The reasons for this selection was the author's experience with the method, along with its suitability for the examined application (as indicated by the literature review of Chapter 2.3.2), algorithmic simplicity and performance compared to other similar methods.

MOPSO retains the basic features of PSO, its principal difference with the latter lying in the selection of the global best: Instead of a single position in search space, the global best is chosen from an external repository containing the members of the updated Pareto front by means of a roulette wheel selection scheme weighted in accordance with the local density of the front. The procedure comprises the following steps:

1. The objective space is divided into N hypercubes and the number of non-dominated solutions contained into each hypercube is calculated.
2. Each non-empty hypercube i is assigned with a fitness values f_i inversely proportional to the number n_i of non-dominated solutions it contains, through the formula:

$$f_i = \begin{cases} 0, n_i = 0 \\ 10/n_i, n_i > 0 \end{cases} \quad (3\text{-}49)$$

3. Using fitness values f_i, a roulette wheel selection is conducted to select the hypercube from which the global best will be taken. The probability p_i of hypercube i being selected is:

$$p_i = \frac{f_i}{\sum_{j=1}^{N} f_j} \quad (3\text{-}50)$$

4. The global best position is picked at random from the solutions contained within the chosen hypercube.

3.4.1.5.2 Two-Level PSO-Based Approach to Aircraft Climb Path Optimization

Criticism over population-based optimization methods mainly focuses on the sometimes-excessive number of fitness function evaluations required for locating the optimal solutions: Although these methods are very capable of conducting a global search in the optimization domain, in applications where the computational cost per evaluation is considerable, the optimization turnaround time becomes excessive. For a pre-set number of fitness function evaluations, in some cases this results in sub-optimal, non-converged solutions. To remedy this problem, two options are generally available:

- A reduction in the number of design variables.
- The use of a surrogate model [149, 150] to better initialize the search or filter-out non-promising candidate solutions.

In this study, in order to introduce a computationally competitive climb path optimization methodology, both strategies were adopted: As specified in Section 3.4.1.2, Bezier splines were used for the generation of climb paths, reducing design variables to the coordinates of a finite number of control points, rather than solving the original highly dimensional optimal control problem; the use of a parameterized curve is a common feature with other, similar methods, however, these are hereby used to design trajectories and not control sequences, facilitating the selection of inputs. Furthermore, E-M predictions are used as a surrogate model of the actual cost functions in a proposed two-level optimization strategy. This focuses on reducing the turnaround time of the simulation-based optimization run by pre-evaluating the problem in the E-M domain: An initial low-level optimization run is performed using E-M as a low-cost, low-fidelity approximate of the actual objective functions. *TTC* and *FTC* are obtained from numerical integration of the quantities:

$$TTC = \int_{E_{s_1}}^{E_{s_2}} \frac{1}{P_s} dE_s \tag{3-51}$$

$$FTC = \int_{E_{s_1}}^{E_{s_2}} \frac{\dot{m}_f}{P_s} dE_s \tag{3-52}$$

along candidate flight paths, m_f accounting for fuel flow rate.

Solutions generated at the first level are used to initialize a second, high-level optimization run which employs the aircraft simulation to accurately assess the outcome of candidate flight paths. In both levels, the MOPSO algorithm is used to conduct the search. The flowchart of the process is shown in Figure 3.35.

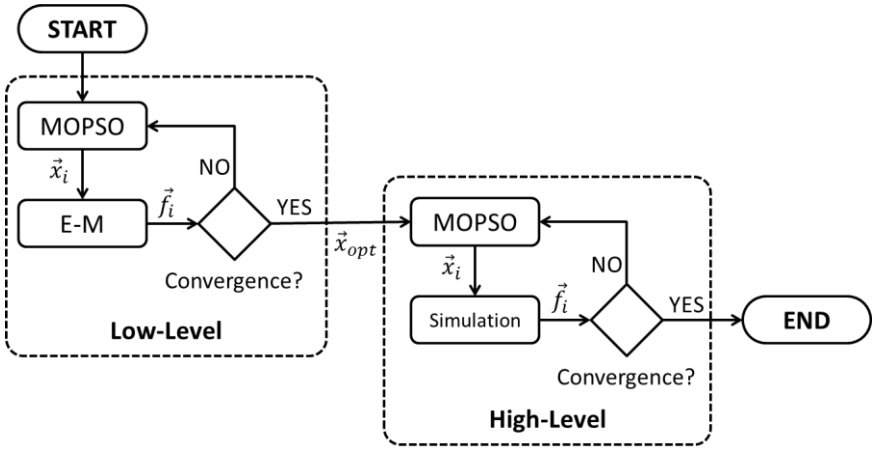

Figure 3.35. Flowchart of the proposed two-level optimization scheme.

The performance of the two-level optimization scheme was compared with that of standard MOPSO in a climb path optimization problem with 8 design variables (4 control points × 2 coordinates per point) using a population of 20 particles. After some trial and error analysis, PSO constants were set at $c_1 = c_2 = 1.7$ and $w = 0.3$. For the two-level optimization case, an initial low-level run of 300 iterations was specified. Start conditions were set at M = 0.8, h = 0 m and end conditions at M = 1.8, h = 14,000 m. The hypervolume indicator [62] was used to compare the convergence speed of the two methods. In a two-objective problem, this equals the area of the objective space formed between the origin and a user-defined “nadir” point (for this example, this was set at (800, 2500)) that is dominated by the Pareto front.

In order to address the randomness of the PSO, 10 optimization runs were performed for each method. The averaged convergence histories are shown in Figure 3.36 and the mean and standard deviation values of the final solutions are included in Table 3.5. These indicate that the proposed approach displayed consistently faster convergence over the basic MOPSO method, which is initialized using a homogeneous random distribution of the particles in the design space. As expected, the injected optimal solutions from the E-M calculations were sub-optimal when evaluated by means of the aircraft simulation; the average hypervolume of the injected front was rather low when compared to the converged solutions and was equalled by MOPSO after only a few iterations. Despite this, the large number of well-placed solutions that were

injected to the initial population did consistently boost convergence speed, leading to better fronts for a given amount of fitness function evaluations (Figure 3.37).

Table 3.5. Convergence of the proposed 2-level MOPSO vs. standard MOPSO after 100 iterations; Statistics have been derived from 10 optimization runs for each method.

Method	Hypervolume Indicator	
	Mean	Std. Dev.
$MOPSO$	5.142×10^5	3.876×10^3
$MOPSO\ 2\text{-}level$	5.234×10^5	5.825×10^3

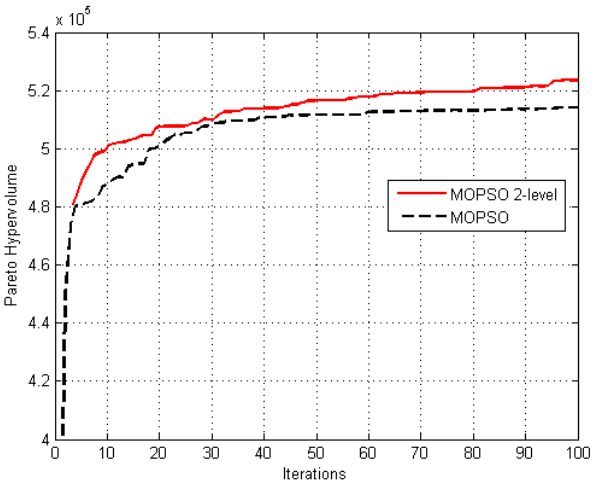

Figure 3.36. Convergence of the proposed 2-level MOPSO vs. standard MOPSO in a supersonic climb path optimization problem, using a population of 20 particles; results are averaged from 10 two-objective optimization runs. Iteration counts for the two-level method have been shifted to account for the computational cost of the low-level optimization run. The hypervolume indicator quantifies the part of the objective space (up to a user-defined "nadir" point) dominated by the Pareto front. Higher indicator values correspond to better-placed and/or better-populated fronts.

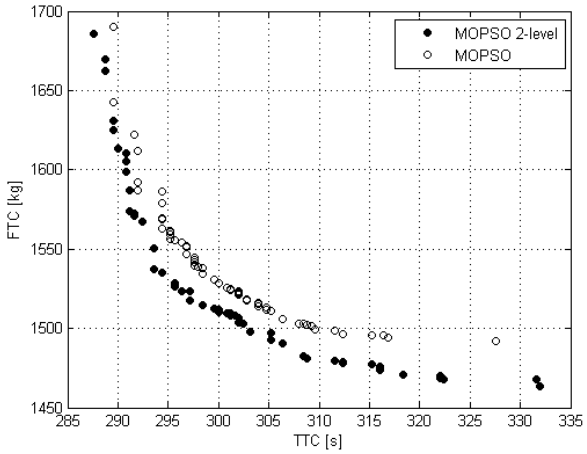

Figure 3.37. Pareto front produced by the proposed two-level MOPSO vs. standard MOPSO after 100 iterations, using a 20-particle population.

3.4.2 Mission Performance Simulation

As a result of the longer time-scales involved compared to simple climb segments, the simulation of full mission profiles is a much more demanding task, mainly due to the associated rise in computational time requirements. Taking this into account, in the context of the present project, the full-mission simulation strategy was switched to a quasi-static scheme using an augmented version of the classical Energy-Manoeuvrability method to model climb and descent segments.

Based on an analysis of the mission profiles listed in the Appendix section of MIL-STD-3013 [48] it was noted that, with only few exceptions, all the mission segments included fall into one of the following categories:

1. *Energy transitions* covering climb, descent, acceleration and deceleration segments
2. *Cruise* covering cruise, loiter, penetration and withdrawal flight phases
3. *Combat*

Under this scope, mission simulation was split into three separate routines, each corresponding to a category listed above. A description of the exact approach followed for each routine is given in the following sub-sections.

3.4.2.1 Energy Transitions

The classical Energy-Manoeuvrability method is based on a graphical procedure that is used to minimize the integral:

$$Q = \int_{E_{S_1}}^{E_{S_2}} \frac{dQ/dt}{P_S} dE_S \tag{3-53}$$

where Q is a performance metric (typically, time or fuel). Rutowski suggested that an optimal trajectory (with respect to Q) can be constructed by joining the points where contours of $\frac{P_S}{dQ/dt}$ are tangent to specific energy (E_s) contours on a Mach-Altitude chart (Figure 3.38).

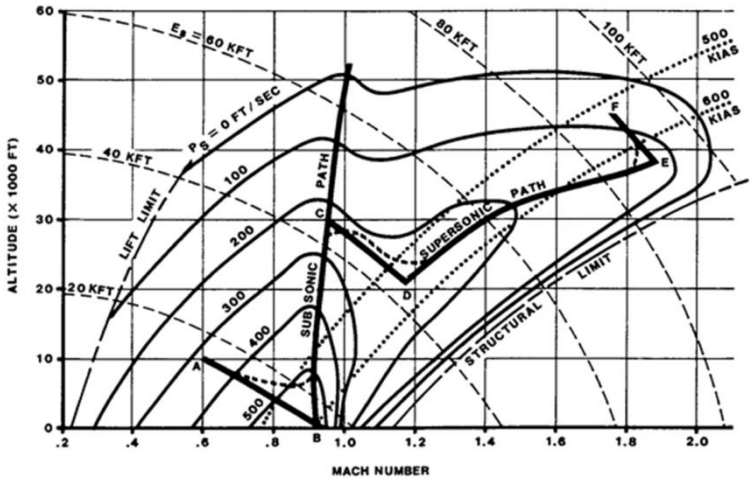

Figure 3.38: Minimum-time Rutowski climb paths for a supersonic fighter [99].

An obvious limitation of the method is that it assumes that a constant throttle setting is retained throughout the entire trajectory. This might be considered typical for aircraft climb sequences, however, as far as aircraft full mission performance studies are concerned, studying the actual potential of aircraft/engine configurations dictates that the engine schedule (fuel flows, variable geometry) be adapted to the requirements of different mission segments. Considering that the original method represents a sequential approach to solving the generalized trajectory optimization problem, it is easily understood that the latter limitation may be easily overcome if the basic

graphical solution that is restricted to only two dimensions is replaced with an optimization routine. In this context, it is also more practical to introduce a discretized version of Eq. (3-53) and formulate the respective discrete optimization problem:

$$\min_{q} Q = \sum_{i=1}^{N} \frac{1}{q_i} \Delta E_{S_i} \tag{3-54}$$

This is converted to N maximization problems that are solved independently:

$$\max_{\bar{x}} q_i = \frac{P_S}{dQ/dt}$$

subject to $$E_S(\bar{x}) = E_{S_i}$$

$$D_j(\bar{x}) \leq 0\,, \quad j = 1, \ldots, M \tag{3-55}$$

The inequality constraints $D_j(x) \leq 0$ represent the aircraft flight envelope limits. In Rutowski's two-dimensional formulation, the optimization variables included in the design vector $\bar{x}$ are the Mach number (M) and Altitude (h). If a numerical scheme is employed to solve the optimization problem instead of the baseline graphical approach, vector $\bar{x}$ may be expanded to include more variables, such as the Turbine Entry Temperature (TET), exhaust nozzle throat and exit area, along with Variable Stator Vanes' (VSV) settings; in this manner, the engine control schedule can be optimized simultaneously with the trajectory itself, providing more insight on engine performance characteristics than a fixed-throttle approach. Of course, this requires an investigation to be carried out on whether the generated solutions represent truly optimal conditions, due to the loss of the visual 'feel' as a result of the increase in dimensionality. This method was employed in the context of the present study on full-mission performance and validated through a series of test cases.

To further expand the potential of this methodology, modified versions of the optimization function q can be introduced, making it possible to construct

optimal descent/deceleration schedules covering a variety of mission tasks not included in the method's original formulation which only considers minimum time and fuel climb trajectories. In this project, an interface with the developed aircraft IRSL and noise models was used to generate minimum IRSL and noise climb paths. This was achieved in a rather straightforward manner by setting these models' outputs to represent the optimization quantity Q.

An additional limitation of the E-M profiles lies in the fact that no consideration is made for the horizontal distance covered on the course of each trajectory; as a result, in their original form, these solutions are not well-suited for aircraft range maximization. This can be achieved through a modification of the minimum fuel cost function, in order for the distance covered during the climb phase to be taken into account. This may be derived as follows: Assuming a mission segment comprising a climb followed by constant-altitude cruise with total length L, the corresponding fuel consumption Q equals:

$$Q_S = Q_{CL} + Q_{CR} \tag{3-56}$$

Where subscripts S, CL and CR correspond to segment, climb and cruise respectively. Substituting, Eq. (3-56) becomes:

$$Q_S = \int_{E_{S_1}}^{E_{S_2}} \frac{\dot{Q}_{CL}}{P_S} dEs + \left[\frac{\dot{Q}_{CR}}{V_{CR}}\right](L - x_{CL}) \tag{3-57}$$

Where x_{CL} accounts for the distance covered during the climb phase. Cruise fuel flow and velocity are assumed to be constant and set to represent maximum range cruise conditions. Expressing x_{CL} in energy terms yields:

$$Q_S = \int_{E_{S_1}}^{E_{S_2}} \frac{\dot{Q}_{CL}}{P_S} dEs + \left[\frac{\dot{Q}_{CR}}{V_{CR}}\right](L - \int_{E_{S_1}}^{E_{S_2}} \frac{V_{CL}}{P_S} dEs) \tag{3-58}$$

Reorganizing:

$$Q_S = \int_{E_{S_1}}^{E_{S_2}} \frac{\dot{Q}_{CL} - \left[\frac{\dot{Q}_{CR}}{V_{CR}}\right] V_{CL}}{P_S} dEs + \left[\frac{\dot{Q}_{CR}}{V_{CR}}\right] L \tag{3-59}$$

Considering the minimization of Q_S, the second term is a constant and can be neglected. The corresponding optimization problem formulation then becomes:

$$\min Q_S = \int_{E_{S_1}}^{E_{S_2}} \frac{\dot{Q}_{CL} - \left[\frac{\dot{Q}_{CR}}{V_{CR}}\right] V_{CL}}{P_S} dEs \tag{3-60}$$

The resulting formula corresponds to that for a minimum fuel climb path, modified with the addition of an additional term which rewards the distance covered in the horizontal plane. This objective function minimizes the fuel consumption over a mission segment of fixed length, equivalently leading to the maximization of the distance covered for a fixed fuel load.

Table 3.6: Various formulations for the energy transition optimization problem

Trajectory Type	Optimization Function	Remarks
$Minimum\ Time$	$q_i = \max_{\bar{x}} P_S$	
$Minimum\ Fuel$	$q_i = \max_{\bar{x}} \frac{P_S}{\dot{Q}_F}$	$\dot{Q}_F$: $Fuel\ Flowrate$
$Maximum\ Mission\ Range$	$q_i = \max_{\bar{x}} \frac{P_S}{\dot{Q}_F - \left[\frac{\dot{Q}}{V_x}\right]_{cr} V_x}$	$\left[\frac{\dot{Q}}{V_x}\right]_{cr}$: $Cruise\ fuel\ consumption\ per\ unit\ distance$
$Minimum\ Noise$	$q_i = \max_{\bar{x}} log\left(\frac{P_S}{P_{OASPL}}\right)$	P_{OASPL}: $Aicraft\ Noise\ Sound\ Pressure\ w.r.t.\ ground\ observer$
$Minimum\ IRSL$	$q_i = \max_{\bar{x}} \log\left(\frac{P_S}{IRSL}\right)$	$IRSL$: $Aicraft\ IR\ Signature\ Level\ w.r.t.\ ground\ observer$

Finally, the concurrent optimization of the engine schedule and the flight trajectory, allows the method's use to be extended to descent/deceleration cases; as this is a technique not documented in the literature, a numerical

experiment was conducted to assess the convergence characteristics under typical mission scenarios and is presented in Section 3.4.2.4.

A summary of various possible formulations for the energy transition optimization problem is given in Table 3.6.

3.4.2.2 Cruise

MIL-STD-310 requires that the cruise segments of the mission profiles be also optimized for maximum performance. As a result, where required, an optimization algorithm was employed to find optimal solutions for the following cruise problem:

$$\min_{\bar{x}} Q(\bar{x}) \ , \ \bar{x} = \{h, M, T\}$$

$$\text{subject to} \qquad D_j(\bar{x}) \leq 0 \ , \ j = 1, \dots, M$$

$$C(\bar{x}) = 0 \tag{3-61}$$

As previously, the inequality constraints $D_j(x) \leq 0$ represent the aircraft flight envelope limits. The additional equality constraint defines the aircraft trim condition. Depending on the formula used for function Q, different objectives can be modelled, as shown in. Figures 3.28 and 3.39 which present two example applications of the described method.

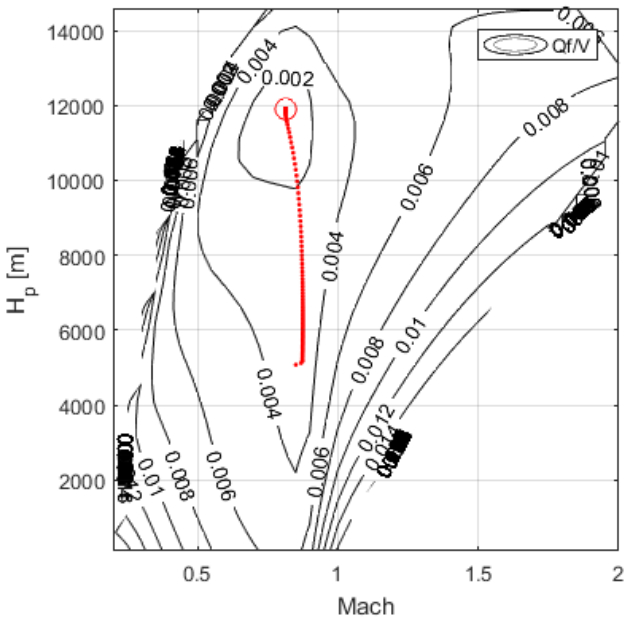

Figure 3.39: Cruise Optimization for maximum range. The red circle denotes the optimal solution whereas red dots account for intermediate solutions generated during an optimization process.

Table 3.7: Various formulations for the cruise optimization problem

Cruise Type	Q
Max Range	$Q(\bar{x}) = \frac{\dot{Q}_F}{V}$
Max Endurance (Loiter)	$Q(\bar{x}) = \dot{Q}_F$
Min Noise	$Q(\bar{x}) = \log(P_{OAPSL})$
Min IRSL	$Q(\bar{x}) = \log(IRSL)$

3.4.2.3 Combat

MIL-STD-310 prescribes combat as a sequence of turns and energy exchanges at specified flight conditions. Under this scope, sustained turn rate charts are constructed (Figure 3.40) and used to estimate the duration of each manoeuvre along with the associated fuel consumption and noise/IR generation. Case setup is the same as for the cruise case, except for the lift term which in this

case must also counteract the centrifugal force resulting from the simulated turns.

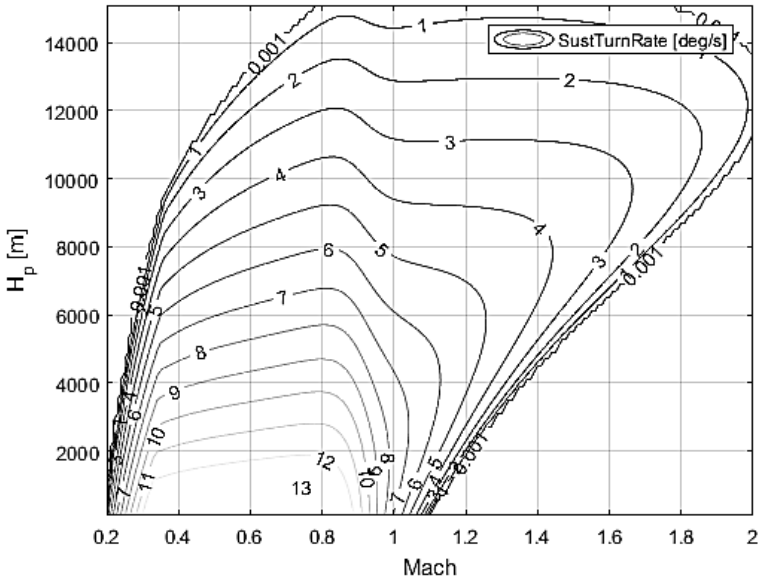

Figure 3.40: Calculated contours of aircraft sustained turn rate

3.4.2.4 Test Cases

The validity of the developed trajectory optimization methodology was assessed through a study of energy transition profiles and cruise points covering all the different optimization objectives set. Its results, presented in Figures 3.41-3.56, were also used to unveil the connections between the engine's schedule and each objective. In this context, an evaluation of different gradient-based optimization solvers was performed in order to identify the most suitable method for the specified application. Following experimentation with various solvers, a first-order variable-step method was deemed as the best choice for a direct interface with the engine modelling software, to keep intermediate solutions within the models' feasible space without significantly compromising convergence speed.

Figures 3.41-3.42 show generated optimal engine schedules for a test case considering cruise at 2000 m Altitude and Mach 0.7 for a low-bypass

afterburning turbofan engine. Figure 3.41 presents total pressure and temperature distributions along engine stations (the numbering of Figure 3.5 was used) for three different optimization objectives, namely maximum range, minimum noise and minimum IR cruise. The resulting curves signify the different ‘methods’ for adapting the engine’s operating conditions to each objective: As expected, the maximum range case achieves the minimum fuel flow value (0.348 kg/s, as compared to 0.360 and 0.544 for the minimum noise and IR cases respectively), using an ideally expanded, convergent-divergent nozzle setting (Figure 3.42).

Of great interest are the ways the engine schedule is altered to achieve the minimum noise and IR solutions. A perhaps counterintuitive finding was the fact that the highest TET value was observed in the minimum IR scenario: this solution also uses the largest throat area setting in order to maximize the engine air mass flow, therefore, in this context, a high TET (maximum allowable for the specified engine model) serves to increase the bypass ratio by allowing the fan to be driven with minimum flow passing through the engine core. These effects can be observed in Figure 3.41 through the large temperature drop in the Low-Pressure Turbine (Stations 6-7) and Mixer (Stations 7-8). An overexpanded convergent-divergent nozzle setting (Figures 3.41-3.42) is also employed to further reduce the engine’s exhaust temperature and, consequently, minimize the engine’s IR signature. However, since the fan is operating away from its design point, its isentropic efficiency is low, resulting in the highest fuel consumption among the three cases examined.

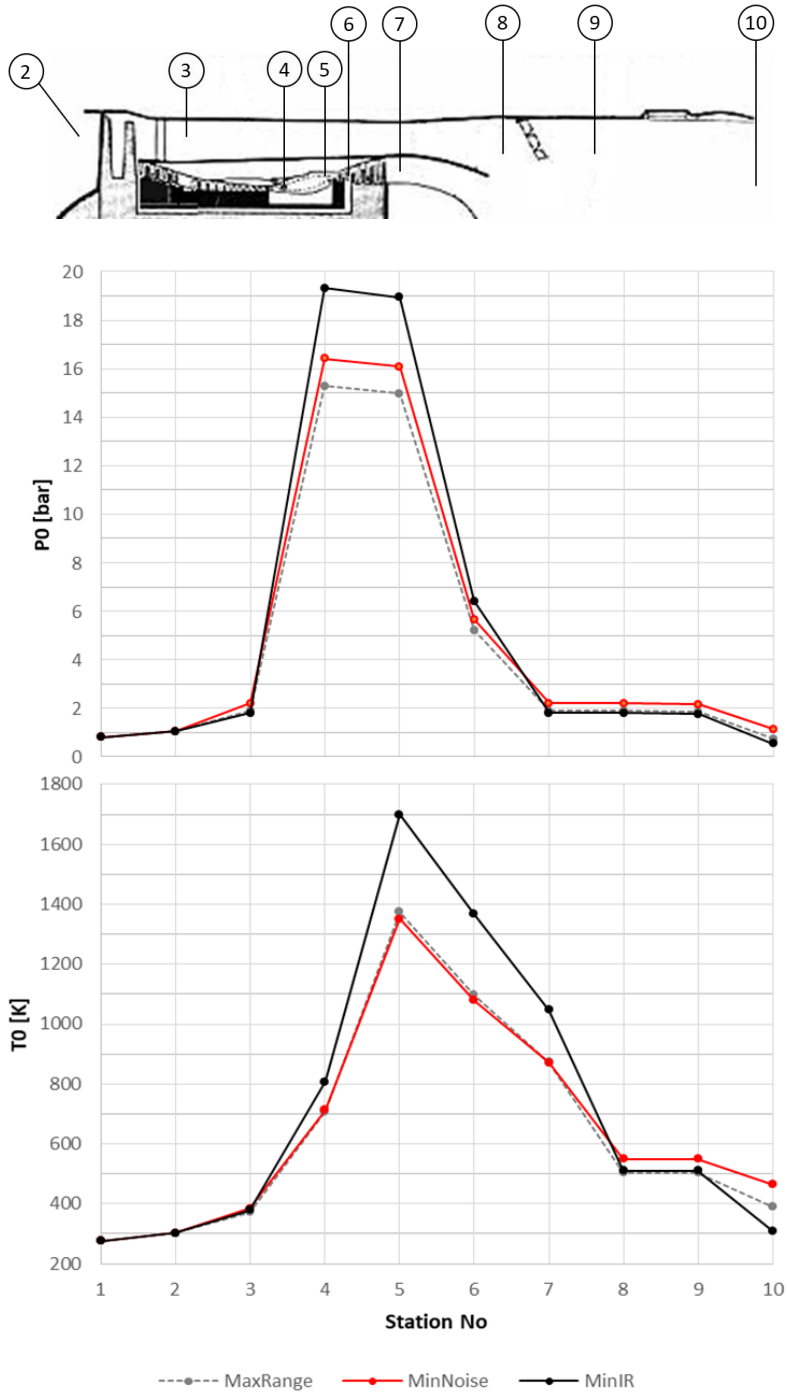

Figure 3.41. Core flow Total Pressure and Temperature distribution along engine stations for maximum range, minimum noise and minimum IR cruise solutions

Diametrically opposed to the minimum IR case, the minimum noise solution employs a low-throat-area convergent nozzle setting, aiming at minimizing exhaust velocity and generating pressure thrust through an underexpanded

nozzle. The low throat area serves in raising the fan's operating pressure ratio, and, consequently, the nozzle pressure ratio; it also results in a reduction to the engine air mass flow and bypass ratio. Compared to the maximum range case, exhaust velocity (V_j^8) is reduced by 15%, leading to a 70% decrease in engine noise sound pressure.

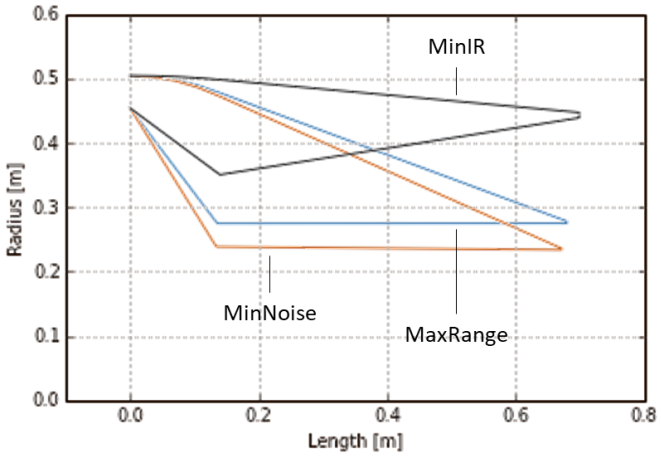

Figure 3.42. Nozzle geometry for maximum range, minimum noise and minimum IR cruise solutions

In addition to the previously examined cruise case, the developed method's performance was assessed in a trajectory optimization problem considering a climb from Altitude 300 m, Mach 0.5 to Altitude 11000 m, Mach 0.8. Five different trajectories were generated, corresponding to minimum time, noise, IR and fuel solutions, along with the proposed maximum range formulation. Figures 3.43-3.50 present the results obtained.

An inspection of the Altitude/Mach profiles of Figure 3.43 unveils the main characteristics of each trajectory: Minimum time and fuel profiles have a similar form to E-M solutions, both including an initial acceleration segment at zero altitude. In the case of the minimum time profile, this is followed by a roughly constant Mach number climb just below the drag divergence limit, whereas in the minimum time case, the climb begins earlier and follows the loci of the aircraft's maximum aerodynamic performance points. Not surprisingly, the

maximum mission range profile has a similar form to the minimum fuel solution, with some small alterations due to the different form of the optimization function used in each case. The minimum IR profile prioritizes altitude over velocity gain, in order to quickly increase the distance between the aircraft and the ground (with respect to which IR emission is measured). The same partly applies to the minimum noise solution, in this case, however, the trajectory is shifted towards higher Mach numbers. This fact is in agreement with the findings of Section 3.3 and suggests that the noise reduction effect of the jetflow mixing with the freestream at higher velocities is equally or more significant than the distance between the source and receiver.

The different characteristics of each trajectory are also visible in the Altitude-Range chart of Figure 3.44. The minimum time profile comprises a short acceleration at sea level followed by a steep 45-degree climb towards the target altitude; the distance covered in this case is significantly less than any other profile examined. TET and A/B temperature are set to their maximum values throughout the trajectory (Figure 3.45), the same also applying to nozzle throat area, which has the highest value among all trajectory types to accommodate the increase in corrected mass flow resulting from the use of afterburning (Figure 3.46). A convergent-divergent nozzle configuration is used, to maximize the velocity of the exhaust gases; the nozzle throat-to-exit area ratio decreases with altitude, to account for the increase in nozzle pressure ratio that occurs at higher altitude and Mach number (Figure 3.47).

Aside from the minimum time climb solution, the minimum IR trajectory also showcases a steep climb gradient, as expected due to the form of the trajectory in the Alt-Mach plane. The solution employs the maximum TET setting throughout the entire length of the trajectory (Figure 3.45), without use of the afterburner. A low throat-to-exit nozzle area ratio setting allows for maximizing the expansion of the engine exhaust, to reduce exit temperature (Figure 3.47) in accordance with the results from the cruise test cases. During the entire course of the minimum IR trajectory, the generated IR signal is lower than that of the other trajectory types (Figure 3.49).

On the contrary, the minimum noise profile favours horizontal acceleration to increase forward velocity, leading to the shallowest climb gradient of all five solutions examined. In common with the previous profiles, the maximum TET setting is retained throughout the trajectory (Figure 3.45). The nozzle schedule follows the same logic as for the minimum noise cruise case: the combination of a small throat area with a convergent nozzle configuration is used to raise the pressure of the exhaust jet and generate pressure thrust, allowing for a reduction in exit velocity for the same thrust level (Figures 3.46-3.47), ultimately resulting in the lowest sound pressure levels between all the trajectory types evaluated (Figure 3.50).

Minimum fuel and maximum range trajectories are similar at low altitudes, however, as the climb target is approached, the maximum range profile switches to a shallow cruise/climb segment which significantly increases the length of the trajectory (Figure 3.44). This effect is achieved by progressively reducing the TET (A/B is not used) by 100 K as compared to the minimum fuel profile's constant 1700 K setting (Figure 3.45). As a result, the length and time duration of the trajectory are enlarged, simultaneously maximizing the corresponding 'cruise' efficiency, as shown in Figure 3.48.

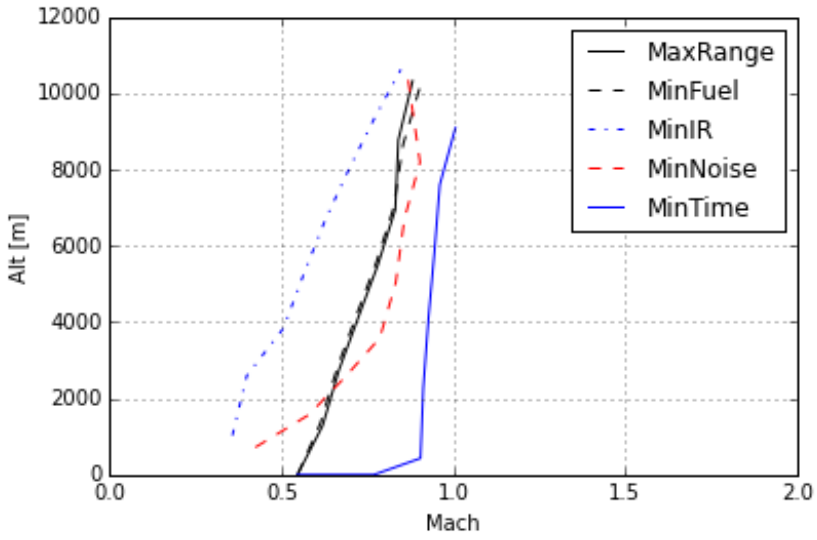

Figure 3.43. Altitude vs Mach number for maximum range, minimum noise and minimum IR climb trajectories

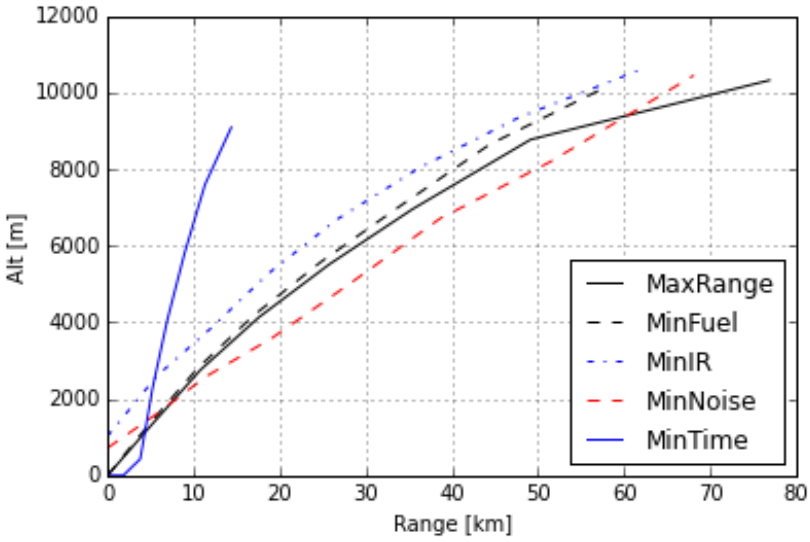

Figure 3.44. Horizontal distance vs Altitude for maximum range, minimum noise and minimum IR climb trajectories

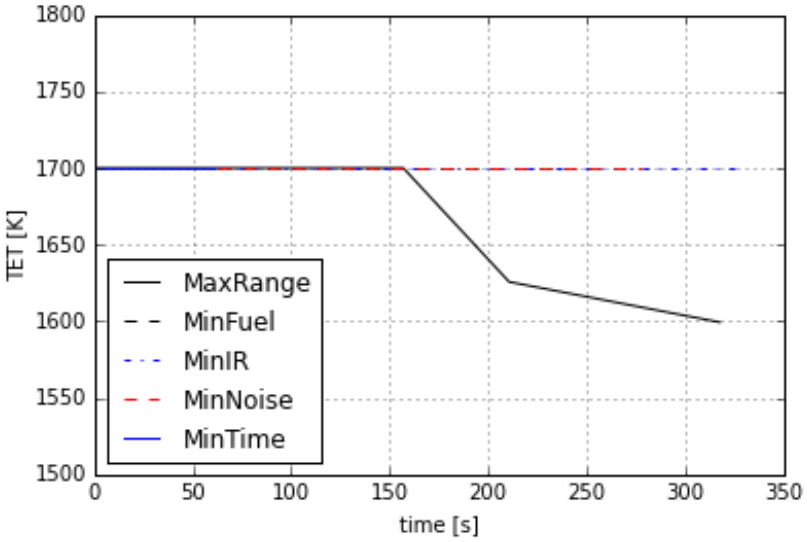

Figure 3.45. TET vs time for maximum range, minimum noise and minimum IR climb trajectories

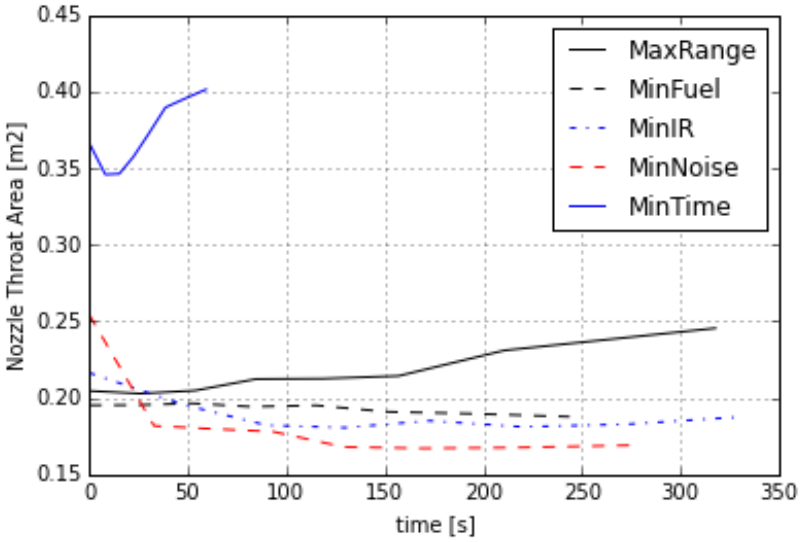

Figure 3.46. Nozzle throat area vs time for maximum range, minimum noise and minimum IR climb trajectories

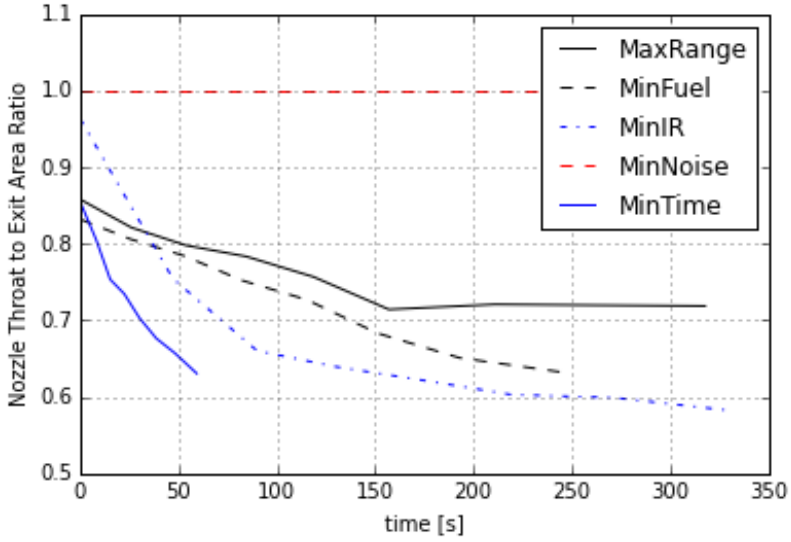

Figure 3.47. Nozzle throat-to-exit area ratio for maximum range, minimum noise and minimum IR climb trajectories

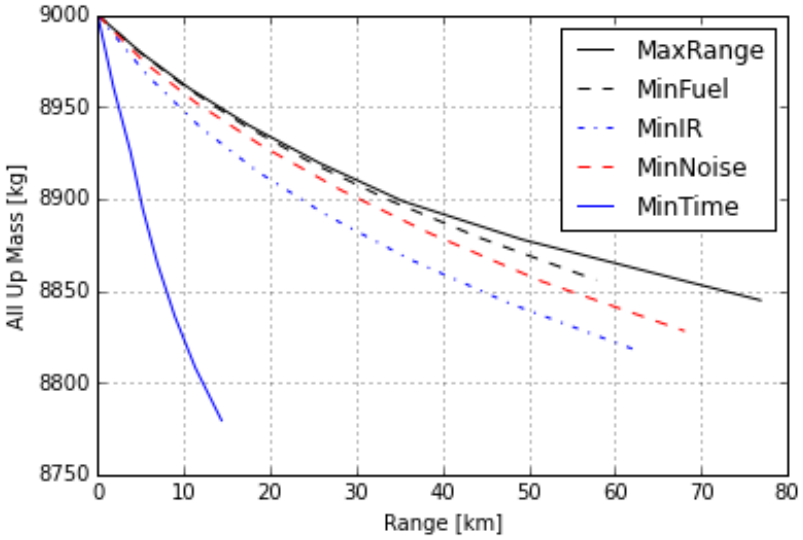

Figure 3.48. All up mass vs horizontal distance for maximum range, minimum noise and minimum IR climb trajectories

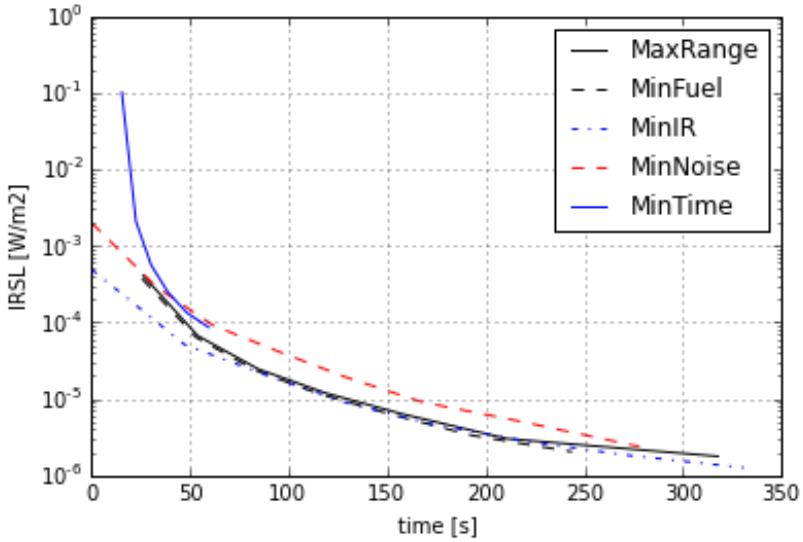

Figure 3.49. IRSL vs time for maximum range, minimum noise and minimum IR climb trajectories

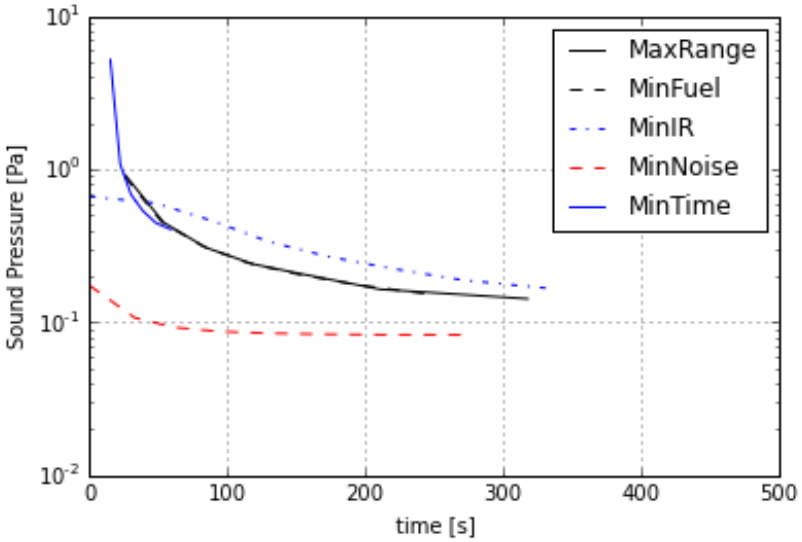

Figure 3.50. Noise sound pressure vs time for maximum range, minimum noise and minimum IR climb trajectories

Having explored the different characteristics of the above described profiles, the possibility of applying the same approach to descent profiles was evaluated. This is allowed by the fact that Rutowski's energy formulation has two minima, one corresponding to the climb case (positive Ps, positive dEs) and one to the descent case (negative Ps, negative dEs). Under this scope, a test case considering a maximum range descent from Altitude 11000 m, Mach 0.8 to Altitude 100 m, Mach 0.5 was specified. In the context of the latter, the exact same case setup as for the corresponding climb case was employed, only differing in terms of the optimization solver initialization: Instead of the 'maximum dry' setup used in the climb cases, the solver was initialized at 'flight idle' conditions, to ensure that aircraft specific excess power has a negative sign.

The resulting trajectory is pictured in Figures 3.51-3.52. In accordance with standard practice in aircraft long-range descents and subject to some engine-performance-related fluctuations, the trajectory traces the loci of the maximum aerodynamic efficiency points as it sweeps through the aircraft envelope (Figure 3.51). This results in an approximately straight descent profile (Figure 3.52), with a slope of 12 (meters travelled per meter descent), higher than the airframe's maximum lift-to-drag ratio of seven, due to the non-zero thrust

contribution of the engine at idle. TET is set close to its minimum value for the entire length of the trajectory (Figure 3.53), whereas nozzle throat area is adapted to the altitude change (Figure 3.54) in a similar manner as for the climb cases (Figure 3.46). Due to the low value of the engine pressure ratio, a convergent nozzle configuration is retained throughout the entire trajectory (Figure 3.55); VSV deflection is introduced at the lower-speed segments of the trajectory to optimize the engine's off design performance (Figure 3.56).

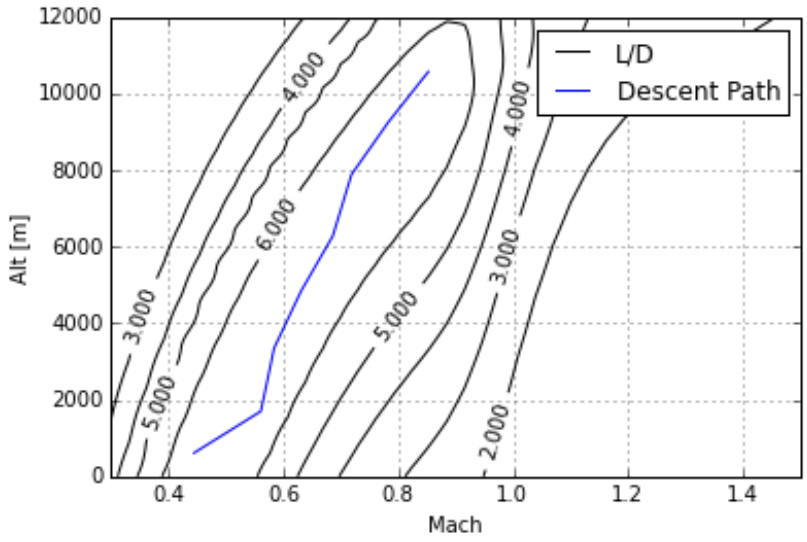

Figure 3.51. Altitude vs Mach number for the maximum range descent profile

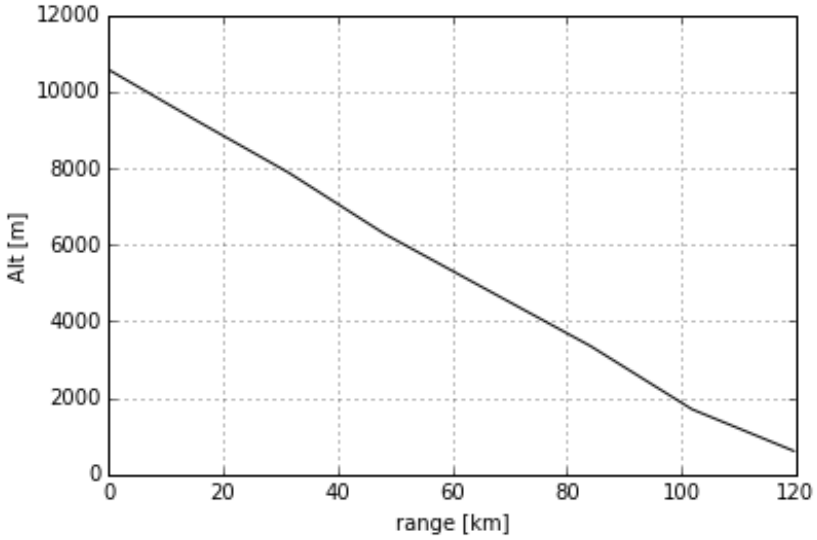

Figure 3.52. Altitude vs horizontal distance for the maximum range descent profile

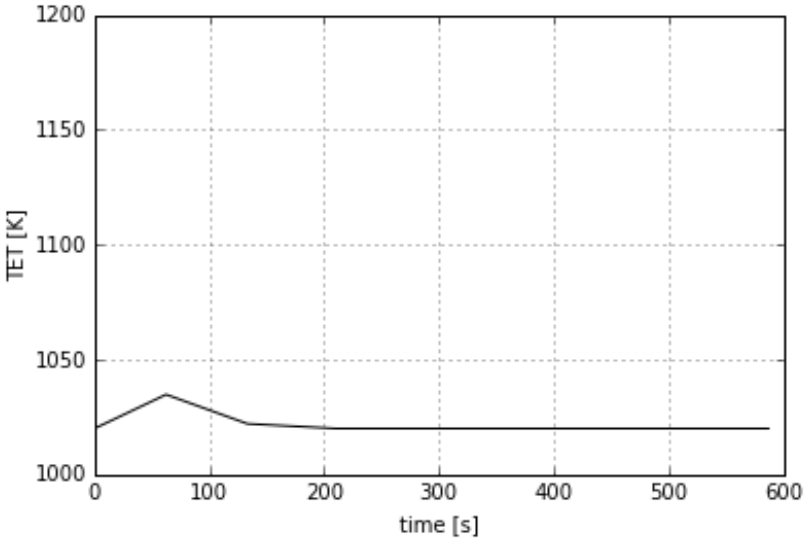

Figure 3.53. TET vs time for the maximum range descent profile

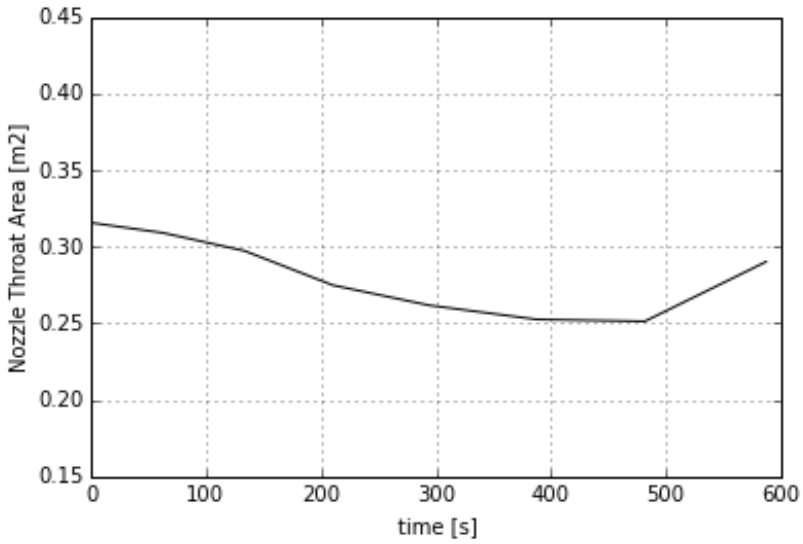

Figure 3.54. Nozzle throat area vs time for the maximum range descent profile

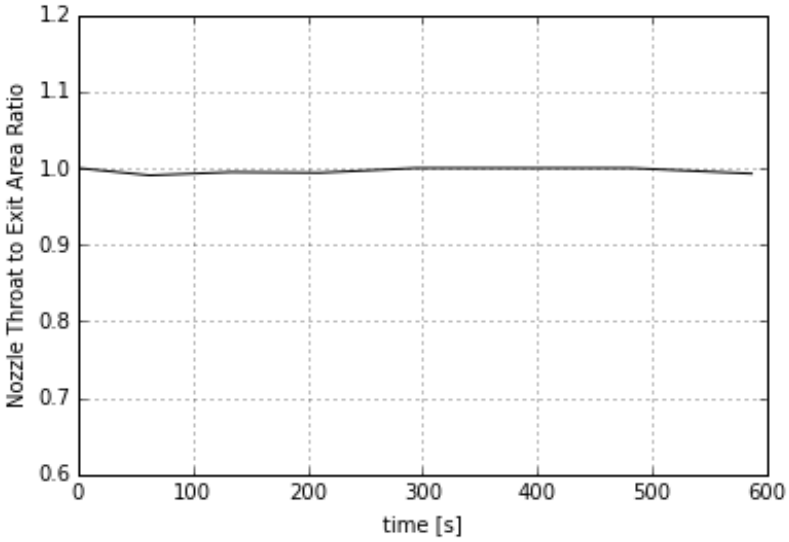

Figure 3.55. Nozzle throat-to-exit area ratio vs time for the maximum range descent profile

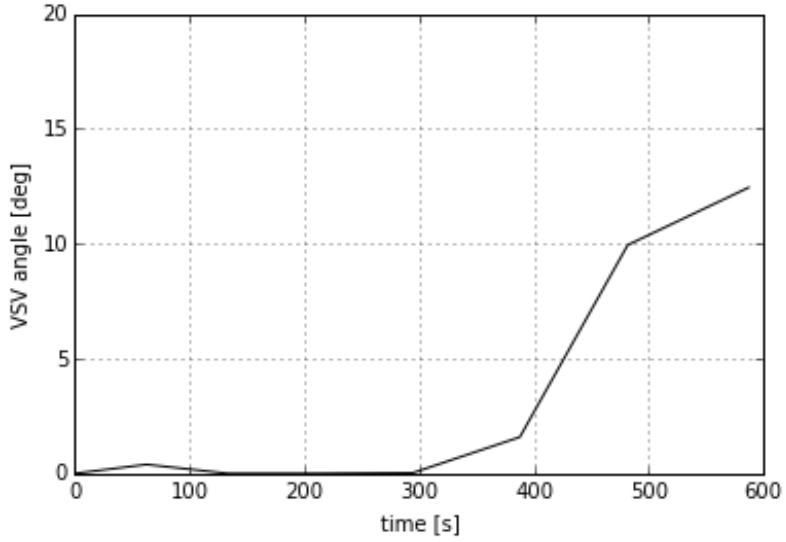

Figure 3.56. VSV angle vs time for the maximum range descent profile

3.5 Survivability

Ball [151] defines aircraft combat survivability as the capability of an aircraft to avoid or withstand a man-made hostile environment. With this in mind, the relation between aircraft combat survivability becomes evident: An aircraft must survive the challenges of the aerial battlefield in order to fulfil its mission

objectives whether these are directly related to air combat or not. Aircraft survivability is a function of many diverse variables and, consequently, hard to predict. In this study, a method for investigating the influence of the propulsion system on aircraft survivability was developed considering the major physical mechanisms of this interaction, namely the kinematic effect of engine thrust and the IR emissions generated by the engine's operation. This is achieved by combining the output of the IR model of Section 3.2 with missile-vs-aircraft and aircraft-vs-aircraft simulations to identify the spatial domain that an aircraft is vulnerable to attacks from other aircraft or missiles. A description of the simulations' setup, along with the respective aircraft and missile guidance laws is given in the following paragraphs.

3.5.1 Aircraft and Missile Dynamic Models

An 8-state aircraft model was employed to construct a representation of aircraft kinematics, assuming a no-sideslip condition. The model's equations are as follows:

$$\dot{V} = \frac{Tcosa - \dot{D}}{m} - gsin\gamma \tag{3-62}$$

$$\dot{\gamma} = \frac{(L+Tsina)cos\varphi}{mV} - \frac{gcos\gamma}{V} \tag{3-63}$$

$$\dot{\psi} = \frac{(L+Tsina)sin\varphi}{mVcos\gamma} \tag{3-64}$$

$$\dot{p} = c_1 p + c_2 \xi \tag{3-65}$$

$$\dot{\varphi} = p \tag{3-66}$$

$$\dot{\alpha} = \frac{a_c - a}{\tau_\alpha} \tag{3-67}$$

$$\dot{x} = Vcos\gamma cos\psi \tag{3-68}$$

$$\dot{y} = Vcos\gamma sin\psi \tag{3-69}$$

$$\dot{h} = V sin\gamma \tag{3-70}$$

$$L = 1/2\rho V^2 S C_{L_a} a \tag{3-71}$$

$$D = 1/2\rho V^2 S C_{\mathrm{D}} \tag{3-72}$$

$$\xi = k_p(\varphi_c - \varphi) + k_d p \tag{3-73}$$

Angle-of-attack (a), Lift (L) and roll rate $(\dot{\varphi})$ being subject to the following constraints:

$$|a| \leq a_{max} \tag{3-74}$$

$$|L| = \min\left\{\frac{1}{2\rho V^2 S C_{L_a}|a|},\ mn_{z_{max}} g\right\} \tag{3-75}$$

$$|p| \leq p_{max}(a) \tag{3-76}$$

$$|\xi| \leq \xi_{max} \tag{3-77}$$

Equations (3.74)-(3.77) represent the aircraft's maximum angle of attack capability, structural strength, roll rate limit and maximum aileron deflection respectively. Table 3.8 contains the parameter values used to create a model of a generic single-engine fighter aircraft.

Table 3.8: Aircraft Parameters

Parameter		Value	Description
m	=	$8500\ kg$	Mass
S	=	$25\ m^2$	Wing Reference Area
C_{L_a}	=	$0.07/deg$	Lift Coefficient Slope
a_{max}	=	$15\ deg$	Maximum Angle of Attack (AoA)
$n_{z_{max}}$	=	$9\ g$	Maximum Vertical Load Factor
τ_α	=	$0.1\ s$	AoA Time Constant
P_{max}	=	$270\ deg/s\ \ (zero-lift)$	Maximum Roll Rate
	=	$120\ deg/s\ \ (max\ AoA)$	
ξ_{max}	=	$20\ deg$	Maximum Aileron Deflection
c_1	=	$-2.5/s$	Roll Parameters
c_2	=	$0.76\ rad/deg.s^2$	Roll Parameter
k_p	=	20	Aileron Control Proportional Gain
k_d	=	4	Aileron Control Derivative Gain

A simpler, point-mass representation was employed to model the missile's dynamics, as per Equations (3-78)-(3-88).

$$\dot{V}_m = \frac{T_m - \dot{D_m}}{m_m} - gsin\gamma_m \tag{3-78}$$

$$\dot{a_p} = \frac{a_{p_c} - a_p}{\tau_{\alpha_m}} \tag{3-79}$$

$$\dot{a_y} = \frac{a_{y_c} - a_y}{\tau_{\alpha_m}} \tag{3-80}$$

$$\dot{\gamma}_m = \frac{a_p - gcos\gamma_m}{V_m} \tag{3-81}$$

$$\dot{\psi}_m = \frac{a_p}{V_m cos\gamma_m} \tag{3-82}$$

$$\dot{x}_m = V_m cos\gamma_m cos\psi_m \tag{3-83}$$

$$\dot{y}_m = V_m cos\gamma_m sin\psi_m \tag{3-84}$$

$$\dot{h}_m = V_m sin\gamma_m \tag{3-85}$$

$$C_{L_m} = C_{\mathrm{L_{a_m}}} a_m \tag{3-86}$$

$$a_{p,y} = \frac{\rho V^2 S C_{L_{m_{p,y}}}}{2m_m} \tag{3-87}$$

$$D_m = 1/2\rho V^2 S_m (C_{\mathrm{D_{0_m}}} + k_m C_{L_m}^2) \tag{3-88}$$

Similar to the aircraft case, the missile model is subject to aerodynamic and structural constraints:

$$|a_m| \leq a_{\max_m} \tag{3-89}$$

$$\left|a_{p,y}\right| = \min\left\{\frac{\rho V^2 S C_{L_a} |a_m|}{2m_m},\ n_{z_{max}} g\right\} \tag{3-90}$$

The model's parametrization is shown in Table 3.9: the data, sourced from reference [108], correspond to a generic short-range IR-guided missile.

Table 3.9: Missile model parameters

Parameter		Value	Description
m_m	=	$90\ kg$	Missile Mass
S_m	=	$0.03\ m^2$	Missile Reference Area
$C_{L_{a_m}}$	=	$0.61/deg$	Missile Lift Coefficient Slope
Cd_{0_m}	=	$0.75\ (subsonic)$	Missile Zero-lift Drag Coefficient
	=	$1.1\ (supersonic)$	
k_m	=	0.03	Missile Induced Drag Factor
a_{max_m}	=	$30\ deg$	Missile Maximum AoA
τ_{α_m}	=	$0.2\ s$	Missile Acceleration Time Constant
T_m	=	$15{,}000\ N$	Missile Thrust
t_B	=	$5\ s$	Propellant Burnout Time
m_p	=	$20\ kg$	Propellant Mass
$n_{z_{\max_m}}$	=	$30\ g$	Missile Maximum Vertical Load Factor

3.5.2 Engagement Scenarios

In the context of the present study on aircraft survivability, two separate simulation scenarios were examined, considering missile-vs-aircraft and aircraft-vs-aircraft scenarios. Details on the setup of each scenario are given in the following paragraphs.

3.5.2.1 Missile-vs-Aircraft scenario

A missile-vs-aircraft simulation was used to study the effect of missile and aircraft dynamics on the missile lethal envelope expressed by constructing target-centered Kinematic Lethal Zones (KLZ), as per Figure 3.57. In each simulation scenario, the missile was initialized at a distance R from the aircraft, at the same altitude and airspeed with its nose pointed to the target or offset by some fixed angle (Angle Off-Boresight - AOB) and guided to the target using proportional navigation. The target used the anti-proportional navigation scheme of reference [108] to evade capture. The latter is summarized as follows:

The normal acceleration command generated by pure proportional navigation guidance is given by the formula:

$$a_{y_c} = N_c \omega_y V_c \tag{3-91}$$

$$a_{p_c} = N_c \omega_p V_c + g cos\gamma \tag{3-92}$$

where N_c is the navigation constant, V_c is the closure velocity and ω_p, ω_y correspond to the pitch and yaw components of the Line-Of-Sight (LOS) rate vector. Imado [108] established a guidance law for missile evasion by reversing the sign of the ω components and rotating by an arbitrary angle η. The resulting guidance formula then becomes:

$$a'_{y_c} = -a_{p_c} \sin\eta + \alpha_{y_c} \cos\eta \tag{3-93}$$

$$a'_{p_c} = a_{p_c} \cos\eta + \alpha_{y_c} \sin\eta \tag{3-94}$$

By varying angle η, Imado was able to demonstrate various established, 'textbook' aircraft evasive manoeuvres while conducting large-scale simulations in the parameter space. In the present study, an optimization solver was used instead of a brute-force search to find optimal values for the navigation constant N_c and angle η that maximize time-to-intercept t_i. The latter equals the time required for the missile to approach the target at a distance R equal to the warhead's lethal radius R_w.

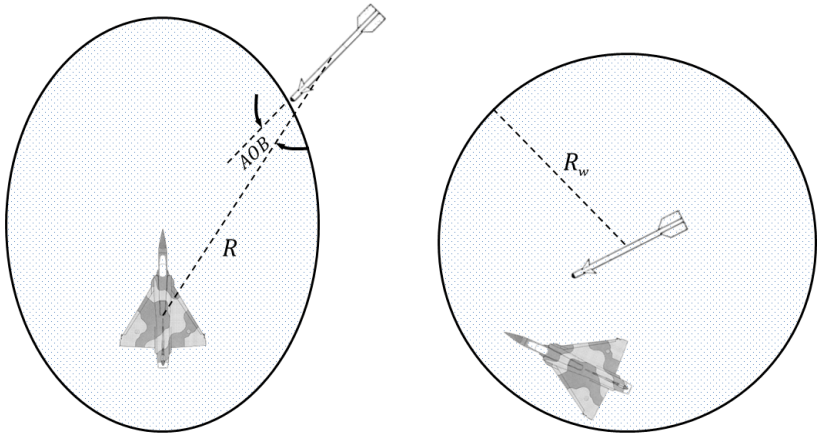

Figure 3.57: Simulation initialization [left] and intercept condition [right]. The shaded eclipse on the left corresponds to the missile's target-centered kinematic launch success zone.

Given the above description, the respective optimization problem can be formally expressed as:

$$\max\{t_i : R(t_i) = R_w\}$$

$$s.t.\ initial\ conditions\ \&\ Eq.\ (3\text{-}62)\text{-}(3\text{-}90) \qquad (3\text{-}95)$$

To ensure the global optimality of the generated solutions, given the small dimensionality and unknown structure of the problem, instead of a gradient-based optimization method, Particle Swarm Optimization (PSO - the single-objective variant of the method described in Section 3.4.1) [152] was selected as the optimization solver; population size was set to five particles, leading to

converged solutions after 10 generations on average (Figure 3.58). The result of a typical missile-vs-aircraft scenario is shown in Figure 3.59.

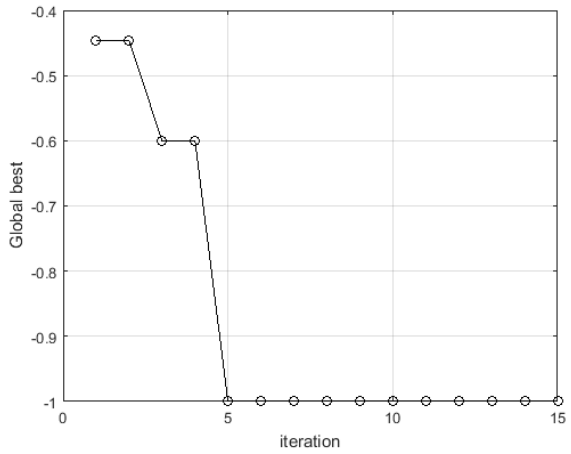

Figure 3.58: Convergence of the PSO optimization scheme for N_c and η.

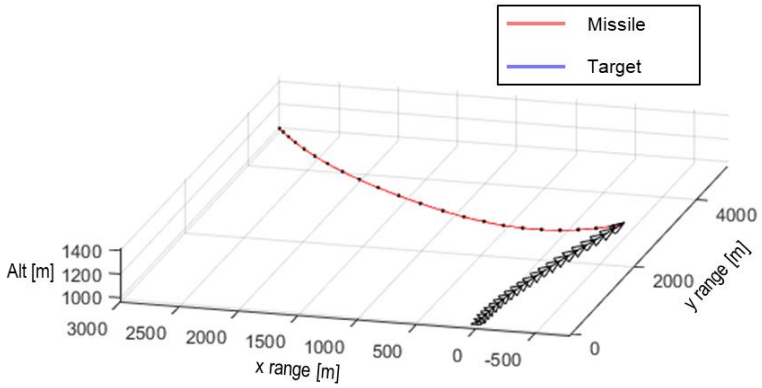

Figure 3.59: Schematic representation of a typical missile-vs-aircraft simulation scenario; the missile [red] intercepts the aircraft [blue] which attempts an 'away'-type manoeuvre

3.5.2.2 Aircraft-vs-Aircraft Scenario

The case setup for the aircraft-vs-aircraft scenario was identical to that of the missile-vs-aircraft case with two exceptions:

- The attacking aircraft's guidance was switched to a pure pursuit scheme. This was shown to be more effective in cases with low closure velocity than the proportional navigation law and more representative of human pilot behavior.

- The termination criterion was not based on the Euclidean distance between the attacker and the evader; instead, the results of multiple runs of the missile-vs-aircraft scenario where used to construct generalized weapon Lethal Zones (LZ), as functions of range, aspect angle and angle-off tail. A "kill" was counted in cases when the evading aircraft remained within the attacker's weapon envelope for time greater than one second (Figure 3.60).

- Maximum simulation time was set to 40 sec assuming that, given that both aircraft must use the maximum power throttle setting to maximize their manoeuvrability, the latter constitutes a limit above which the required fuel consumption would typically deter the attacker from performing an attack to the target.

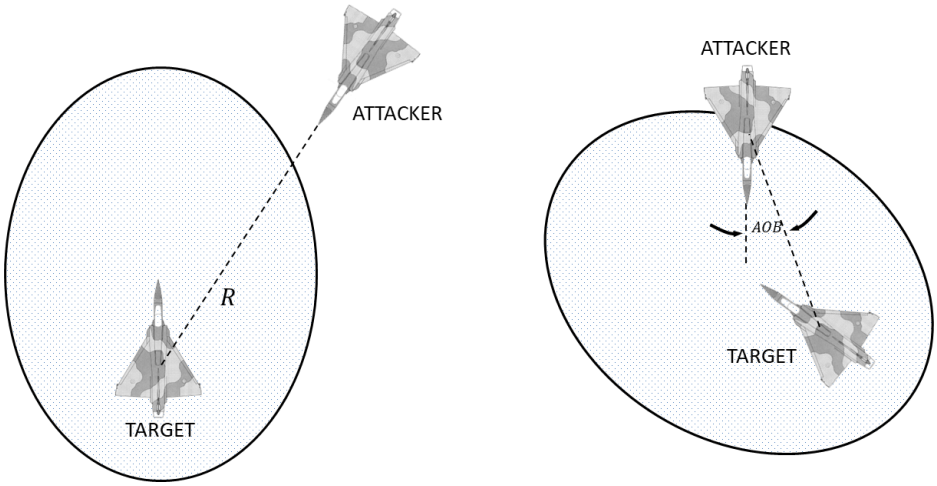

Figure 3.60: Simulation initialization [left] and intercept condition [right]. The shaded ellipses represent the missile's target-centered envelope.

Figure 3.61 shows the outcome of a typical aircraft-vs-aircraft simulation scenario. In the absence of related material in the literature, pilot feedback was used to investigate the validity of the resulting trajectories. Based on this input,

the trajectories of Figures 3.59 and 3.61 reproduce standard tactics for evading attacks from hostile aircraft and missiles respectively: Turning away from the attack with an in-plane manoeuvre is a textbook evasive manoeuvre, performed against both missiles and aircraft. In the former case, the turn is conducted at maximum vertical load factor and serves to move the aircraft as quickly as possible outside of the missile's kinematic envelope, exploiting the short burning time of its rocket motor. When used against an attacking aircraft, the manoeuvre has a dual purpose: Similar to the missile case, turning away from the attack serves to retain or increase the distance between the two aircraft, keeping the evader away from the attacker's weapon range. Contrary to this case, however, a lower vertical load factor is used, to minimize the loss of velocity during the turn and keep the evader in a position from which it may be possible to escape the attack by accelerating away from the attacker. The second objective of the manoeuvre is to achieve a reduction in the attacker's weapon range by placing him behind the evader and minimizing the relative velocity between the two aircraft; this effect is visible in Figure 3.61, in which the attacker is unable to get the evader within his weapons' range despite the decreasing distance between the two aircraft.

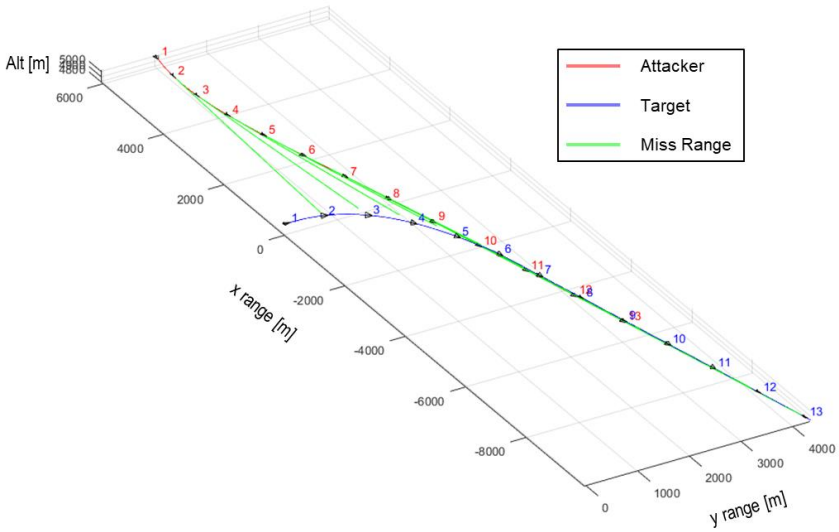

Figure 3.61: Schematic representation of a typical aircraft-vs-aircraft simulation scenario; the attacker is shown in red, the evader in blue and the green lines represent the missile's envelope.

4 RESULTS AND DISCUSSION

This Chapter presents the results obtained from a series of numerical experiments used to assess the performance of the proposed methods and investigate propulsion system effects on aircraft performance. The study is split into three Sections, dedicated to aircraft climb performance, mission performance and combat survivability respectively. In each case, a comparison between different engine configurations is used to unveil the associated differences in aircraft performance and is followed by a discussion on the findings of each of the scenarios evaluated.

4.1 Climb Performance

In the context of evaluating the effectiveness of the proposed climb simulation module and to demonstrate a potential application, a hypothetical engine upgrade scenario was examined. This considers a replacement of the aircraft's original J79 turbojet engine with the EJ200 low-bypass turbofan, which has a similar design air mass flow rate. Under this scope, engine models inspired by these engines were created based on data found in the public domain and making engineering valid assumptions.

The climb performance of three aircraft–engine configurations was evaluated using the proposed multi-objective climb path optimization methodology. A summary of their specifications is given in Table 4.1 and Table 4.4: Configuration C1 is the original aircraft configuration, while configurations C2 and C3 correspond to EJ200-equipped variants. Configuration C2 shares the same all-up mass (AUM) with configuration C1, assuming that, as a result of the reduced weight of the EJ200 engines, the airframe's weight is allowed to increase with the addition of extra equipment or internal fuel. Configuration C3 shares the shame airframe and internal fuel weight with Configuration C1, resulting in a reduced aircraft AUM.

Table 4.1. Specifications of the examined configurations.

Configuration	Engine Type	Mass [kg]		
		Airframe + Fuel	Engines	Total
$C1$	$J79$	15,512	3500	19,012
$C2$	$EJ200$	17,052	1960	19,012
$C3$	$EJ200$	15,512	1960	17,472

To compare the performance of the above configurations, two test cases were evaluated, their details being provided in Table 4.3. Case A examines a typical subsonic mission climb scenario, where an aircraft, after take-off, uses a military (maximum, non-afterburning) thrust setting to climb to the optimum cruise altitude. Case B, on the other hand, considers a maximum power supersonic climb, to be encountered in a supersonic, point-intercept-type mission.

Table 4.2: Engine Model Parameters

Parameter		J79	EJ200	Description
$\dot{m}_{SLS}$	=	$76\ kg/s$	$76\ kg/s$	Design Air Mass Flow
PR_F	=	–	4.2	Fan Pressure Ratio
n_F	=	–	0.88	Fan Isentropic Efficiency
PR_{HPC}	=	13.5	5.9	HP Compressor Pressure Ratio
n_{HPC}	=	0.84	0.87	HP Compressor Isentropic Efficiency
TET_{max}	=	$1{,}400\ K$	$1{,}750\ K$	Maximum TET
n_{HPT}	=	0.85	0.89	HP Turbine Isentropic Efficiency
n_{LPT}	=	–	0.9	LP Turbine Isentropic Efficiency
ABT_{max}	=	$1{,}800\ K$	$2{,}000\ K$	Maximum A/B Temperature

A population of 20 particles was selected and run for 300 low-level and 100 high-level iterations in all test cases. Four control points were employed for the test runs of Case A and six for the runs of Case B, corresponding to eight and twelve design variables, respectively. In both cases, PSO constants were set at $c_1 = c_2 = 1.7$ and $w = 0.3$. Results are presented in Figures 4.1-4.4 for Case A and Figures 4.5-4.8 for Case B. For reasons of clarity, only flight paths corresponding to minimum-time and minimum-fuel solutions are shown, intermediate flight paths being bounded within them.

Table 4.3. Test case specifications.

Case	Thrust Setting	Start		End	
		Mach	Alt [m]	Mach	Alt [m]
A	$Military$	0.3	0	0.9	10,000
B	$Maximum$	0.3	0	1.8	15,000

A qualitative assessment of the resulting trajectories indicates that these are in agreement with related theoretical estimates and published results [49, 50, 74, 75]: All paths begin with a level acceleration at sea level where the aircraft has its maximum acceleration capability. In the subsonic climb case, this is followed by an accelerated climb that follows the peaks of the Specific Excess Power (for the minimum-time climb) and Energy Efficiency (for the minimum-fuel climb) contours up to the specified end conditions; this is a good indication for the accuracy of the generated solutions, since the optimizer, by definition, uses no information about the gradients of the respective functions. In the supersonic climb case, the tracking of contours usually results in a dive occurring in the transonic region. In minimum-fuel climb paths, climbs begin at lower subsonic Mach numbers than in the respective minimum time paths, trajectories being shifted towards higher altitudes for improved efficiency. In general, in all cases and in accordance with the results of Reference [74], the resulting paths look like “smoothed” versions of E-M paths. This is because E-M solutions do not consider the energy loss during manoeuvres and assume that the transition between equal energy levels may be realized instantaneously; if the latter are considered, climb path optimization becomes a trade-off between accurate tracking of contours and avoidance of intense manoeuvres.

As far as the performance of the examined configurations is concerned; an inspection of Figures 4.1 and 4.5 denotes a clear advantage of the EJ200-equipped configurations. In the subsonic climb case; an average 14.5% reduction in fuel consumption was combined with 13.7% reduction in time to climb with respect to the aircraft’s original configuration at an equal aircraft AUM (Configuration C2). The above values were further increased to 23.6% and 22.7%, respectively, if the weight reduction resulting from the reduced engine weight were considered (Configuration C3). A similar picture was observed in

the supersonic climb test results: The average reduction in fuel consumption was 17.3% for configuration C2 and 25.3% for configuration C3 accompanied by a 6.7% and 18.9% reduction in climb time, respectively.

A comparison of the maximum power Specific Excess Power and Energy Efficiency contours of the three examined configurations unveils the different performance characteristics of the engines examined: The EJ200 is a low-bypass turbofan engine with a higher static thrust than the J79 turbojet. This accounts for an acceleration and efficiency advantage of the former over most of the aircraft's envelope, particularly at high altitude and low-to-medium Mach numbers. On the contrary, because of its turbojet cycle, the J79 has better performance at medium altitudes in the transonic Mach number range, gradually expanding to the entire altitude range as the Mach number further increases. In Case B, this results in smaller differences in TTC between configuration C1 and configurations C2 and C3 compared to the results of Case A (Figures 4.1 and 4.5). The different performance characteristics of the two engines also become evident by comparing the minimum-time supersonic climb trajectories of configurations C2 and C3 with that of configuration C1. The J79-equipped configuration (C1) favours an acceleration at medium altitude in the transonic regime, followed by a zoom climb to reach the specified altitude (Figure 4.6), whereas the EJ200-equipped configurations (C2 and C3) use a subsonic climb to high altitude followed by an accelerated supersonic climb to the desired conditions (Figures 4.7 and 4.8). On the contrary, minimum-fuel supersonic climb trajectories are similar for both engines, which lead to a rather "broad" front of optimal solutions for configuration C1 (Figure 4.5) compared to the respective results for configurations C2 and C3. The same, to a smaller degree, also apply to the results of the subsonic climb case, as may be observed in Figures 4.1-4.4: The greater "distance" between minimum-fuel and minimum-time trajectories for configuration C1 leads to greater variations in FTC and TTC among members of the resulting front. Consequently, this constitutes an additional advantage of the EJ200-equipped configurations since the relative coincidence between minimum-time and minimum-fuel climb paths minimizes the compromises required (in fuel when climbing for the minimum

time and the reverse) in each climb case. As a general conclusion, the characteristics of the low-bypass turbofan cycle appear to be better suited to typical aircraft mission requirements, leading to faster climbs with less fuel consumption. On the other hand, the regions where the performance of the turbojet is dominant are of little operational interest, a fact that is justified by the evolution of military aircraft engines since the development of the J79 in the late 1950s.

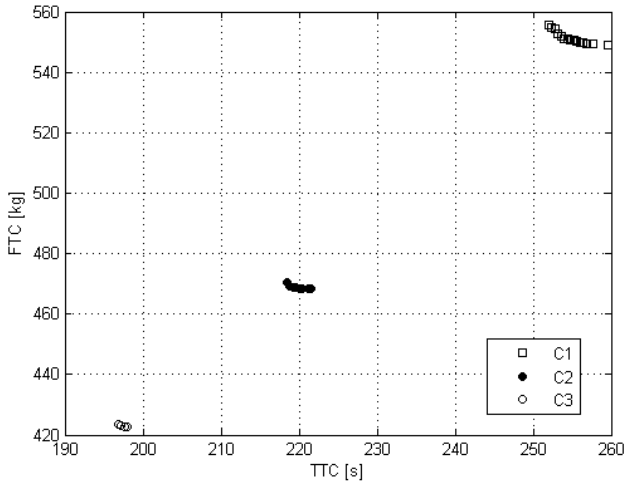

Figure 4.1. Case A; comparison of fronts of non-dominated solutions obtained for Configurations C1, C2 and C3.

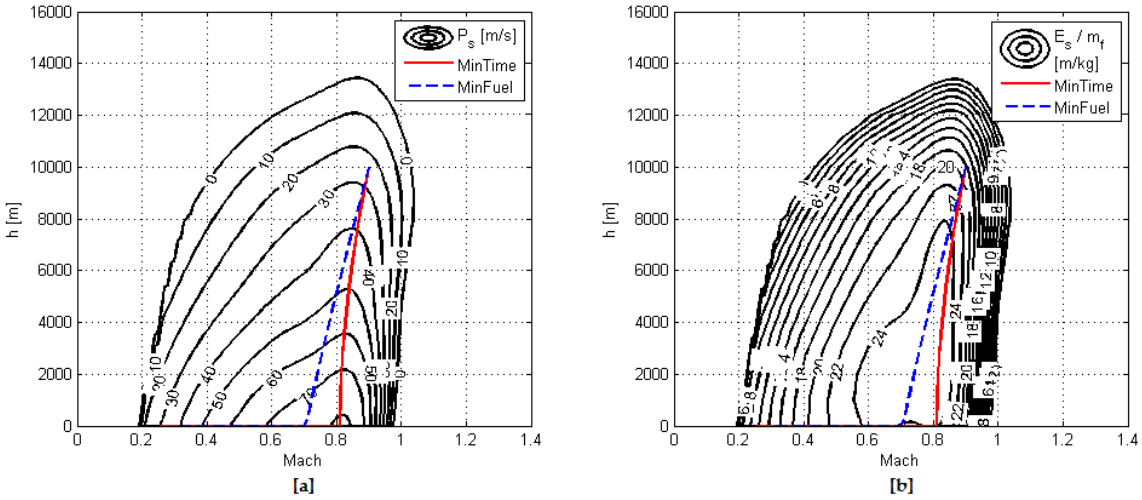

Figure 4.2. Case A, Configuration C1; Minimum Time and Minimum Fuel climb paths, plotted over contours of: Specific Excess Power (m/s) (a); and Energy Efficiency (m/kg) (b).

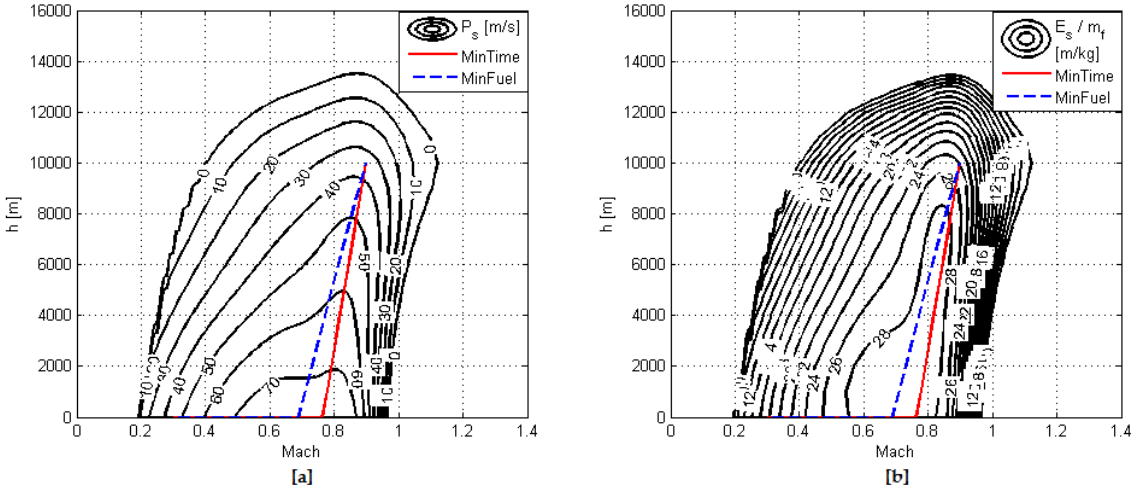

Figure 4.3. Case A, Configuration C2; Minimum Time and Minimum Fuel climb paths, plotted over contours of: Specific Excess Power (m/s) (a); and Energy Efficiency (m/kg) (b).

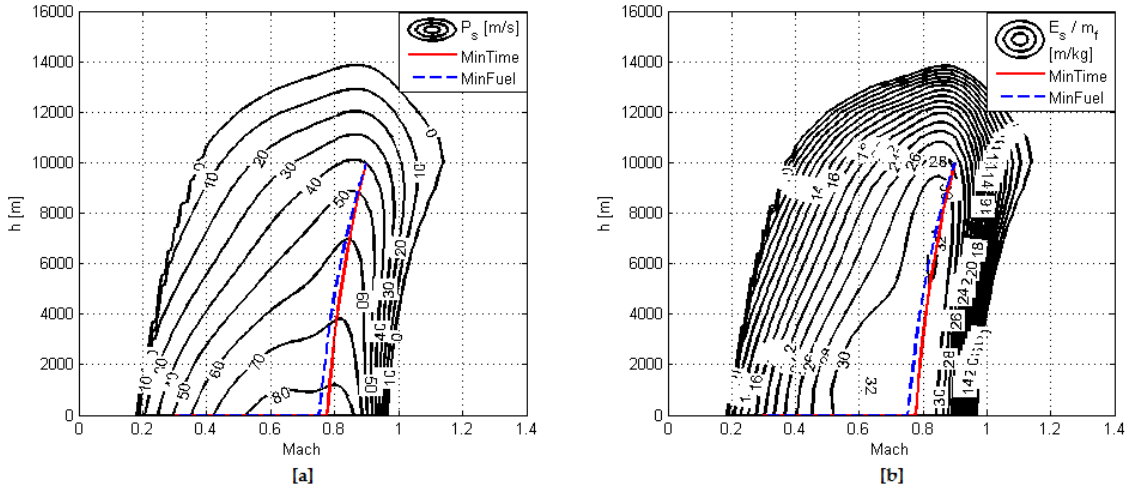

Figure 4.4. Case A, Configuration C3; Minimum Time and Minimum Fuel climb paths, plotted over contours of: Specific Excess Power (m/s) (a); and Energy Efficiency (m/kg) (b).

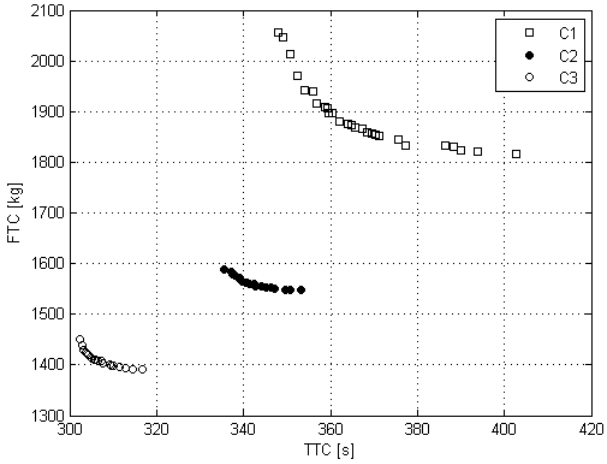

Figure 4.5. Case B; comparison of fronts of non-dominated solutions obtained for Configurations C1, C2 and C3.

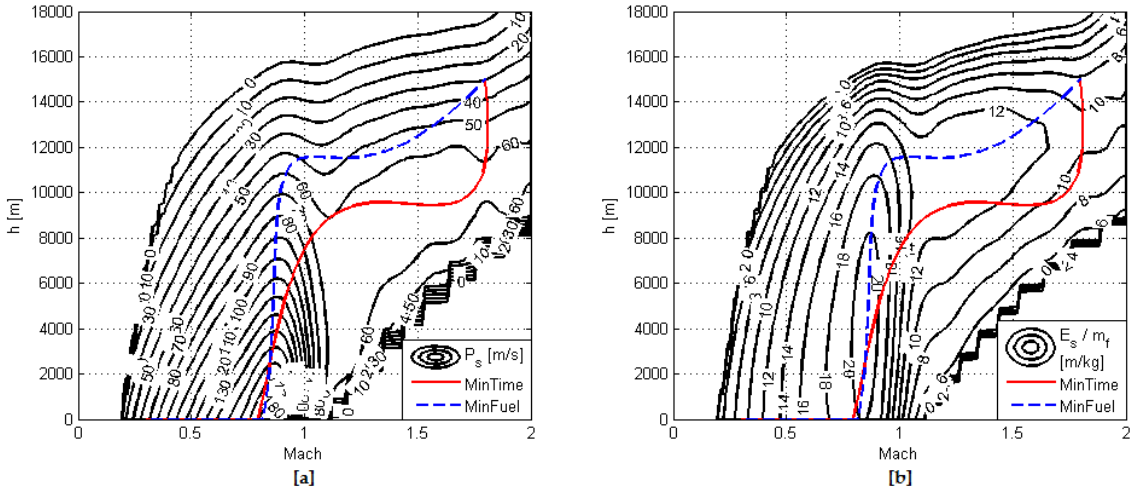

Figure 4.6. Case B, Configuration C1; Minimum Time and Minimum Fuel climb paths, plotted over contours of: Specific Excess Power (m/s) (a); and Energy Efficiency (m/kg) (b).

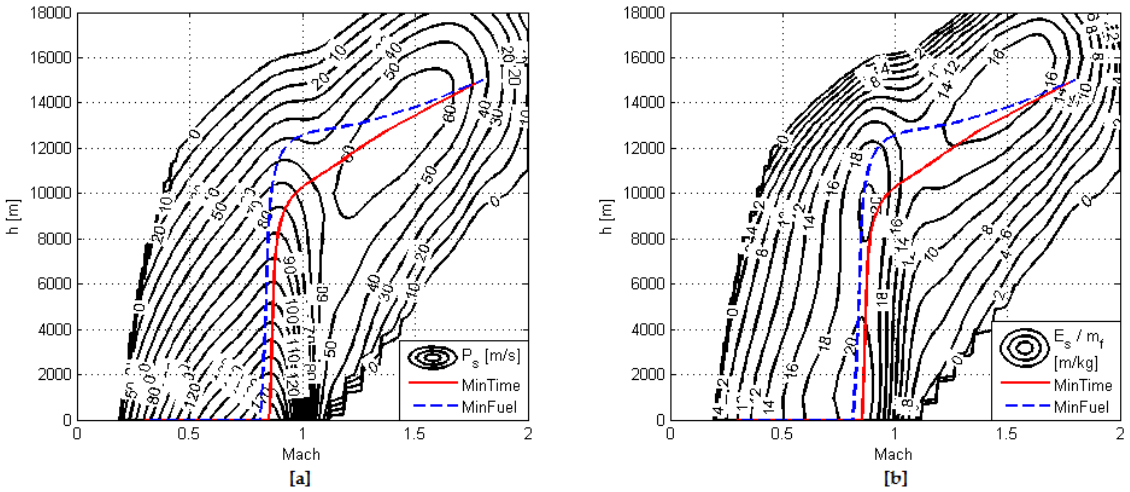

Figure 4.7. Case B, Configuration C2; Minimum Time and Minimum Fuel climb paths, plotted over contours of: Specific Excess Power (m/s) (a); and Energy Efficiency (m/kg) (b).

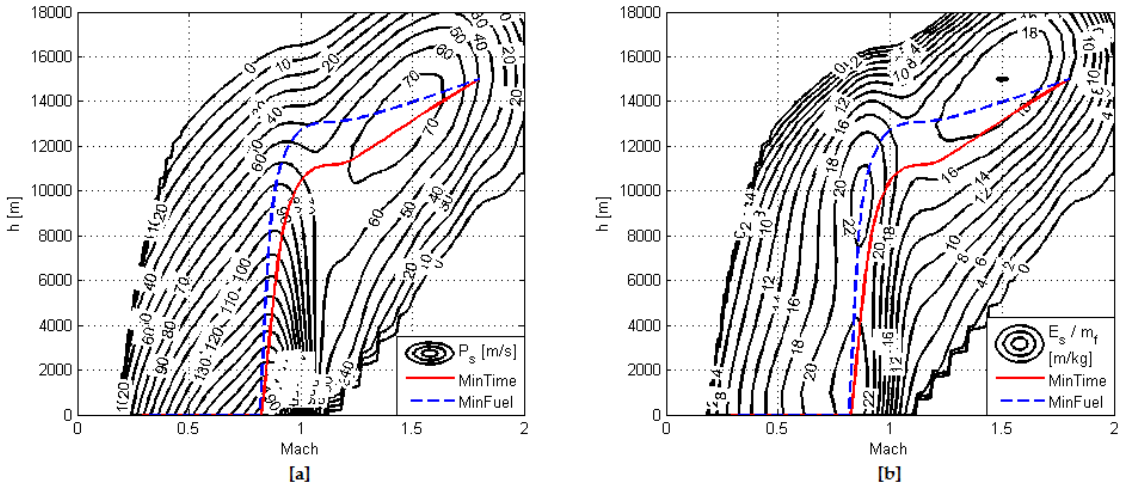

Figure 4.8. Case B, Configuration C3; Minimum Time and Minimum Fuel climb paths, plotted over contours of: Specific Excess Power (m/s) (a); and Energy Efficiency (m/kg) (b).

4.2 Mission Performance

In this Section, an example application of the developed methodology for aircraft mission performance assessment is presented. Similarly to the previous Section on climb performance, a study was performed based on a comparison

between two different engine propulsion system configurations for the same airframe: one selected to represent a new high-performance twin-spool afterburning turbofan engine and a second accounting for an older-generation engine sharing the same geometry: The two engines' specifications are given in Table 4.4. Aircraft reference area S was set at 30 m^2. The performance the two configurations is measured in the context of three mission types, representative of missions typically flown by a modern multi-mission aircraft:

- Mission 1 (M1 - Figure 4.9) represents a training sortie, in which the aircraft must cover the distance separating the training area from its home base. A minimum noise profile is used during the initial climb segment in order to minimize the disruption caused to populations living in the vicinity of the airfield; this is followed by a maximum-range cruise segment to the training area. Training is conducted using the engine's maximum power setting. Finally, maximum range cruise and descent profiles are employed for the aircraft's return to base. For this mission aircraft take-off weight was set to 10000 kg and the configuration's drag index (DI) to 3.
- Mission 2 (M2 - Figure 4.10) considers a supersonic interception scenario: the aircraft is scrambled from its base to intercept an incoming threat and follows a minimum-time trajectory to accelerate to supersonic speed. It then follows a constant altitude and Mach number cruise until it reaches its target. Combat is conducted at maximum power setting, following which the aircraft follows maximum range cruise and descent profiles back to its base. Similar to mission M1, this mission's aircraft take-off weight was set to 10000 kg and the configuration's drag index to 3.
- Mission 3 (M3 - Figure 4.11) is a typical Lo-Lo-Lo interdiction mission. The aircraft takes off with a payload of air-to-ground weapons and accelerates to Mach 0.9 at sea level. It then cruises at the same velocity and altitude, reaches its target and releases its payload before cruising back to its home base following the same cruise profile. Aircraft take-off

weight and drag index were set to 11000 kg and 3 respectively, not including the additional weapon load.

Table 4.4. Engine Model Parameters

Parameter		Engine 1	Engine 2	Description
$\dot{m}_{SLS}$	=	$90\ kg/s$	$90\ kg/s$	Design Air Mass Flow
PR_F	=	2.9	3.6	Fan Pressure Ratio
n_F	=	0.82	0.87	Fan Isentropic Efficiency
PR_{HPC}	=	5.17	8.9	HP Compressor Pressure Ratio
n_{HPC}	=	0.82	0.87	HP Compressor Isentropic Efficiency
TET_{max}	=	$1{,}600\ K$	$1{,}700\ K$	Maximum TET
n_{HPT}	=	0.85	0.9	HP Turbine Isentropic Efficiency
n_{LPT}	=	0.85	0.9	LP Turbine Isentropic Efficiency
ABT_{max}	=	$1{,}900\ K$	$2{,}000\ K$	Maximum A/B Temperature

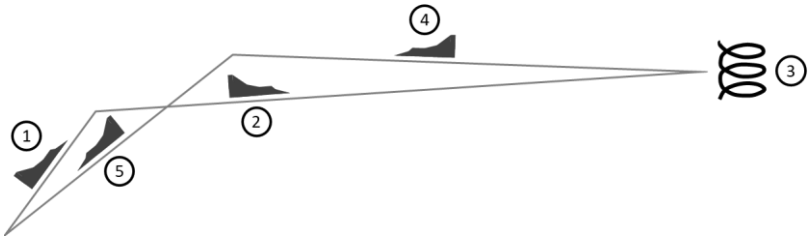

1. Min Noise Climb
2. Max range Cruise
3. Combat
4. Max range Cruise
5. Max Range Descent

Figure 4.9. Mission 1 profile specification

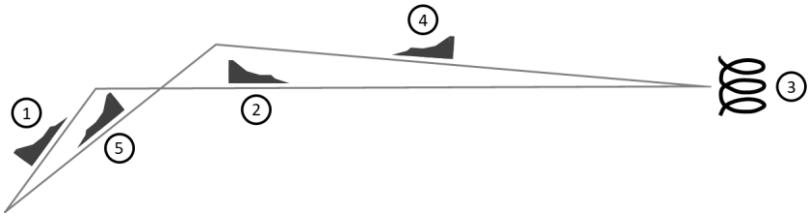

1. Min Time Climb
2. Const Alt Cruise
3. Combat
4. Max range Cruise
5. Max Range Descent

Figure 4.10. Mission 2 profile specification

1. Min Time Climb
2. Const Alt Cruise
3. Combat
4. Const Alt Cruise

Figure 4.11. Mission 3 profile specification

To allow for a parametric study on the potential of each propulsion system configuration, each mission type was split in two parts, corresponding to its inbound and outbound segments. Inverse simulation of the last segment (return to base) was used to extract the aircraft mass variation with mission range, subject to the aircraft's landing at its minimum landing mass, set to 8000 kg for all missions. The missions' outbound segments were simulated in the normal sense, and the point of intersection of aircraft mass with mission radius when cross-plotting the results from the two simulations where used to estimate the maximum range for each mission type. In mission profiles M2 and M3, a 360-degree turn at the aircraft's maximum sustained turn rate at the end-of-cruise conditions was used to calculate the fuel consumption corresponding to these missions combat segment.

The results obtained for mission profile M1 are plotted in Figures 4.12-4.14. Figure 4.12 shows the variation in aircraft mass with mission radius for both the inbound and outbound flight legs. As expected, engine E2 is more fuel efficient than engine E1, permitting the aircraft to cruise at 25% longer distances for the same fuel load. The same effect also applies to the available training time, as a small difference between the two engines at low mission ranges is magnified with increasing mission range (Figure 4.13).This suggests that the engines have approximately the same fuel consumption at maximum A/B mode. Finally, whereas the observed difference in fuel consumption during the initial minimum-noise climb segment is small, engine E2 was found to have a lower sound footprint with respect to the ground, its overall impact becoming even smaller compared to that of engine E1 due to the smaller duration of the corresponding climb segment: 190 seconds as compared to 238 seconds for engine E1 (Figure 4.14).

The supersonic profile of mission M2 unveils the difference in high speed cruise capability between the two configurations. To allow for a comparison in an operational basis, the mission's outbound supersonic cruise segment was simulated for a range of Mach numbers between 1.0 and 1.6, each time optimizing the engine schedule and flight altitude for maximum range. The

simulation results for maximum mission range (intercept radius) and the corresponding time-to-target (reaction time) are plotted in Figure 4.15, showing the performance gap between the two engine configurations. The introduction of the transonic cruise segment is shown to have a significant effect on the maximum mission radius for both engine configurations, compared to mission M1 which has a similar profile but uses the maximum range cruise strategy for both cruise segments: The effect is more significant for engine E2 (305 km or 31% of range reduction) than for E1 (159 km or 20% of range reduction). Despite this effect, the maximum attainable mission radius using engine E2 is 31% higher than that obtained with engine E1 (531 km), whereas, for any given mission radius, the E2-equipped aircraft is able to reach the target at least 2 minutes faster that the corresponding E1-equipped variant. The better efficiency of engine E2, attributed to its cycle characteristics, decreases at higher Mach numbers due to the fact that both engines must increasingly rely on the use of afterburning to produce the required thrust levels which leads to a large efficiency penalty. Figures 4.16-4.17 demonstrate this effect through a comparison of the engines' operating points for Mach 1 and 1.6 cruise.

In the context of evaluating propulsion system effects on aircraft performance at mission M3, multiple external store loadings were evaluated and used to estimate the maximum attainable mission range in each case. Aircraft basic take-off weight was set to 11000 kg, including internal fuel and an external fuel tank with a drag index of three. Following that, configurations considering the carriage of MK-84-type (m=1000 kg, DI=7) air-to-ground weapons were evaluated on the same mission profile; store loadings of 0-4 weapons were tested and the calculated mission ranges were used to form a payload range chart (Figure 4.18). Similar to the other mission profiles, the E2-engined aircraft variant displays greater overall capability, expressed as a 24% average increase in mission range or, perhaps more importantly, the ability to carry three more weapons for the same mission range. Simultaneously, as a result of its higher cruise bypass ratio, engine E2 has lower IR emissions than engine E1 (Figure 4.19); the increased use of afterburning to overcome the drag of the heavier store loadings decreases the difference in the IR signal generated by

the two engines; this effect is similar to what was observed in mission M2. In the general case, however, engine E2 also has a survivability advantage over engine E1, due to a lower probability of being detected by enemy sensors over a greater variety of flight conditions.

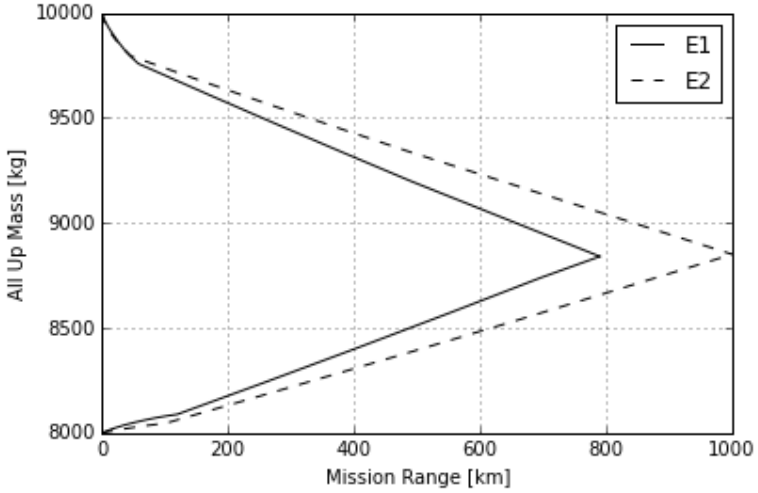

Figure 4.12. Mission M1: Aircraft mass vs mission range for engine configurations E1 and E2

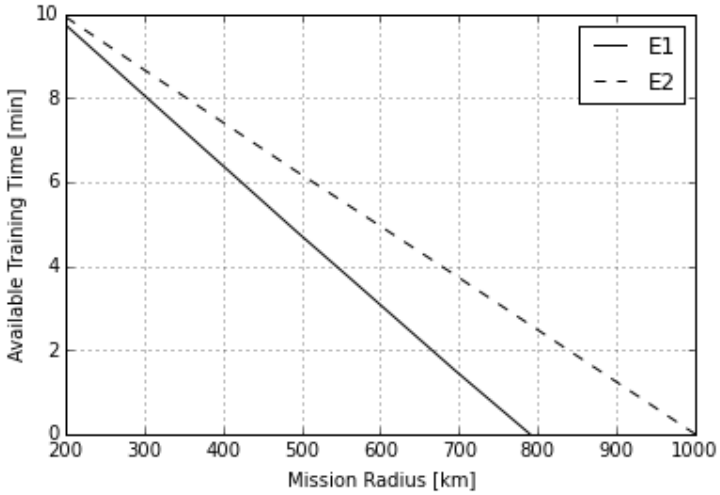

Figure 4.13. Mission M1: Available training time as a function of mission range for engine configurations E1 and E2.

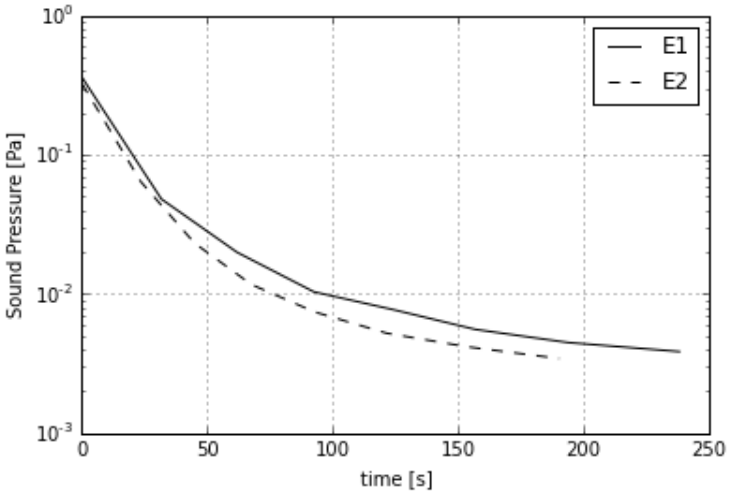

Figure 4.14 Mission M1: Noise sound pressure during the climb segment for engine configurations E1 and E2.

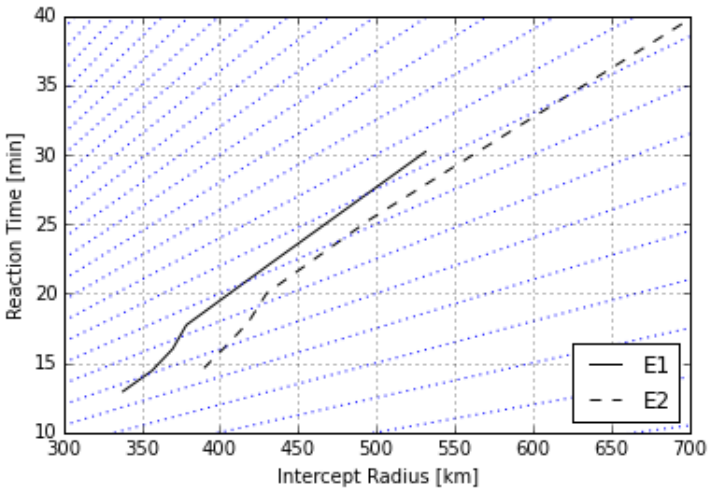

Figure 4.15. Mission M2: Reaction time vs mission radius for engine configurations E1 and E2. The dashed blue lines represent loci of constant velocity.

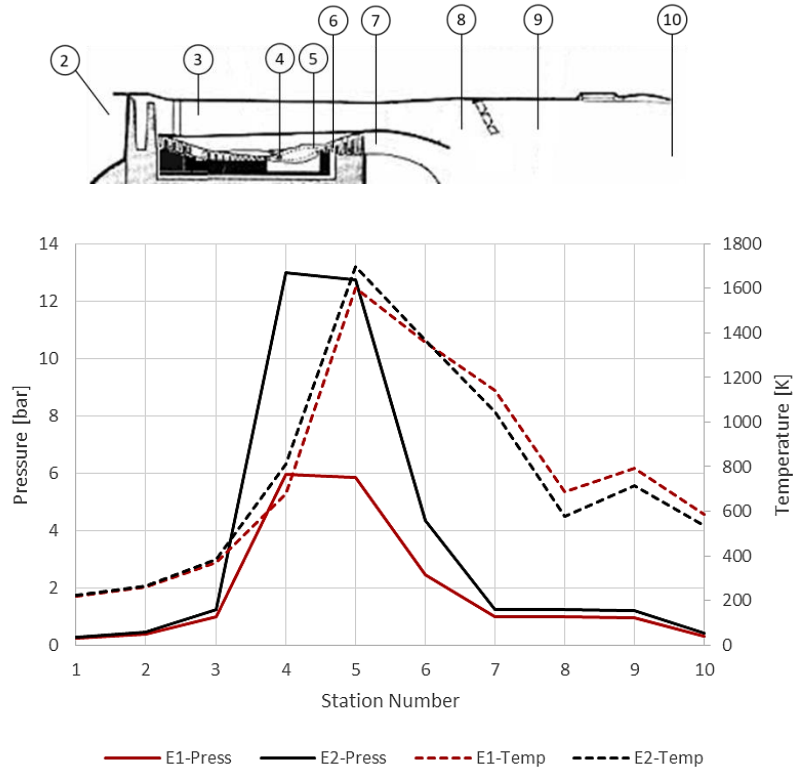

Figure 4.16. Mission M2: Comparison of engine cycles (core flow) for engine configurations E1 and E2 at Mach =1 cruise

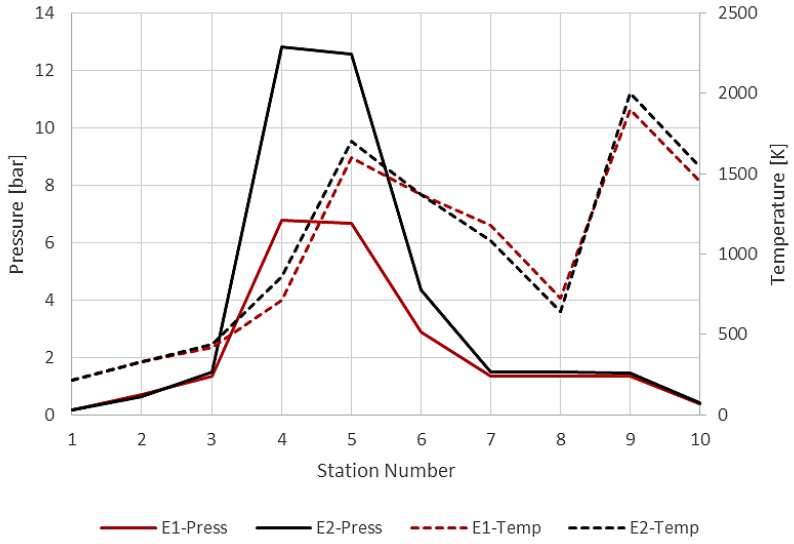

Figure 4.17. Mission M2: Comparison of engine cycles (core flow) for engine configurations E1 and E2 at Mach =1.6 cruise

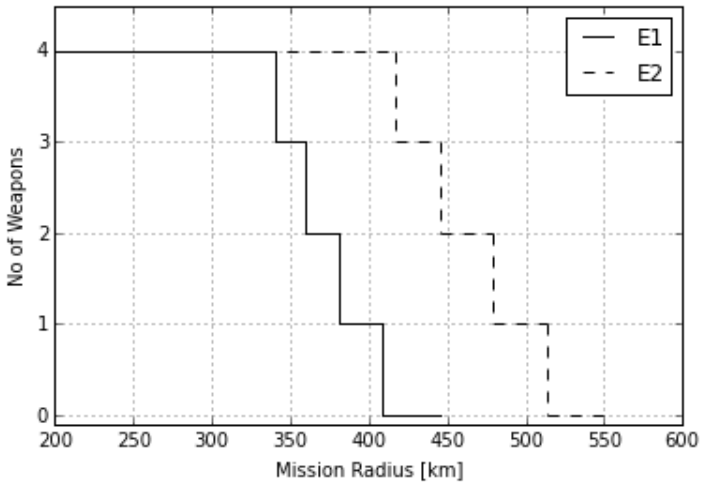

Figure 4.18. Mission M3: Payload-range chart for engine configurations E1 and E2. Each weapon corresponds to a generic 1000-kg air-to-ground store.

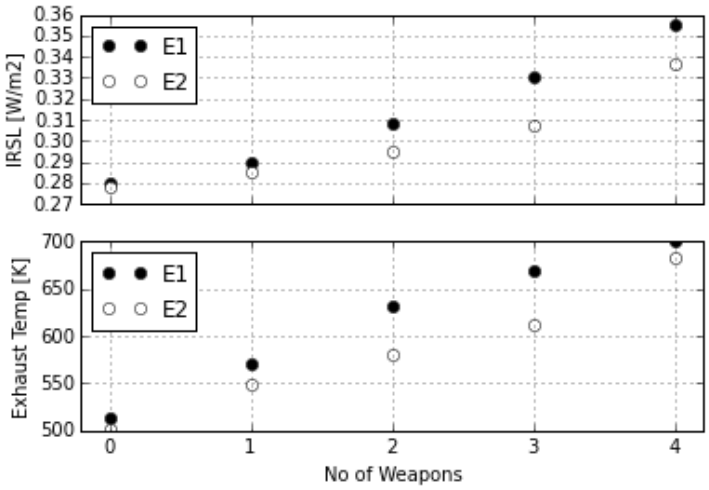

Figure 4.19. Mission M3: Exhaust temperatures and IR emissions during cruise for engine configurations E1 and E2

4.3 Survivability

In the same context as for the previously presented studies, a comparison between two different aircraft/propulsion system configurations was used to present propulsion system effects on aircraft survivability: One corresponding to a modern, high-performance turbofan engine and a second one simulating an older-generation version, sharing the same geometry. Table 4.5 contains the main parameters of the two engine models. Aircraft reference area S was set at 25 m^2.

Table 4.5: Engine Model Parameters

Parameter		Engine 1	Engine 2	Description
$\dot{m}_{SLS}$	=	$75\ kg/s$	$75\ kg/s$	Design Air Mass Flow
PR_F	=	4.2	3.2	Fan Pressure Ratio
n_F	=	0.88	0.82	Fan Isentropic Efficiency
PR_{HPC}	=	5.95	4	HP Compressor Pressure Ratio
n_{HPC}	=	0.87	0.81	HP Compressor Isentropic Efficiency
TET_{max}	=	$1{,}700\ K$	$1{,}500\ K$	Maximum TET
n_{HPT}	=	0.89	0.85	HP Turbine Isentropic Efficiency
n_{LPT}	=	0.9	0.85	LP Turbine Isentropic Efficiency
ABT_{max}	=	$2{,}000\ K$	$1{,}800\ K$	Maximum A/B Temperature

Three test cases were specified, covering different areas of the aircraft's flight envelope, as per Table 4.6. Aircraft and missile parameters were kept constant for all engagement scenarios, as specified in Section 3.5.1. The study was subdivided in two parts addressing power plant effects on the survivability against missile and aircraft threats respectively. The results obtained are presented in Sections 4.3.1-4.3.2.

Table 4.6: Test Case Specifications

Test Case	Altitude [m]	Mach
C_1	1,000	0.6
C_2	5,000	0.9
C_3	10,000	1.5

4.3.1 Missile-vs-aircraft survivability

Figures 4.20-4.22 present the calculated missile-vs-aircraft Lethal Zones (LZ) under flight conditions C1, C2 and C3: These were defined by the intersection between the lock-on range resulting from IR calculations and the missile kinematic envelope, as calculated from missile-vs-aircraft simulations.

The left part of Figures 4.20-4.22 presents the missile envelopes against non-manoeuvring aircraft cruising at the specified flight conditions: engine throttle setting was set to achieve constant-speed cruise for each aircraft/engine configuration. In these cases, it can be noted that the lock-on envelope bounds

most of the missile envelope except for an area at the rear of the aircraft where the envelope's limit is kinematic. Due to its greater efficiency, engine 1 has a lower exhaust temperature than engine 2 when generating the same thrust and, as a result, this leads to a smaller missile lethal envelope for engine 1 in cases C1 and C2. In case C3, both engines make use of the afterburner mode and have roughly the same exhaust temperature. With increasing altitude and Mach number, the airframe and engine exhaust become hotter and the atmospheric transmittance increases leading to an expansion of the aircraft lock-on range and, consequently, of the entire missile envelope. To add more, the kinematic envelope is also expanded due to the greater closure velocity between the missile and the aircraft along with the reduced drag of the missile resulting from the change in air density at higher altitudes.

The right part of Figures 4.20-4.22 presents the missile envelopes against manoeuvring aircraft initialized at the specified flight conditions: in these cases, the maximum-power throttle setting was used to maximize aircraft manoeuvrability, leading to an expansion of the aircraft's lock-on envelope, to such an extent that it almost entirely covers the respective missile kinematic limit. Lock-on range is in this case larger for engine 1, because of the higher afterburner temperature at maximum throttle. Evasive manoeuvres were shown to have a significant effect on the missile's kinematic envelope, mainly in cases of front-quarter attacks, where, depending upon the flight condition a 30% reduction to the missile lethal range can be achieved. By comparing the results for the two engines (Figure 4.23) it was found that the propulsion system has little effect on the missile's kinematic envelope, since the exact same results were obtained in all cases for both engines despite a 20% thrust advantage of engine 1 compared to engine 2. In the same context, it was found that non-zero values of AOB have a pronounced effect on the shape of the kinematic envelope, in agreement with qualitative data from the literature [99]. Under this scope, multiple runs were conducted at each flight condition to construct generalized missile envelopes accounting for these effects to be used for aircraft-vs-aircraft studies.

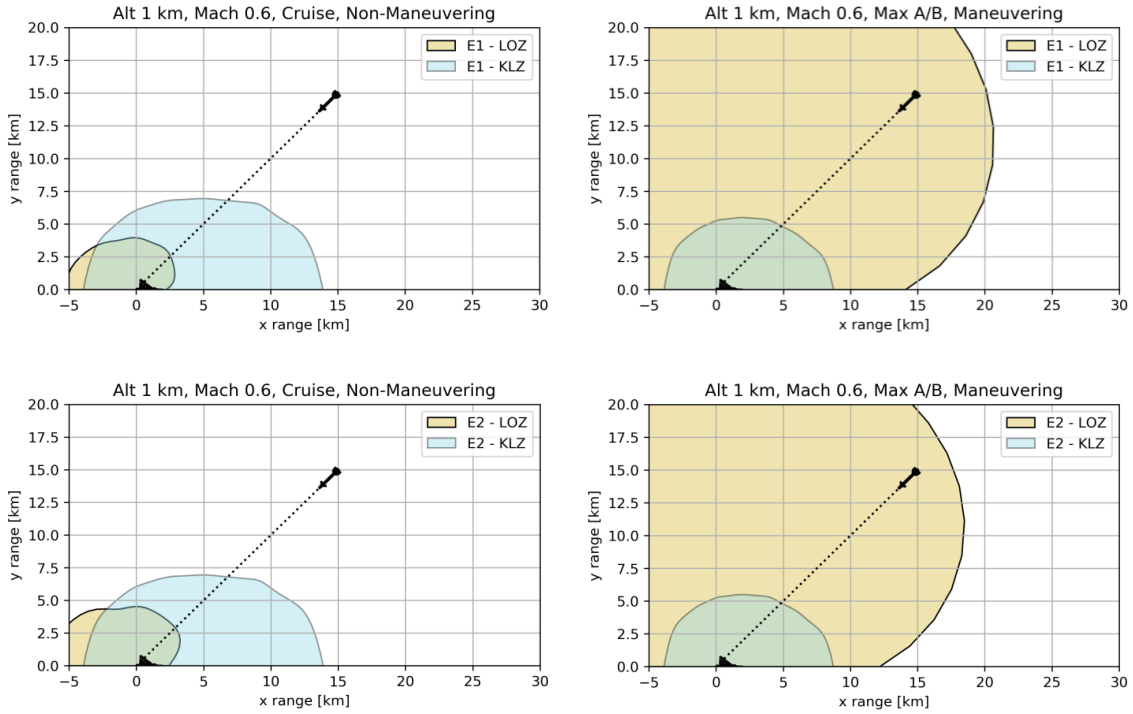

Figure 4.20: Flight Condition C1; missile lethal zones (LZ) against non-manoeuvring (left) and manoeuvring aircraft (right). Results for missile Kinematic Lethal Zones (KLZ) against non-manoeuvring and manoeuvring targets, along with Lock-On Zones (LOZ) for engine 1 (E1) and engine 2 (E2) are presented. Missile lethal zones are defined by the intersection between KLZ and LOZ corresponding to each configuration.

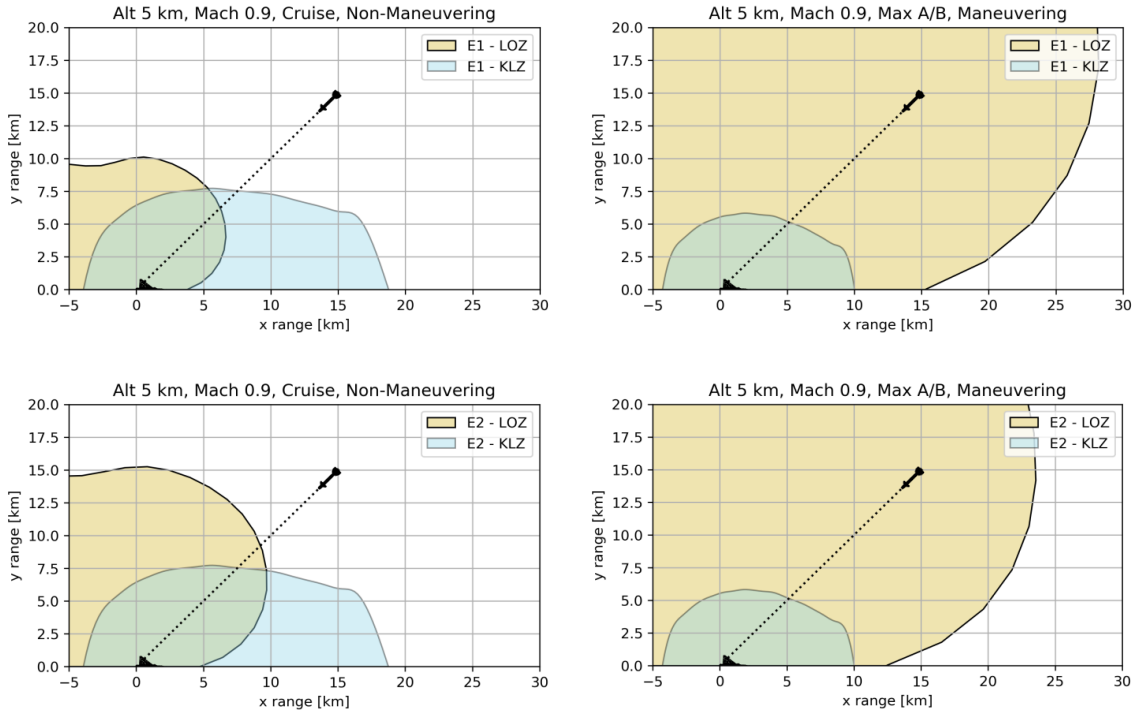

Figure 4.21: Flight Condition C2; missile lethal zones (LZ) against non-manoeuvring (left) and manoeuvring aircraft (right).

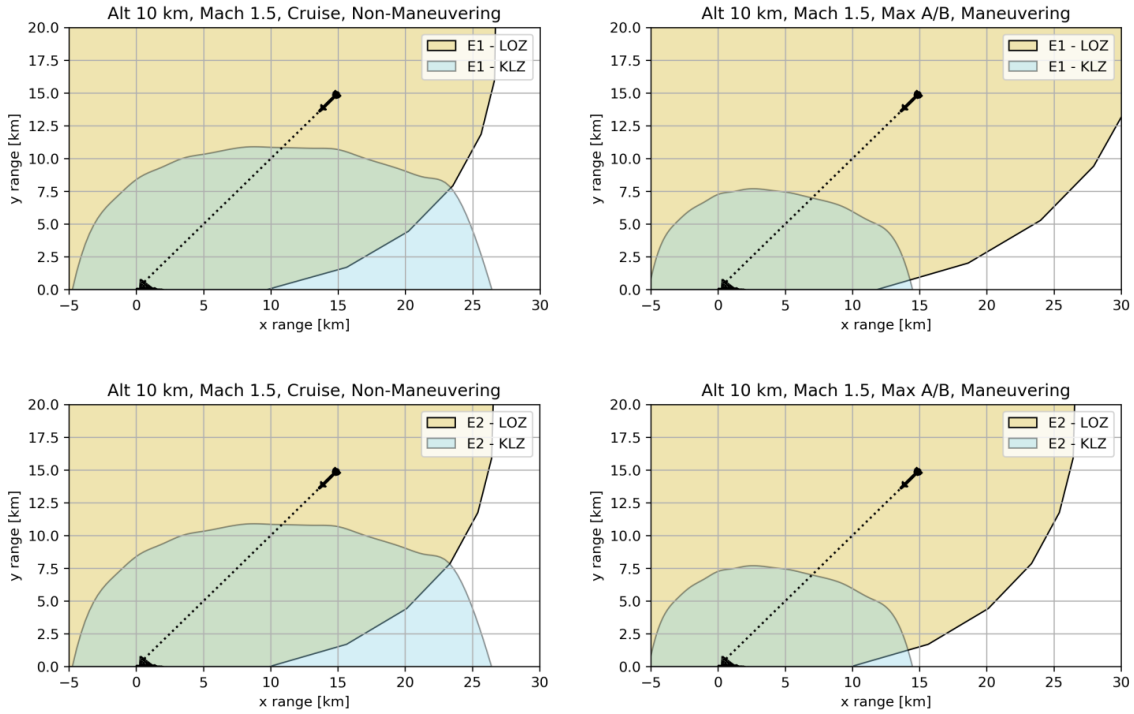

Figure 4.22: Flight Condition C3; missile lethal zones (LZ) against non-manoeuvring (left) and manoeuvring aircraft (right).

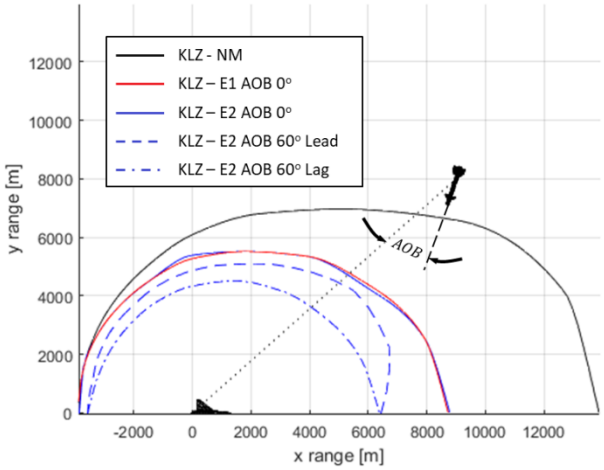

Figure 4.23: Flight Condition C1; missile Kinematic Lethal Zones (KLZ) for various engine configurations and initial conditions.

4.3.2 Aircraft-vs-aircraft Survivability

Using the missile envelopes generated by parametric runs of the missile-vs-aircraft scenario, the study was extended to the aircraft-vs-aircraft case. In order to construct equivalent lethal zones (named under the term Aircraft Lethal Zones - ALZ) for the latter case, both aircraft where initialized at the same altitude and airspeed with AOB set to zero. Both engine types (in all cases using the maximum power throttle setting to maximize manoeuvrability) were altered between the attacking and target aircraft to allow for an assessment of thrust effects on the size of the generated ALZs.

Figures 4.24-4.26 display the results obtained for various aircraft configurations and flight conditions C1-3 in comparison with the corresponding missile kinematic envelopes. To provide a common reference, cases with identical opponents are also presented: the latter unveil that the attacks from the frontal aspect provide the attacker with a positional advantage, leading to a local extension to the ALZ at the front with respect to the MLZ. The extent of this change depends upon the flight condition which defines the target's ability to

turn away from the attacker without sacrificing speed: For this reason, a maximum occurs in case C3, in which, due to the supersonic initial conditions, closure velocity is high and the target's turn performance is lower than in the subsonic cases C1 and C2. This approximately corresponds to 2.2 km of increase in ALZ for case C3 (Figure 4.26) compared to 0.9 km for case C1 (Figure 4.24) and 0.7 for case C2 (Figure 4.25).

A consistent finding within all the cases examined is that, contrary to the observations from the respective missile-vs-aircraft scenarios, engine thrust has a clear effect on the aircraft's offensive and defensive capability. In terms of offence, thrust advantage is translated into an approximately uniform expansion of the ALZ around the target, which is more pronounced for rear-aspect attacks due to the attacker's ability to accelerate faster than the target and consequently attack from longer range. This effect is more evident in subsonic cases C1 (Figure 4.24) and C2 (Figure 4.25), whereas the difference is smaller in case C3 (Figure 4.26) in which, due to the supersonic flight condition, the difference in performance between the two engines is smaller (engine 2 has lower bypass ratio than engine 1). As far as the aircraft's defensive capability is concerned, a similar trend can be observed; in all cases engine 2-vs-engine 1 ALZs marginally extend beyond the corresponding MLZs, meaning that lower-thrust opponents only get chances to score kills in cases when the target does not manoeuvre until entering the attacker's missile envelope. Due to the smaller performance margin between the two engines in the supersonic regime, in case C3 the engine 2-vs-engine 1 ALZs are expanded approaching that for equal-thrust opponents (Figure 4.26).

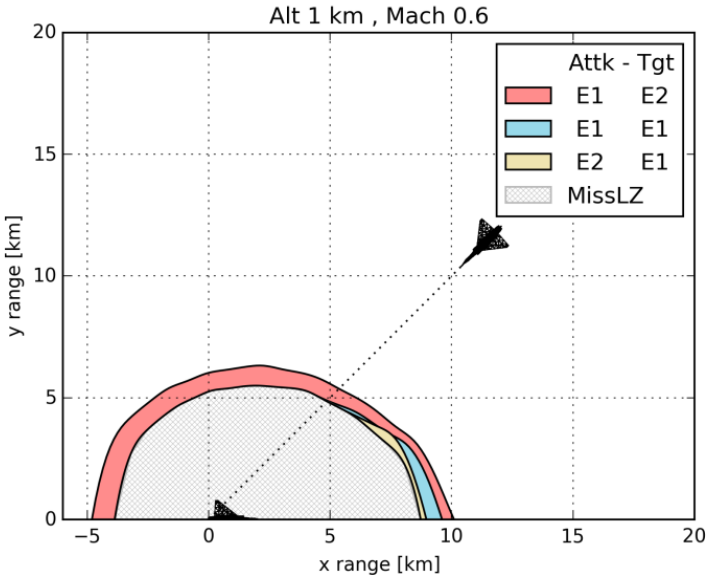

Figure 4.24: Flight Condition C1; comparison between Aircraft Lethal Zones (ALZ) for different aircraft configurations.

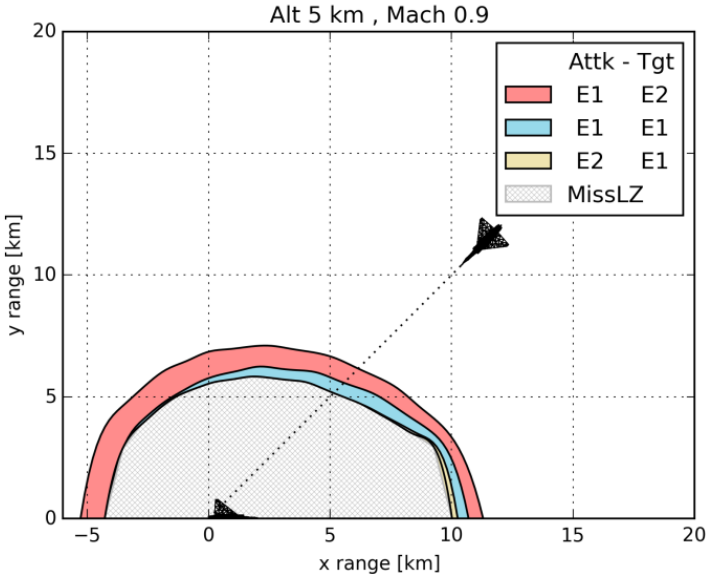

Figure 4.25: Flight Condition C2; comparison between Aircraft Lethal Zones (ALZ) for different aircraft configurations.

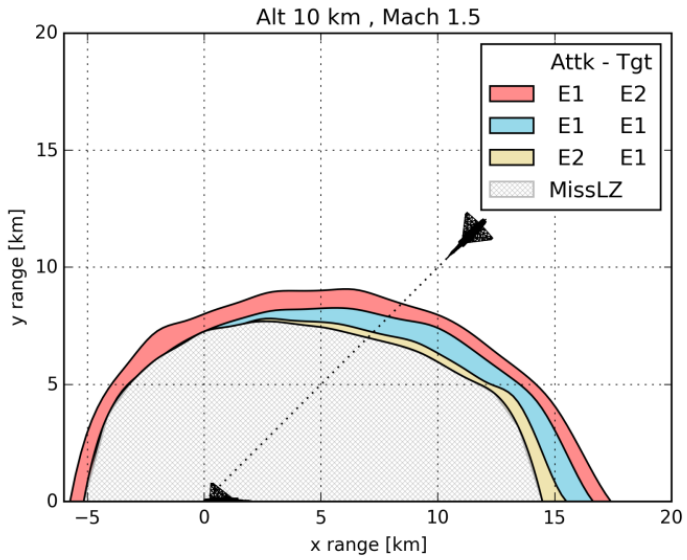

Figure 4.26: Flight Condition C3; comparison between Aircraft Lethal Zones (ALZ) for different aircraft configurations.

5 CONCLUSIONS

In this study, a computational module was developed, under the scope of quantifying the contribution of the propulsion system to different aspects of military performance. This comprises models representing the aerodynamic characteristics, IR and noise emissions of a generic military aircraft which are combined with simulation-based methods to assess aircraft climb, mission and combat performance. Work on the project was focused on four main tasks, which are presented in this Chapter together with the conclusions that were reached on the course of their development:

1. The synthesis of a generic low-cost representation of a military aircraft covering aircraft aerodynamics, airframe/propulsion system aerodynamic interference, IR and noise signature which is suitable for use in the context of large-scale parametric studies and trajectory optimization cases. The resulting aircraft performance platform is unique in the open literature in that it accounts for multiple aspects of interaction between the aircraft and the propulsion system, setting the basis for future multidisciplinary analyses on aircraft/propulsion system integration. All models were developed and validated using published data, leading to the following observations:

- The combined effect of throttle dependent forces on the aircraft accounts for 5% of the total aircraft drag in a typical cruise condition, based on the output of the developed models. The afterbody force is significantly affected by the boattail angle, leading to 62% increase as the nozzle angle varies from 6 degrees to 20 degrees at high subsonic Mach numbers. In the supersonic region this effect becomes stronger, leading to a sevenfold increase in drag for the same variation in afterbody angle. Exhaust pluming was shown to introduce a reduction to afterbody drag with increasing nozzle exit pressure; negative values were observed for exit pressure ratios higher than 1.8, for a typical nozzle configuration.
- The low lift-to-drag ratio of a military aircraft is significantly compromised by the installation of external stores: a typical 370-gal wing tank causes

an increase of 6% in the aircraft's total drag in a typical cruise condition, not considering the increase in aircraft weight.

- Representing the entire aircraft by means of its principal IR-contributing components, namely the skin, exhaust tailpipe, exhaust plume and turbine face-each modelled as an anisotropic source of radiation-was found to be a valid approach for obtaining simple estimates of aircraft IR signature. In this context, the use of a 3-D aircraft geometry was required, in order to properly represent the directivity of each one of these IR sources.
- To account for the dependency of the exhaust plume shape and temperature distribution on the engine's operating condition, a plume temperature model was developed, based on a combination of semi-empirical formulations and data available in the literature. The model's performance was tested against CFD data and was found to output correct-trend-and-magnitude temperature distributions, subject to the limitations of the simple methodology that was adopted. In particular, the plume model was unable to capture the temperature oscillations resulting from the complicated flow interactions occurring within supersonic over/under-expanded jets, however, its predictions were shown to approximate the local average temperature values to a sufficient degree.
- Aircraft noise modelling was based upon a synthesis of a widely-used method for jet noise prediction with an empirical approach for sonic boom amplitude estimation. Simulations unveiled that, other than the rather obvious effects of jet velocity and the distance from the source, the magnitude of the jet noise is strongly affected by the freestream velocity of the air surrounding the exhaust jet: high freestream velocity promotes the mixing of the jet with the surrounding flow, leading to noise reduction. In the supersonic regime, the contribution of the jet noise to aircraft signature becomes much less important, due to the fact that the latter is dominated by the sonic boom whose peak amplitude, depending on the flight condition, can be up to two orders of magnitude higher than the noise originating from the exhaust jet.

2. The development of a new multi-objective trajectory optimization technique for climb performance analysis. A novel two-objective formulation of the aircraft climb trajectory optimization problem was used to generate a pareto-front representation of aircraft climb potential which clearly shows the compromise between climb time and fuel consumption for a given aircraft configuration:

- As part of this methodology, a new approach for guidance in the Altitude-Mach plane using aircraft attitude control was proposed and tested over a wide range of trajectories. The proposed guidance law demonstrated robustness in tracking different trajectories, its performance being limited by aircraft dynamics, i.e. the flyability of the tracked trajectories
- A two-level optimization procedure was introduced, using Energy-Manoeuvrability trajectory estimates as an initial low-fidelity approximation to the actual solutions, which are evaluated at the second level using a simulation to calculate the optimization function values. The proposed optimization approach demonstrated consistently faster convergence than a single-level scheme using the same optimization solver.
- A performance comparison between conceptual J79- and EJ200-equipped variants of an F-4-like aircraft was used as an example application of the climb performance methodology, as part of a hypothetical engine upgrade scenario. Results denoted a clear advantage of the EJ200-equipped configurations in both subsonic and supersonic climb conditions: on average, 15% faster climbs were achieved with 20% less fuel consumption. As expected, the characteristics of the low-bypass turbofan cycle were found to be better suited to aircraft mission requirements, while the regions where the performance of the turbojet was dominant were of little operational interest; a point that is clearly justified by the evolution of military aircraft engines since the development of the J79.

3. The expansion of the classical Energy-Manoeuvrability (E-M) technique to form a new full-mission simulation procedure in which concurrent optimization of the aircraft's trajectory and the engine control schedule is performed. A modification of the inputs and objectives of the original method was combined with the introduction of aircraft IR and noise emissions as variables to the trajectory optimization problem, establishing new types of optimal climb and descent trajectories.

- As a result of the longer time-scales involved compared to simple climb segments, the simulation of full mission profiles is a much more demanding task, primarily due to the associated rise in computational requirements. Using an energy-based quasi-static approach for mission simulation allows for using a coarse discretization and significantly reduces the time required for computations. This strategy also has the advantage of breaking down the trajectory optimization problem to a series of sub-problems which are easier to handle and possible to solve in parallel, to further reduce simulation time.
- The developed trajectory optimization technique demonstrated the validity of the E-M solutions to higher-dimensional input spaces by replacing the graphical solution with a gradient-based optimization solver. Following experimentation with various solvers, a first-order variable-step method was deemed as the best choice for a direct interface with the engine modelling software, to keep intermediate solutions within the models' feasible space without significantly compromising convergence speed. Using this approach, the use of E-M in descent profiles was also made possible, using the same optimization functions and by simply altering the engine models' initialization.
- The feasibility of minimum noise and IR trajectories was validated through a series of tests considering aircraft climb profiles and cruise points. In the same context, a new "maximum range" formulation to aircraft climb and descent trajectories was demonstrated and shown to improve the cruise efficiency of climb and descent profiles over the traditional minimum-fuel formulation.

- At constant altitude and Mach number cruise, TET, nozzle throat and exit area were shown to be the most important engine control inputs for adapting engine performance to match the requirements of different objectives. Similar observations could also be made in climb optimization cases, though in the latter scenarios it was the trajectory's shape in the altitude-Mach number that was found to be the dominant control parameter, results being strongly affected by the type of objective function used.
- The developed full-mission simulation methodology was used to demonstrate the performance margin between a modern turbofan engine and an older generation engine in the context of three mission scenarios. Sharing the same airframe, the newer generation engine achieved 25% better range in a training mission, 2 minutes less reaction time for the same radius in an intercept mission and could carry 3000 kg more payload for the same mission radius in a low-level interdiction mission profile.

4. The development of a new methodology for assessing aircraft survivability, considering both the aircraft's IR signature and aircraft/missile kinematic performance. This constitutes a new approach to the quantification of propulsion systems effects on aircraft survivability that is based on a combination of aircraft IR signature and kinematic simulations of missile-vs-aircraft and aircraft-vs-aircraft scenarios. The latter were applied to parametric studies dedicated to the estimation of aircraft attack and self-defence capability against manoeuvring opponents.

- The optimization of aircraft evasive manoeuvres demonstrated that a level turn away from the attack is the optimal defensive strategy against both attacking aircraft and missiles.
- The study unveiled that the performance of the target aircraft's propulsion system has essentially no effect on missile kinematic envelopes but does influence aircraft lock-on range which is related to the engine exhaust's temperature distribution. More fuel-efficient engines

tend to generate lower IR emissions which lead to a reduction in the size of the missile's lethal zone. The effect is more apparent at higher altitudes and high subsonic/transonic flight conditions, due to the higher throttle settings used during cruise and because of the higher atmospheric transmittance which allows IR signals to travel greater distances.

- As the engine is switched to afterburning mode for air combat manoeuvring, the aircraft lock-on envelope expands to such an extent that the missile envelope is practically limited only by its kinematic performance.
- Effective aircraft evasive manoeuvres were found to drastically reduce the missile's kinematic envelope, though this result is a function of the aircraft's instantaneous manoeuvrability and is practically unrelated to engine thrust performance.
- As far as the aircraft-vs-aircraft cases are concerned, contrary to the respective missile-vs-aircraft scenarios, the engine's thrust performance was shown to have a measurable effect on the equivalent 'aircraft lethal zones' (ALZs), translated into both offensive and defensive advantages for aircraft with higher thrust over their opponents, the extent of which depends upon the thrust increment between the opponents at the specified flight condition. Among the configurations and flight conditions examined, the maximum ALZ expansion observed was 1 km compared to the equal-opponents case, whereas the corresponding ALZs of low-thrust attackers attacking higher-thrust targets were found to shrink down to approximately the size of the missile lethal zone.

6 FURTHER WORK

The present study introduced a unified methodology for assessing the combined performance of military airframe/propulsion system configurations as function aircraft operational mission requirements. This research work was performed under the scope of establishing the basis of a new TERA framework dedicated to military aircraft propulsion systems. Therefore, from this point, the most obvious step forward would be the completion of this framework with the introduction of all the missing aspects, such as weight estimation, lifecycle cost, emissions modules, in a similar manner as for all other TERA applications. This will allow for multi-disciplinary analyses on propulsion system design trade-offs extending further than pure mission performance, towards a full lifecycle assessment of candidate designs.

Given that this projects' aim was to develop and demonstrate the associated methodology, the example applications presented were by no means exhaustive and served partially to provide a physical validation for the developed models. A large-scale parametric investigation is hereafter required in order to quantify the connection between the propulsion system configuration and aircraft performance. Under this scope, the use of the tools developed can be the subject of future studies that will investigate key trends in aircraft performance associated with engine design and the adoption of new propulsion technologies.

In this context, it would be useful to state the limitations of the presented approach and suggest areas for further research in order to expand its applicability and improve its accuracy:

- The aircraft models' development was based upon published data corresponding to 'typical' fighter aircraft configurations, representative of most contemporary jets. Though this is sufficient to cover a wide range of aircraft platforms, the fact that modern trends point towards low-observable airframe designs should be accounted for, which will require some modification and expansion of the existent methods. In particular:

- A new model for airframe drag is required, taking into account the particularities of low observable configurations (geometry, no vertical surfaces etc). In the absence of published data, this could be created using either an engineering or CFD approach and used to compliment / replace the current drag model.
- The afterbody force model is currently limited to conical, axisymmetric nozzle configurations. Non-axisymmetric nozzles are typically used in low-observable platforms but are not as well documented in the open literature. The same also applies to aircraft intakes, for which new diverterless designs with pronounced S-ducts are being used to mask the compressor face. An investigation of possible modelling techniques should be realized to define a strategy for predicting throttle-dependent forces and inlet pressure recovery for these cases.
- Under the same scope, similar modifications need to be introduced to the developed IR model, including new airframe geometries simulating IR masking techniques and aircraft skin temperature distribution. More importantly, a generalized plume model is required, able to estimate the exhaust temperature distribution of nozzle configurations other than the axisymmetric single-flow case covered by the model used in this project. In this study, aircraft IRSL was identified as a critical factor for combat survivability, therefore, an improvement of the available IR prediction tools would allow for optimizing the propulsion system's configuration with respect to this objective. Following that, combined with suitable kinematic models, the same method could be also applied to survivability studies of a wider range of air vehicles, not strictly classified as fighters, but operating in the same threat environment, such as military transport aircraft, helicopters and UAVs.

- For reasons of simplicity, aircraft modelling in this project did not include the air and power bleed requirements of the airframe. which are known to

introduce performance penalties to the propulsion system. Establishing models for these effects would allow for measuring their influence on aircraft mission performance in the context of realistic mission scenarios, particularly with respect to the increased power requirements of modern on-board electronic warfare equipment.

- In this study, propulsion system effects on aircraft mission performance were demonstrated in the context of three sample mission scenarios. The developed trajectory optimization utility can cover most of the standardized mission scenarios, therefore some effort should be made to configure new mission profiles and their associated mission performance metrics, which will form the basis of a more complete framework for the multidisciplinary performance assessment of candidate propulsion system configurations. It is also noted that, with minor modifications, the same tool can also be applied to simulate missions of different air vehicle types such as civil or transport aircraft and helicopters.
- To assess aircraft survivability, simple guidance models were developed and used to approximate actual air combat manoeuvring in air-to-air combat scenarios. The methods applicability to air-to-ground combat can be expanded through a simple modification of the missile-vs-aircraft scenario, considering the different initial conditions and vehicle parameters involved. Under this scope, the introduction of a model for aircraft radar signature would also be beneficial in expanding the threat modelling capabilities of the existent method. Finally yet importantly, as recent research on the field has pointed out, a major improvement in the realism of the simulated combat scenarios can result from the adoption of modern artificial intelligence techniques to set up and train the combat agents.

Summarizing, it may be stated that this project's main contribution is a methodology for the multidisciplinary performance assessment of military aircraft propulsion systems. In their current form, the developed tools are fully usable and can cover a wide range of test scenarios. However, the project is by no means finalized, as there exist several areas of improvement the most

important of which were listed above. The possibility for future expansion has been considered during the development of the computational routines, which have been set-up in a modular fashion, to allow for easy upgrading/replacement of their functionalities.

The next major milestone in this project's development will be its integration to the TERA framework, following the addition of models interconnecting engine performance to economic and environmental criteria. As a final step, an interface of this new TERA module with an external optimization solver would introduce the capability of partially or fully automating the process of propulsion system preliminary design by closing the loop between the initial conceptual studies and the propulsion system's operational life.

REFERENCES

[1] R. G. Grant, Flight: The complete History: Dorling Kindersley Limited, London, 2010.

[2] B. W. McCormick, Aerodynamics, Aeronautics and Flight Mechanics: John Wiley and Sons Inc., New York, 1979.

[3] C. W. Boppe, "Aircraft Drag Analysis Methods," *AGARD-R-783,* 1991.

[4] C. E. Jobe, "Prediction of Aerodynamic Drag," US Air Force Wright Aeronautical Laboratories, Wright-Patterson Air Force Base, Ohio, 1984.

[5] ESDU 97016, "Estimation of Airframe Drag by Summation of Components: Principles and Examples," ESDU International, 1997.

[6] P. Laskaridis, "Performance Investigations and Systems Architectures for the More Electric Aircraft," PhD Thesis, School of Engineering, Cranfield University, Cranfield, 2004.

[7] I. H. Abbott and A. E. Von Doenhoff, Theory of Wing Sections: Dover Publications, Mineola, 1959.

[8] M. Ghoreyshi, D. Vallespin, A. Ronch, K. J. Badcock, J. Vos and S. Hitzel, "Simulation of Aircraft Maneuvres based on Computaional Fluid Dynamics," in *AIAA Atmospheric Flight Mechanics Conference,* Toronto, Canada, 2-5 August 2010.

[9] AFFDL-TR-79-3032, "The USAF Stabiltiy and Control Digital Datcom," McDonnel Douglas Astronautics Company, St Louis, Missouri, 1979.

[10] A. K. Cooke, "A Simulation Model of the NFLC Jetstream 31," School of Engineering, Cranfield University, Cranfield, 2006.

[11] M. Tsentseris, "Development of ARES: Method for Military Aircraft/Engine Integration," MSc Thesis, School of Engineering, Cranfield University, Cranfield, 2009.

[12] ETPS, "The Drag Index Concept of Performance: Training Notes," DERA, Boscombe Down, UK, 2000.

[13] R. V. J. Harris, "An Analysis and Correlation of Aircraft Wave Drag," NASA TM X-947, Langley Research Center Langley Station, 1964.

[14] T. M. Berens, "Aerodynamic Propulsion Integration for Supersonic Business Jets," in *46th AIAA/ASME/SAE/ASEE Joint Propulsion Conference & Exhibit*, Nashville, 25-28 July 2010.

[15] R. T. Whitcomb, "A Study of the Zero-Lift Drag-Rise Characteristics of Wing-Body Combinations Near the Speed of Sound," NACA, Langley Field, 1956.

[16] R. T. Jones, "Theory of Wing-Body Drag at Supersonic Speeds," NACA, Moffett Field, 1959.

[17] S. K. Rallabhandi and D. N. Mavris, "An Unstructured Wave Drag Code for Preliminary Design of Future Supersonic Aircraft," in *33rd AIAA Fluid*

Dynamics Conference and Exhibit, Orlando, Florida, 23-26 June 2003.

[18] E. Glasgow, D. Santman and L. Miller, "Experimental and Analytical Determination of Integrated Aiframe Nozzle Performance," AFFDL-TR-72-101, Air Force Flight Dynamics Laboratory, Wright-Patterson Air Force Base, Ohio,1972.

[19] R. Heffley and F. Wayne, "Aircraft Handling Qualities Data," NASA CR-2144, NASA, Washington DC, 1972.

[20] G. Teper, "Aircraft Stability and Control Data," NASA CR-96008, NASA Ames Research Center, Mountain View, California, 1969.

[21] E. Haering and F. J. Burcham, "Minimum Time and Fuel Flight Profiles for an F-15 Airplane with a Highly Integrated Digital Electronic Control System," NASA-TM-88042, NASA Ames Research Center, Mountain View, California, 1984.

[22] L. Nguyen, M. Ogburn, W. Gilbert, K. Kibler, P. Brown and P. Deal, "Simulator Study of Stall/Post-Stall Characteristics of a Fighter Airplane with Relaxed Longitudinal Static Stability," NASA-TP-1538, NASA Langley Research Center, Hampton, Virginia, 1979.

[23] T. Webb, D. Kent and J. Webb, "Correlation of F-16 Aerodynamics and Performance Predictions with Early Flight Test Results," AGARD-CP-242, 1977.

[24] D. L. Bowers, "Throttle Dependent Forces - A Primer," US Air Force Wright Aeronautical Laboratories, Wright-Patterson Air Force Base, Ohio, 1985.

[25] T. Triantafyllou, "Effect of Airflow Distortion on Installed Gas Turbine Performance", PhD thesis, Cranfield University, Cranfield, UK, 2017.

[26] AGARD-AG-237, "Guide to In-Flight Thrust Measurement of Turbojets and Fan Engines," AGARD, Neully-sur-Seine, France, 1979.

[27] H. Oertel, Prandtl's Essentials of Fluid Mechanics: Springer-Verlag, New York, 2004.

[28] P. R. Payne, "Aftebody Drag Volume 2-Jet Interference Effects on Subsonic Boattal Drag," DTNSRDC, Bethesda, Maryland, 1980.

[29] ESDU 00026, "Supersonic Pressure Drag of Conical, Circular-Arc and Parabolic Boat-Tails," ESDU International, 2000.

[30] C. Swavely and J. Soileau, "Aircraft aft body/propulsion system integration for low drag," *AIAA paper No 72-1101* in *AIAA/SAE 8th Joint Propulsion Specialist Conference,* New Orleans, Louisiana, 29 November-1 December 1972*.*

[31] M. Brazier and W. Ball, "Accounting of Aerodynamic Forces on Airframe/Propulsion System," *AGARD CP 150, paper 7,* 1974.

[32] W. B. Compton, "Effects of Jet Exhaust Gas Properties on Exhaust Simulation and Afterbody Drag," NASA TR R-444, NASA Langley

Research Center, Hampton, Virginia., 1975.

[33] L. L. Steers, "Flight-Measured Afterbody Pressure Coefficients from an Airplane having Twin Side-by-Side Jet Engines for Mach Numbers from 0.6 to 1.6," NASA TP 1549, NASA Dryden Flight Research Center, Edwards, California, 1979.

[34] D. E. Reubush and L. E. Putnam, "An Experimental and Analytical Investigation of the Effect on Isolated Boattail Drag of Varying Reynolds Number up to $130 \cdot 10^6$," NASA TN D-8210, NASA Langley Research Center, Hampton, Virginia., 1976.

[35] D. E. Reubush, "Effect of Reynolds Number on the Subsonic Boattail Drag of several Wing-Body Configurations," NASA TN D-8238, NASA Langley Research Center, Hampton, Virginia., 1976.

[36] W. B. Compton and J. F. Runckel, "Jet Effects on the Boattail Axial Force of Conical Afterbodies at Subsonic and Transonic Speeds," NASA TM X-1960, NASA Langley Research Center, Hampton, Virginia, 1970.

[37] AGARD-AR-226, "Aerodynamics of Aircraft Afterbody," AGARD, Neully-sur-Seine, France, 1986.

[38] Royal Air Force Historical Society, The birth of the Tornado, Royal Air Force Historical Society, 2002.

[39] R. Whitford, Design for Air Combat: Jane's Publishing Company Limited, London, 1987.

[40] FLIGHT International, "FIAT G.91Y," pp. 931-932, 20 June 1968.

[41] J. Cluts, C.-W. Kuo and M. Samimy, "Exploring Physics and Control of Twin Supersonic Circular Jets," in *53rd AIAA Aerospace Sciences Meeting*, Kissimmee, Florida, 5-9 January 2015.

[42] AGARD-AR-318, "Aerodynamics of 3-D Aircraft Afterbodies," AGARD, Neully-sur-Seine, France, 1995.

[43] N. J. Georgiadis and J. R. DeBonis, "Navier-Stokes analysis methods for turbulent jet flows with application to aircraft exhaust nozzles," *Progress in Aerospace Sciences,* no. 42, pp. 377-418, 2006.

[44] P. Wang and J. McGuirk, "Large Eddy Simulation of Supersonic Jet Plumes from Rectangular Con-Di Nozzles," *International Journal of Heat and Fluid Flow,* no. 43, pp. 62-73, 2013.

[45] D. Allison and E. Alyanak, "Development of Installed Propulsion Performance Model for Efficient Supersonic Air Vehicle Design," SAE Technical Paper 2014-01-2133, 2014.

[46] R. Leinburger, Fighter: Parragon Books Ltd, Bath, UK, 2011.

[47] MIL-C-005011B, "Standard Aircraft Characteristics and Performance, Piloted Aircraft (Fixed Wing)," US Department of Defence, Washington DC, 1951.

[48] MIL-STD-3013, "Glossary of Definitions, Ground Rules and Mission

Profiles to Define Air Vehicle Performance Capability," US Department of Defence, Washington DC, 2003.

[49] J. R. Boyd, T. P. Christie and J. E. Gibson, "Energy-Manoeuvrability," AD372287, Air Proving Ground Center Eglin AFB, 1966.

[50] E. Rutowski, "Energy Approach to the General Aircraft Performance Problem," *Journal of the Aeronautical Sciences,* vol. 21, no. 3, pp. 187-195, March 1954.

[51] J. Neufeld, "The F-15 Eagle: Origins and Development 1964-1972," Office of Air Force History, USAF, 1974.

[52] T. Takahashi, "Aircraft Concept Design Performance Visualization Using an Energy-Manoeuvrability Presentation," in *12th AIAA Aviation Technology, Integration and Operations (ATIO) Conference and 14th AIAA/ISSM Multidisciplinary Analysis and Optimization Conference*, Indianapolis, Indiana, 17-19 September 2012.

[53] G. Wunderlich and H. Fehrenz, "Air Combat Simulation: Methods, Models, Trends," *AGARD-AG-262,* 1984.

[54] D. Cenciotti, "“Here’s What I’ve Learned so Far Dogfighting in the F-35”: a JSF Pilot’s first-hand Account," The Aviationist, [Online]. Available: https://theaviationist.com/2016/03/01/heres-what-ive-learned-so-far-dogfighting-in-the-f-35-a-jsf-pilot-first-hand-account/. [Accessed 1st November 2016].

[55] J. Stillion, "Trends in Air-to-Air Combat: Implications for Future Air Superiority," Center for Strategic and Budgetary Assessment, 2015.

[56] M. Arena, O. Younossi, K. Brancato, I. Blickstein and C. Grammich, "Why Has the Cost of Fixed-Wing Aircraft Risen?," RAND Corporation, Santa Monica, CA, 2008.

[57] J. W. McManus and K. H. Goodrich, "Application of Artificial Intelligence (AI) Programming Techniques to Tactical Guidance for Fighter Aircraft," AIAA Paper 89-3525, in *Proceedings AIAA Guidance, Navigation and Control Conference*, Boston, Massachusetts, 14-16 August 1989.

[58] G. H. Burgin and A. Owens, "An Adaptive Manoeuvring Logic Program for the Simulation of One-on-One Air-to-Air Combat," NASA CR-2582, CR-2583, Decision Science, San Diego, California, 1975.

[59] R. D. Kosciusko, "Correlation of Fighter Aircraft Performance with Combat Effectiveness in a Tactically Significant Environment," Msc Thesis, Massachusetts Intitute of Technology, 1991.

[60] M. Nichols, "Bibliography in Aerodynamics of Airframe/Engine Integration of High-Speed Turbine-Powered Aircraft, Vol I," NASA TM-81814, NASA Langley Research Center, Hampton, Virginia, 1980.

[61] AGARD, "Aerodynamic Engine/Airframe Integration for High Performance Aircraft and Missiles," AGARD-CP-498, 1992.

[62] E. Zitzler, D. Brockhoff and L. Thiele, "The Hypervolume Indicatot

Revisited: On the Design of Pareto-compliant Indicators via Weighted Integration," in *Proceedings of the Evolutionary Multi-Criterion Optimization (EMO 2007)*, Matsushima, Japan, 5-8 March 2007.

[63] US Department of Defence, "MIL-E-5007: Engines, Aircraft, Turbojet and Turbofan, General Specification for," US Department of Defence, Washington DC, 1973.

[64] J. Mace and G. Nyberg, "Fighter Airframe/Propulsion Integration - A McDonnel Aircraft Perspective," in *28th Joint Propulsion Conference and Exhibit*, Nashville, Tenessee, 6-8 July 1992.

[65] L. McCullers, "Aircraft Configuration Optimization Including Optimized Flight Profiles," *Proceedings of Symposium on Recent Experiences in Multidiciplinary Analysis and Optimization, NASA CP-2327,* pp. 395-412, 1984.

[66] R. Plenener and C. Snyder, "The Navy/NASA Engine Program (NEPP) - A User's Manual," NASA TM-105186, NASA Lewis Research Center, Cleveland, Ohio, 1991.

[67] T. Lavelle, R. Plenener and J. Seidel, "Concurrent Optimization of Airframe and Engine Design Parameters," in *4th Symposium on Multidiciplinary Analysis and Optimization*, Cleveland, Ohio, 21-23 September 1992.

[68] J. Lytle, "The Numerical Propulsion System Simulation: An Overview," NASA TM-2000-209915, NASA Glenn Research Center, Cleveland, Ohio, 2000.

[69] R. Mishler and T. Wilkinson, "Emerging Airframe/Propulsion Integration Technologies at General Electric," in *28th Joint Propulsion Conference and Exhibit*, Nashville, Tenessee, 6-8 July 1992.

[70] A. Seitz, "Advanced Methods for Propulsion System Integration in Aircraft Conceptual Design," PhD thesis, Techische Universitat Munchen, Munchen, 2011.

[71] W. Lammen, P. Kupijai, D. Kickenweitz and T. Laudan, "Integrate Engine Manufacturer's Knowledge into the Preliminary Aircraft Sizing Process," NLR-TP-2014-428, NLR, Amsterdam, The Netherlands, 2014.

[72] S. Ogaji, P. Pilidis and R. Hales, "TERA - A Tool for Aero-engine Modelling and Management," in *2nd World Congress on Engineering Asset Management and the 4th International Conference on Condition Monitoring*, Harrogate, UK, 11-14 June 2007.

[73] T. Nikolaidis, "The TURBOMATCH 2.0 Scheme for Gas Turbine Performance Calculations," unpublished software manual, Cranfield University, Cranfield, UK, 2015.

[74] D. Johnson, "Evaluation of Energy Manoeuvrability Procedures in Aircraft Flight Path Optimization and Performance Estimation," AD754909, Wright Patterson Air Force Base, Dayton, Ohio, USA, 1972.

[75] T. Takahashi, "Optimal Climb Trajectories through Explicit Simulation," in *Proceedings of the 15th AIAA Aviation Technology, Integration and Operations Conference*, Dallas, TX, USA, 22-26 June 2015.

[76] J. Betts, "A Survey of Numerical Methods for Trajectory Optimization," *Journal of Guidance, Control and Dynamics,* no. 21, pp. 193-207, 1998.

[77] S. Ong, "Sequential Quadratic Programming Solutions to Related Aircraft Trajectory Optimization Problems", PhD thesis, Iowa State University, Ames, Indiana, 1992.

[78] K. Chircop, D. Zammit-Mangion and R. Sabatini, "Bi-Objective Pseudospectral Optimal Control Techniques for Aircraft Trajectory Optimization," in *In Proceedings of the 28th International Congress of the Aeronautical Sciences*, Brisbane, Australia, 23-28 September 2012.

[79] D. Bertsekas, Dynamic Programming and Optimal Control, Volume 1: Athena Scientific, Belmont, Massachusetts, 1995.

[80] O. Von Stryk and R. Bulirsch, "Direct and Indirect Mehods for Trajectory Optimization," *Annals of Operations Research,* vol. 37, no. 1, pp. 357-373, 1992.

[81] J. Holub, J. Foo, V. Kilivarapu and E. Winer, "Three Dimensional Multi-Objective UAV Path Planning using Digital Pheromone Particle Swarm Optimization," in *53rd AIAA/ASME/ASCE/AHS/ASC Structures, Structural Dynamics and Materials Conference*, Honolulu, Hawaii, 23-26 April 2012.

[82] G. Bower and I. Kroo, "Multi-Objective Aircraft Optimization for Minimum Cost and Emissions over Specific Route Networks," in *Proceedings of the 26th International COngress of the Aeronautical Sciences*, Anchorage, Alaska, 14-19 September 2008.

[83] N. Yokoyama and S. Suzuki, "Modified Genetic Algorithm for Constrained Trajectory Optimization," *Journal of Guidance, Control and Dynamics,* no. 28, pp. 139-144, 2005.

[84] M. Pontani and B. Conway, "Particle Swarm Optimization Applied to Space Trajectories," *Journal of Guidance, Control and Dynamics,* no. 33, pp. 1429-1441, 2010.

[85] A. Rahimi, K. Kumar and H. Alighanbari, "Particle Swarm Optimization Applied to Spacecraft Reeentry Trajectory," *Journal of Guidance, Control and Dynamics,* no. 36, pp. 307-310, 2013.

[86] M. Pontani, P. Ghosh and B. Conway, "Particle Swarm Optimization of Multiple-Burn Rendezvous Trajectories," *Journal of Guidance, Control and Dynamics,* no. 35, pp. 1192-1207, 2012.

[87] N. Othman and M. Kanazaki, "Development of Multiobjective Trajectory-Optimization Method and its Application to Improve Aircraft Landing," *Aerospace Science and Technology,* no. 28, pp. 166-177, 2016.

[88] M. Vavrina and K. Howell, "Multiobjective Optimization of Low-Thrust Trajectories Using a Genetic Algorithm Hybrid," in *In Proceedings of the*

AAS/AIAA Space Flight Mechanics Meeting, Pittsburgh, Pennsylvania, 9-13 August 2009.

[89] J. White, "Aircraft Infrared Principles, Signatures, Threats and Countermeasures," NAWCWD TP 8773, Point Mugu, California, 2012.

[90] F. Neri, Introduction to Electronic Defence Systems, 2nd ed, SciTech Publishing Inc, Raleigh, North Carolina, 2001.

[91] S. Mahulikar, S. Sane and A. Marathe, "Numerical Studies of Infrared Signature Levels of Complete Aircraft," *The Aeronautical Journal,* no 105., pp. 185-192, 2001.

[92] L. Jianwei and W. Qiang, "Aircraft-skin Infrared Radiation Characteristics Modeling and Analysis," *Chinese Journal of Aeronautics,* vol. 22, pp. 493-497, 2009.

[93] T. Kim, H. Lee, J. Bae, T. Kim, J. Cha, D. Jung and H. Cho, "Susceptibility of Combat Aircraft Modeled as an Anisotropic Source of Infrared Radiation," *IEEE Transactions on Aerospace and Electronic Systems,* vol. 52, no. 5, pp. 2467-2476, 2015.

[94] G. Rao and S. Mahulikar, "New Criterion for Aircraft Susceptibility to Infrared Guided Missiles," *Aerospace Science and Technology,* vol. 9, no. 8, pp. 701-712, 2005.

[95] H. Sonawane and S. Mahulikar, "Tactical Air Warfare: Generic Model for Aircraft Susceptibility to Infrared Guided Missiles," *Aerospace Science and Technology,* vol. 15, pp. 249-260, 2011.

[96] H. Sonawane and S. Mahulikar, "Effect of Missile Turn Rate on Aircraft Susceptibility to Infrared-Guided Missile," *Journal of Aircraft,* vol. 50, no. 2, pp. 663-666, 2013.

[97] K. Andersson, "Modeling the Impact of Surface Emissivity on the Military Utility of Attack Aircraft," *Aerospace Science and Technology,* vol. 65, pp. 133-140, 2017.

[98] J. Boyd, "Aerial Attack Study," USAF Fighter Weapons School, Nellis Air Force Base, Nevada, 1960.

[99] R. L. Shaw, Fighter Combat: Tactics and Manoeuvring: United States Naval Institute, Annapolis, Maryland, 1985.

[100] D. Alkaher and A. Moshaiov, "Dynamic-Escape-Zone to Avoid Energy-Bleeding Coasting Missile," *Journal of Guidance, Control and Dynamics,* vol. 38, no. 10, pp. 1908-1921, 2015.

[101] S. Ong and B. Pierson, "Optimal Planar Evasive Aircraft Manoeuvres against Proportional Navigation Missiles," *Journal of Guidance, Control and Dynamics,* vol. 19, no. 6, pp. 1210-1215, 1996.

[102] K. Virtanen, T. Raivio and P. Hamalainen, "An Influence Diagram Approach to One-on-One Air Combat," in *10th International Symposium on Dynamic Games and Applications*, St Petersburg, Russia, 8-11 July 2002.

[103] K. Horie and B. Conway, "Optimal Fighter Pursuit-Evasion Manoeuvres Found via Two-Sided Optimization," *Journal of Guidance, Control and Dynamics,* vol. 29, no. 1, pp. 105-112, 2006.

[104] J. Eklund, J. Sprinkle and S. Sastry, "Implementing and Testing a Nonlinear Model Predictive Tracking Controller for Aerial Pursuit/Evasion Games on aa Fixed Wing Aircraft," in *2005 American Control Conference*, Portland, Oregon, 8-10 June 2005.

[105] J. Sprinkle, J. Eklund, H. Kim and S. Sastry, "Encoding Aerial Pursuit/Evasion Games with Fixed Wing Aircraft into a Nonlinear Model Predictive Tracking Controller," in *43rd IEEE Conference on Decision and Control*, Paradise Island, Bahamas, 14-17 December 2004.

[106] D. You and D. Shim, "Design of an Aerial Combat Guidance Law Using Virtual Pursuit Point Concept," *Proceeding of the Institution of Mechanical Engineers, Part G: Journal of Aerospace Engineering,* vol. 229, no. 5, pp. 792-813, 2015.

[107] Y. Baba and H. Takano, "Air Combat Guidance Law for UCAV," in *AIAA 1st Technical Conference and Workshop on Unmanned Aerospace Vehicles*, Portsmouth, Vinrginia, 20-22 May 2002.

[108] F. Imado, "Some Aspects of a Realistic Three-Dimensional Pursuit-Evasion Game," *Journal of Guidance, Control and Dynamics,* vol. 16, no. 2, pp. 289-293, 1993.

[109] G. Burgin and L. Sidor, "Rule-Based Air Combat Simulation," NASA CR-4160, Ames Research Center, Mountain View, California, 1986.

[110] G. Carpenter and et al, "Analysis of Aircraft Evasion Strategies in Air-to-Air Missile Effectiveness Models," Grumman Aerospace Corporation, Bethpage, NY, 1974.

[111] M. Khan, "Game Theory Models for Pursuit Evasion Games," Technical Report, University of British Columbia, Vancouver, 2007.

[112] K. Virtanen, J. Karelahti and T. Raivio, "Modeling Air Combat by a Moving Horizon Influnce Diagram Game," *Journal of Guidance, Control and Dynamics,* vol. 29, no. 5, pp. 1080-1091, 2006.

[113] I. Nusyirwan and B. Cees, "Factorial Analysis of a Real Time Optimizaiton for Pursuit-Evasion Problem," in *46th AIAA Aerospace Sciences Meeting and Exhibit*, Reno, Nevada, 7-10 January 2008.

[114] J. McGrew, J. How, L. Bush, B. Williams and N. Roy, "Air Combat Strategu using Approximate Dynamic Programming," in *AIAA Guidance, Navigation and Control Conference and Exhibit*, Honolulu, Hawai, 18-21 August 2008.

[115] W. Macmillan, "Development of a Modular Type Computer Program for the Calculation of Gas Turbine Off-Design Performance, Phd Thesis," Cranfield Institute of Technology, Cranfield, UK, 1974.

[116] C. Coello and M. Lechunga, "MOPSO: A Proposal for Multiple Objective

Particle Swarm Optimization," in *Proceedings of the 2002 Congress on Evolutionary Computation, part of the 2002 IEEE World Congress on Computational Intelligence*, Honolulu, HI, USA, 12-17 May 2002.

[117] USAF, "T.O. 1F-4E-1: USAF Series F-4E Aircraft Flight Manual," USAF, 1979.

[118] D. Williams, "Propulsion System Performance Integration: Lecture Notes," Cranfield University, Cranfield, UK, 2013.

[119] US Department of Defence, "MIL-E-5007: Engines, Aircraft, Turbojet and Turbofan, General Specification for," US Department of Defence, Washington DC, USA, 1973.

[120] ESDU 01012, "Subsonic Pressure Drag of Boat-Tails with Negligible Annular Base Area in the Presence of a Central Propulsive Jet," ESDU International, 2001.

[121] ESDU 00017, "Supersonic Base and Boat-Tail Pressure Drag of Cylindrical Bodies with a Conical Boat-Tail and a Central Propulsive Jet," ESDU International, 2000.

[122] ESDU 99010, "Supersonic Base Drag of Cylindrical Bodies with a Central Propulsive Jet," ESDU International, 2005.

[123] S. Mahulikar, P. Kolhe and G. Rao, "Skin-Temperature Prediction of Aircraft Rear Fuselage with Multimode Thermal Model," *Journal of Thermophysics and Heat Transfer,* vol. 19, no. 1, pp. 114-124, 2005.

[124] K. Yi, S. Baek, M. Kim, S. Lee and W. Kim, "The Effects of Heat Shielding in Jet Engine Exhaust Systems on Aircraft Survivability," *Numerical Heat Transfer, Part A,* vol. 66, pp. 89-106, 2014.

[125] ESDU 69011, "Heat Transfer by Forced Convection between a Two-Dimensional Turbulent Boundary Layer and a Smooth Flat Plate, with Application to Wedges, Cyliders and Cones," ESDU International, 2000

[126] S. Mahulikar, H. Sonawane and G. Rao, "Infrared Signature Studies of Aerospace Vehicless," *Progress in Aerospace Sciences,* vol. 43, pp. 218-245, 2007.

[127] C. Bauer, A. Koch, F. Minutolo and P. Grenard, "Engineering Model for Rocket Exhaust Plumes Verified by CFD Results," in *29th ISTS*, Nagoya, Japan, 2-9 June 2013.

[128] U. von Glahn, D. Groesbeck and J. Goodykoontz, "Velocity Decay and Acoustic Characteristics of Various Nozzle Geometries with Forward Velocity," NASA TM X-68259, Lewis Research Center, Cleveland, Ohio, 1973.

[129] G. Abramovich, The Theory of Turbulent Jets: The M.I.T. Press, Cambridge, Massachusetts, 1963.

[130] T. Triantafyllou, T. Nikolaidis, M. Diakostefanis and P. Pilidis, “Numerical Simulation of the Airflow over a Military Aicraft with Active Intake,” *Proceedings of the Institution of Mechanical Engineers, Part G: Journal of*

Aerospace Engineering, vol. 8, no. 231, pp. 1369-1390, 2017.

[131] S. Baqar, "Low-Cost PC-based High-Fidelity Infrared Signature Modelling and Simulation," PhD thesis, Defence College of Management and Technology, Cranfield University, 2007.

[132] D. Aronstein, Advanced Tactical Fighter to F-22 Raptor: Origins of the 21st Century Air Dominance Fighter, AIAA, 1998.

[133] AGARD-CP-512, "Combat Aircraft Noise," AGARD, Neuilly sur Seine, France, 1992.

[134] M. Lighthill, "On Sound Generated Aerodynamically I. General Theory," *Proceedings of the Royal Society (London), series A,* vol. 211, no. 1107, pp. 564-587, 1952.

[135] M. Lighthill, "On Sound Generated Aerodynamically II. Turbulence as a Source of Sound," *Proceedings of the Royal Society (London), series A,* vol. 222, no. 1148, pp. 1-32, 1954.

[136] W. Zorumski, "Aircraft Noise Prediction Program Theoretical Manual," NASA TM-83199 Part 2, NASA Langley Research Center, Hampton, Virginia, 1982.

[137] S. Pietrzko, "FLULA-Swiss Aircraft Noise Prediction Program," in *Acoustics 2002 - Innovation in Acoustics and Vibration Annual Conference of the Australian Acoustical Society*, Adelaide, Australia, 13-15 November 2002.

[138] SAE ARP 876F, "Gas Turbine Jet Exhaust Noise Prediction," SAE International, 2013.

[139] ESDU 90023, "Airframe Noise Prediction," ESDU International, 2017.

[140] ESDU 98019, "Computer-Based Estimation Procedure for Single-Stram Jet Noise Including Far-Field, Static Jet Mixing Noise Database for Circular Nozzles," ESDU International, 2016.

[141] ESDU 14014, "A Theoretically-Based Method for Predicting Static-to-Flight Effects on Coaxial Jet Noise," ESDU International, 2016.

[142] R. Stone, "Interim Prediction Method for Jet Noise," NASA TM X-71618, NASA Lewis Research Center, Cleveland, Ohio, 1974

[143] J. Stone, "An Improved Method for Predicting the Effects of Flight on Jet Mixing Noise," NASA TM-79155, NASA Lewis Research Center, Cleveland, Ohio, 1979.

[144] J. Stone, "An Improved Prediction Method for the Noise Generated in Flight by Circular Jets," NASA TM-81470, NASA Lewis Research Center , Cleveland, Ohio, 1980.

[145] H. Carlson, "Simplified Sonic-Boom Prediction," NASA TP-1122, NASA Langley Research Center, Hampton, Virginia, 1978.

[146] G. Farin, Curves and Surfaces for CAGD: A Practical Guide, 5th ed., Morgan-Kaufmann, San Francisco, California, 2002.

[147] M. Reyes-Sierra and C. Coello, "Multi-Objective Particle Swarm Optimizers: A Study of the State-of-the-Art," Journal of Computational Intelligence Research, Florida, 2006, vol: 2, pp. 287-308.

[148] P. Sujit, S. Saripalli and J. Sousa, "An Evaluation of UAV Path Following Algorithms," in *2013 European Control Conference*, Zurich, Switzerland, 17-19 July 2013.

[149] E. Kontoleontos, V. Asouti and K. Giannakoglou, "An Asynchronous Metamodel-Assisted Memetic Algorithm for CFD-based Shape Optimization," *Engineering Optimization,* vol. 44, pp. 157-173, 2012.

[150] A. Antonakis and K. Giannakoglou, "Optimization of Military Aircraft Engine Maintenance subject to Engine Part Shortages using Asynchronous Metamodel-Assisted Particle Swarm Optimization and Monte-Carlo Simulations," *International Journal of Systems Science: Operations and Logistics,* vol. 5, no. 3, pp. 239-252, 2018.

[151] R. Ball, The Fundamentals of Aircraft Combat Survivability Analysis and Design, 2nd Edition: AIAA Education Series, Blacksburg, Virginia, 2003.

[152] J. Kennedy and R. Eberhart, "Particle swarm optimization," in *Proceedings of IEEE International Conference on Neural Networks 4*, Piscataway, New Jersey, 1995.